Bitlis Eren University Journal of Science and Technology

Year: 2025 • Volume: 15 • Issue: 1

ISSN: 2146-7706

Contact:

BEU Journal of Science and Technology, Bitlis Eren Üniversitesi 13000, Merkez, Bitlis/ TÜRKİYE
Tel: 0 (434) 222 0000

beujstd@beu.edu.tr https://dergipark.org.tr/tr/pub/beuscitech

Bitlis Eren University Journal of Science and Technology

e-ISSN	:	2146-7706
Date of Issue	:	June 30, 2025
Issue Period	:	June 2025
Volume	:	15
Issue	:	1
Founded	:	2011
Location	:	Bitlis
Language	:	English
Address	:	Bitlis Eren University Journal of Science and Technology Bitlis Eren Üniversitesi 13000, Merkez, Bitlis/ TÜRKİYE
e-mail	:	beujstd@beu.edu.tr
URL	:	https://dergipark.org.tr/tr/pub/beuscitech

Bitlis Eren University Journal of Science and Technology

Year: 2025 • Volume: 15 • Issue: 1

Editorial Board

Bitlis Eren University Journal of Science and Technology

Year: 2025 • Volume: 15 • Issue: 1

Bitlis Eren University Journal of Science and Technology (Bitlis Eren Univ J Sci & Technol) is an international, refereed open access electronic journal. Research results, reviews and short communications in the fields of Agriculture, Biology, Chemistry, Engineering Sciences, Mathematics, Medicinal, Molecular and Genetics, Physics, Statistics, and also Engineering Sciences are accepted for review and research article publications. Papers will be published in English. Scientific quality and scientific significance are the primary criteria for publication. Articles with a suitable balance of practice and theory are preferred. Manuscripts previously published in other journals and as book sections will not be accepted.

Bitlis Eren University Journal of Science and Technology indexed in:

- EBSCO
- SCILIT
- ACARINDEX
- SOBIAD
- ACADEMINDEX

Bitlis Eren University Journal of Science and Technology

Year: 2025 • Volume: 15 • Issue: 1

Articles

BİTLİS EREN UNIVERSITY

JOURNAL OF SCIENCE AND TECHNOLOGY

E-ISSN: 2146-7706

MODELING AND COMPREHENSIVE STRATEGIC INTERVENTION ANALYSIS FOR HEPATITIS A AND E INFECTIONS: A PARADIGM SHIFT IN PUBLIC HEALTH DYNAMICS

Adedapo Chris Loyinmi

Tai Solarin University of Education, Department of Mathematics, Ogun State, Nigeria
loyinmiac@tasued.edu.ng

KEYWORDS

Hepatitis A & E
Optimal control Strategies
Public health interventions
Sensitivity analysis
Mathematical modelling

ARTICLE INFO

Research Article
Doi
10.17678/beuscitech.1573256

Received	October 24, 2024
Revised	January 19, 2025
Accepted	February 21, 2025
Year	2025
Volume	15
Issue	1
Pages	1-36

ABSTRACT

Infectious diseases like Hepatitis A and E pose substantial challenges to public health globally, necessitating innovative strategies that combine mathematical modelling with strategic intervention analysis. This study introduces a comprehensive mathematical model designed to encapsulate the complex dynamics of Hepatitis A and E infections, including susceptibility, vaccination, latent and acute phases, treatment, and recovery.

A thorough quantitative analysis was performed, encompassing the non-negativity and boundedness of solutions, the disease-free equilibrium, and the basic reproductive ratio. Stability analyses provided critical insights into the local and global dynamics of the model, essential for understanding the conditions under which the diseases persist or are controlled.

Sensitivity analysis highlighted key parameters driving disease transmission, aiding in the development of targeted intervention strategies. Utilizing optimal control theory, innovative intervention frameworks were formulated to optimize vaccination campaigns, allocate treatment resources efficiently, implement health education programs, and enhance sanitation measures. Numerical simulations further demonstrated the effectiveness of these interventions, showcasing their influence on population dynamics, disease prevalence, and environmental contamination.

1 INTRODUCTION

The historical trajectory of hepatitis, spanning from ancient civilizations to modern scientific discoveries, reflects a complex interplay between human behavior, societal conditions, and viral pathogens. Millennia ago, descriptions of clinical syndromes resembling hepatitis can be traced back to Sumerian medical texts, highlighting the enduring presence of this disease throughout human history. Hippocrates' observations of "epidemic jaundice" further underscored the recognition of hepatitis-like illnesses in antiquity. During subsequent centuries, particularly in the Middle Ages, rudimentary understanding of jaundice transmission emerged, exemplified by Pope Zacharias' quarantine measures [1-4]. However, it wasn't until the 20th century, amid the upheavals of global conflicts, that significant strides were made in elucidating the viral etiology of hepatitis. Pioneering experiments during World War II revealed distinct subtypes of viral hepatitis, paving the way for the identification of hepatitis A and hepatitis B. By the late 1970s, the emergence of hepatitis C as a distinct pathogen underscored the complexity of viral hepatitis. The discovery of hepatitis E virus (HEV) further expanded our understanding, particularly in regions where hepatitis A was traditionally assumed to be the primary cause of waterborne outbreaks [5-8]. The pivotal moment came when Russian virologist Mikhail Balayan's self-experimentation led to the identification of HEV, shedding light on a previously unrecognized form of viral hepatitis. From a virological perspective, hepatitis A virus (HAV) and HEV belong to different families and exhibit distinct genetic characteristics [9-18]. Despite their differences, both viruses share a remarkable ability to survive in the environment due to their non-enveloped structure, facilitating transmission through contaminated food and water sources. This underscores the importance of sanitation measures in preventing hepatitis outbreaks. Epidemiologically, HAV and HEV display contrasting patterns of transmission and geographic distribution. While HAV primarily spreads through fecal-oral routes, HEV transmission encompasses zoonotic and waterborne routes, with variations in prevalence across different regions. Understanding these transmission dynamics is crucial for implementing targeted prevention strategies. Clinically, both HAV and HEV can cause acute hepatitis with varying degrees of severity, although chronic infection is rare with HAV. The clinical presentation of hepatitis A and E can overlap, but distinct features may aid in differential diagnosis [17-21]. Moreover, the emergence of extra hepatic manifestations further complicates the clinical picture, highlighting the multisystem nature of these infections. Diagnosing hepatitis, particularly HEV infection, presents challenges due to limited awareness among clinicians and variability in testing availability and accuracy. Treatment options for acute hepatitis A and E are primarily supportive, with ribavirin showing efficacy in selected cases of severe acute hepatitis E. In chronic HEV infection, reduction of immunosuppression and antiviral therapy with ribavirin are considered, emphasizing the importance of tailored management approaches. Prevention remains the cornerstone of hepatitis control efforts, encompassing measures such as vaccination, sanitation improvements, and public health interventions. Vaccination against HAV and the availability of an HEV vaccine in certain regions offer promising avenues for disease prevention [22-32].

The seminal mathematical framework for analyzing the propagation of infectious diseases was spearheaded by Bernoulli in 1760. Its primary objective was to evaluate the impact of variolation, an early technique akin to smallpox vaccination, on life-tables utilized in actuarial calculations. Mathematical models play an indispensable role in scientific and medical spheres, enabling the interpretation of outcomes, formulation of hypotheses, design of experiments, derivation of diagnoses from clinical presentations and test results, and provision of guidance for decision-making processes [1], [16], [33-40]. Mathematical representation of models allows for meticulous analysis, enabling quantitative forecasts regarding disease trends and intervention impacts. Increasingly, the utilization of mathematical frameworks in elucidating the dynamics of infectious disease propagation holds significant prominence in the formulation of public health protocols. Notable applications encompass the management of the foot-and-mouth disease outbreak in the UK during 2001, addressing episodes of severe acute respiratory syndrome (SARS) and Middle East respiratory syndrome coronavirus (MERS-CoV), devising strategic approaches for controlling tuberculosis (TB), human immunodeficiency virus (HIV), and sexually transmitted infections (STIs), as well as crafting vaccination policies, enhancing preparedness for pandemic influenza, planning responses to bioterrorism threats, strategizing intervention trials, assessing the efficacy of interventions, enriching comprehension of disease progression, and investigating fundamental principles governing disease control [31-34], [39-42]. Infectious disease epidemiology is inherently interdisciplinary as infection transmission within a populace is influenced not only by the biological attributes of the infectious agent and its host, but also by host (and vector, where applicable) contact patterns, environmental factors, and human utilization of healthcare services and response to public health measures, among other factors. Mathematical modeling serves to delineate the intricate interplay among these factors and enables integration of data from diverse disciplines, including social sciences. Crucially, models ought not to be enigmatic constructs but should be lucidly expounded to enable assessment of model validity and data utilization by non-modelers. Modeling embodies the process of formalizing conceptualizations of a system, aimed at enhancing clarity; nevertheless, infectious disease transmission dynamics typically exhibit inherent complexity [3], [5], [7], [38-46].

To gain deeper insights into the epidemiological characteristics of Hepatitis A and E, researchers employ sophisticated mathematical modeling techniques akin to those utilized in studying diseases like diphtheria, pertussis, and influenza. This analytical approach, widely employed in infectious disease epidemiology, enables a systematic exploration of the intricate patterns of transmission within populations. Just as mathematical models have been instrumental in elucidating transmission dynamics of various infectious diseases, from COVID-19 to Lassa fever, we introduce a comprehensive model tailored specifically to understand the transmission dynamics of Hepatitis A and E viruses [2], [3], [7], [46-50].

Infectious diseases, such as Hepatitis A and E, present significant challenges to public health worldwide. Addressing these challenges requires innovative approaches integrating mathematical modeling and strategic intervention analysis, hence this research study holds significant implications for public health epidemiology by providing a comprehensive framework for understanding and controlling Hepatitis A and E infections. Through mathematical modeling and quantitative analysis, the proposed model elucidates the dynamics of transmission, the impact of interventions such as vaccination and treatment, and the effectiveness of sanitation measures. By identifying key parameters and evaluating their sensitivity, the study offers valuable insights into optimal control strategies for taming disease burden. Findings will further contribute to evidence-based decision-making in disease prevention and control, aiding policymakers and healthcare professionals in implementing targeted interventions to reduce Hepatitis A and E transmission and improve population health outcomes.

The proposed mathematical model and use of optimal control theory offer a unique and comprehensive framework for analyzing the dynamics of Hepatitis A and E infections. Unlike traditional SIRS models, this study integrates critical real-world factors such as pathogen shedding into water and food supplies, the impact of sanitation measures, and the interplay between vaccination, treatment, and environmental contamination. By leveraging Pontryagin's Maximum Principle, the research innovatively optimizes intervention strategies, providing a targeted approach to controlling disease transmission. Furthermore, this model advances existing literature by focusing specifically on the dual dynamics of Hepatitis A and E, offering insights that were previously underexplored in public health modeling. Through sensitivity analysis and numerical simulations, the study identifies and prioritizes key parameters influencing disease spread, paving the way for more effective, evidence-based intervention strategies.

2 MATERIALS AND METHOD

2.1 Model Description

We have adapted and modified a model that bears resemblance to the SIRS (Susceptible-Infectious-Recovered-Susceptible) model (Figure 1). This model comprises the following classes:

1. Susceptible (S): This class represents individuals who are susceptible to the infection and have not yet been exposed to it.

2. Vaccinated Class (V): Individuals in this class have received a vaccine before being exposed to the infection, providing them with a level of immunity.

3. Latent Individuals (L): This class includes individuals who have been exposed to the infection but have not yet developed clinical symptoms. They are asymptomatic carriers capable of transmitting the virus.

4. Acute Individuals (A): Individuals in this class have been exposed to the infection and are showing clinical symptoms. They are actively infected and capable of transmitting the virus to others.

5. Treated Acute (T): Acutely infected individuals undergoing treatment aimed at reducing their infectiousness and promoting their recovery.

6. Recovered Individuals (R): This class represents individuals who have recovered from the infection and have developed immunity against it.

This model provides a comprehensive framework for examining the dynamics of Hepatitis A and E infection, including vaccination and treatment effects across different stages of the infection cycle.

The force infection is given as

$$\omega = \rho_1 A + \rho_2 P \tag{1}$$

The model incorporates various parameters to describe the dynamics of the infection. These parameters are detailed in Table 1. Additionally, the flow map illustrating the progression of the infection is depicted in Figure 2.

***Table 1**. Explanation of the parameters utilized in the model.*

Parameters	Description
Γ	Rate of entry into the susceptible population
ϕ	Fraction of the population vaccinated
σ	Rate of vaccination among susceptible individuals
ω	Force of infection for Hepatitis A and E
a	Proportion of acute cases recovering without treatment
γ	Rate of treatment among acute cases
θ_1	Rate of recovery among treated individuals
η	Rate of pathogen mortality due to sanitation measures
δ_1	Rate of pathogen excretion into water or food supply by infectious individuals in the acute stage
δ_2	Rate of pathogen excretion into water or food supply by treated individuals
μ	Rate of natural mortality
μ_p	Rate of Hepatitis A and E disease induction
ξ	Maximum per capita growth rate of Hepatitis A and E pathogens
τ	Rate of progression from latent stage to infected stage
θ_2	Recovery rate of treated individuals

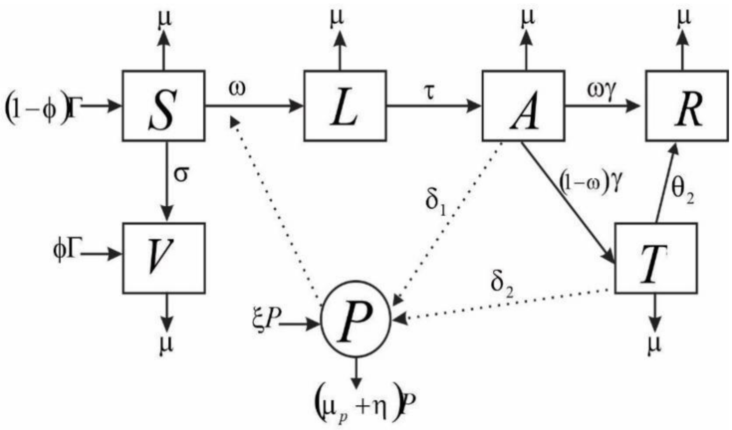

***Figure 1.** Schematic diagram interaction of each compartment.*

2.2 The Equations of the Model

From the aforementioned description, the system of equations takes the following form:

$$\left.\begin{aligned}
\frac{dS}{dt} &= (1-\phi)\Gamma - (\omega+\sigma+\mu)S \\
\frac{dV}{dt} &= \phi\Gamma + \sigma S - \mu V \\
\frac{dL}{dt} &= \omega S - (\tau+\mu)L \\
\frac{dA}{dt} &= \tau L - (a\gamma + (1-a)\gamma + \mu + \delta_1)A \\
\frac{dT}{dt} &= (1-a)\gamma A - (\theta_2+\mu+\delta_2)T \\
\frac{dR}{dt} &= a\gamma A + \theta_2 T - \mu R \\
\frac{dP}{dt} &= \delta_1 A + \delta_2 R - (\mu_p + \eta - \xi)P
\end{aligned}\right\} \qquad \textbf{(2)}$$

2.3 A Comprehensive Investigation into the Model's Quantitative Attributes

2.3.1 Non-negativity and boundedness of solution

The system (2) can be divided into two separate components: one delineating the human population N_H and the other describing the viral concentration in the surrounding environment, particularly in food and water reservoirs N_P.

The differential equation for the human population $N_H = S + V + L + A + T + R$ is as follows:

$$\frac{dN_H}{dt} = \frac{dS}{dt} + \frac{dV}{dt} + \frac{dL}{dt} + \frac{dA}{dt} + \frac{dT}{dt} + \frac{dR}{dt} \tag{3}$$

Through the substitution of the model system represented by equation (2) into equation (3) and subsequent elimination, we achieve the following result:

$$\frac{dN}{dt} = (1-\phi)\Gamma - \mu N + \delta(A+T) \tag{4}$$

Theorem 1: Let (S,V,L,A,T,R) be the solution of equation (1) with the initial conditions in a biologically feasible region Φ with: $\Phi = (S,V,L,A,T,R) \in R_+^6 : N_H \le \frac{\Gamma}{\mu}$

Then Φ is non-negative invariant.

So, Where $\delta = 0$ at DFE, equation (4) becomes

$$\frac{dN_H}{dt} = \Gamma - \mu N \tag{5}$$

By employing the integrating factor method to solve equation (5), we acquire:

$$\therefore \lim_{t\to\infty} N_H(t) \le \frac{\Gamma}{\mu} \tag{6}$$

We conducted a verification process to ensure the non-negativity and boundedness of the solution, thereby affirming the physical and epidemiological plausibility of the model's predictions. This verification safeguards against scenarios where the number of individuals within a compartment becomes negative, maintaining the integrity of the model's outcomes. Additionally, we confirmed that the Hepatitis A and E model does not exhibit unbounded growth, as its values are constrained within defined limits. This boundedness feature prevents unrealistic scenarios wherein the disease proliferates uncontrollably, ensuring that the predictions remain within attainable levels throughout the transmission process.

2.3.2 Disease- free steady-state

In this context, we examine the dynamics of the mathematical model under conditions where the disease is absent, and the population remains unaffected by new disease cases. It is important to emphasize that despite the absence of the disease, every individual within the population is considered susceptible, indicating their vulnerability to potential infections.

So, then, $S^0 \neq 0$,

For $S^0 \neq 0, V^0 = 0, L^0 = 0, A^0 = 0, T^0 = 0, R^0 = 0, P^0 = 0$,

Consequently, the set of equations delineated in the model (2) $\Gamma - \mu S^0 = 0$.

And this gives;

$$S^o = \frac{\Gamma}{\mu} \tag{7}$$

This produces the asymptotic state devoid of disease among the individuals, characterized by:

$$E^0 = \left(S^0, V^0, L^0, A^0, R^0, T^0, P^0\right) = \left(\frac{\Gamma}{\mu}, 0,0,0,0,0,0\right) \tag{8}$$

2.3.3 Basic reproductive ratio

In this analysis, we delineate the pivotal epidemiological parameter utilized for quantifying the potential dissemination of the ailment across the populace. It is imperative to acknowledge that this metric denotes the mean count of subsequent infections induced by a solitary infective entity within an entirely susceptible population. This parameter assumes critical importance in comprehending the intricacies inherent in the transmission dynamics of Hepatitis A and E, as well as in appraising the efficacy of containment methodologies.

The fundamental parameter representing the propagation potential within the model's system equation (2) is determined through the application of the next generation matrix method as elucidated by Diekmann and Heesterbeek.

Using

$$R_n = \rho(AB^{-1})$$

Consider the infected compartments in the model (2) are L, A and P.

The terminology denoting new infections and transitions in system (1) are expressed as follows;

In the model (2), the compartments representing infected individuals are denoted as L, A and P.

The terms describing new infections and transitions in system (1) are expressed as follows:

$$A = \begin{pmatrix} (\rho_1 A + \rho_2 P)S \\ 0 \\ 0 \end{pmatrix} \quad \textbf{(9)}$$

And

$$B = \begin{pmatrix} (\tau + \mu)L \\ -\tau L + (a\gamma + (1-a)\gamma + \mu + \delta_1)A \\ -\delta_1 A - \delta_2 R + (\mu_p + \eta - \xi)P \end{pmatrix} \quad \textbf{(10)}$$

Let $L = g_{1,} A = g_{2,} P = g_3$

$$F_* = \begin{bmatrix} \frac{dg_1}{dL} & \frac{dg_1}{dA} & \frac{dg_1}{dP} \\ \frac{dg_2}{dL} & \frac{dg_2}{dA} & \frac{dg_2}{dP} \\ \frac{dg_3}{dL} & \frac{dg_3}{dA} & \frac{dg_3}{dP} \end{bmatrix} \quad \textbf{(11)}$$

Upon solving equation (11), we obtain:

$$A_* = \begin{bmatrix} 0 & \rho_1 S & \rho_2 S \\ 0 & 0 & 0 \\ 0 & 0 & 0 \end{bmatrix} \quad \textbf{(12)}$$

Likewise,

$$B_* = \begin{bmatrix} (\tau+\mu) & 0 & 0 \\ -\tau & (a\gamma + (1-a)\gamma + \mu + \delta_1) & 0 \\ 0 & -\delta_1 & (\mu_p + \eta - \xi) \end{bmatrix} \quad \textbf{(13)}$$

Let $a = (\tau+\mu)$; $b = -\tau$; $c = (a\gamma + (1-a)\gamma + \mu + \delta_1)$; $d = -\delta_1$; and $e = (\mu_p + \eta - \xi)$

Now, we try to find the $B_*^{-1} = \frac{1}{|B_*|} adjB_*$

$$B_*^{-1} = \begin{bmatrix} \frac{1}{a} & 0 & 0 \\ -\frac{b}{ac} & \frac{1}{c} & 0 \\ \frac{bd}{ace} & -\frac{d}{ce} & \frac{1}{e} \end{bmatrix} \quad \textbf{(14)}$$

Therefore, substitute (17) and (12) in $R_n = \rho(AB^{-1})$, so we have

$$R_n = \begin{bmatrix} 0 & \rho_1 S & \rho_2 S \\ 0 & 0 & 0 \\ 0 & 0 & 0 \end{bmatrix} \begin{bmatrix} \frac{1}{a} & 0 & 0 \\ -\frac{b}{ac} & \frac{1}{c} & 0 \\ \frac{bd}{ace} & -\frac{d}{ce} & \frac{1}{e} \end{bmatrix} \quad \textbf{(15)}$$

$$R_n = \frac{-b\rho_1 S}{ac} + \frac{bd\rho_2 S}{ace}$$

$$R_n = R_1 + R_2$$

Where $R_1 = \frac{-b\rho_1 S}{ac}$ and $R_2 = \frac{bd\rho_2 S}{ace}$

Substituting these values into the equation above:

$a = (\tau+\mu)$; $b = -\tau$; $c = (a\gamma + (1-a)\gamma + \mu + \delta_1)$; $d = -\delta_1$; and $e = (\mu_p + \eta - \xi)$, we get

$$R_n = \frac{\tau(1-\phi)\Gamma}{\mu(\tau+\mu)(a\gamma+(1-a)\gamma+\mu+\delta_1)}\left(\rho_1 + \frac{\delta_1\rho_2}{(\mu_p+\eta-\xi)}\right) \quad \textbf{(16)}$$

Moreover, let R_1 and R_2 denote the respective contributions stemming from direct and indirect transmissions, respectively.

2.4 Stability Property

2.4.1 Local stability of the disease-free steady-state

In this examination, we investigate the regional robustness of the equilibrium devoid of disease. This characteristic delves into the temporal evolution of the model's parameters when the virus is absent, indicating the equilibrium devoid of disease. It facilitates comprehension of the model's dynamics in the absence of the virus and its sensitivity to minor alterations or disturbances.

Theorem 1:

Within the domain of model system (2), the disease-free equilibrium is regarded as locally asymptotically stable (LAS) provided that all eigenvalues of the associated Jacobian matrix exhibit negative real components.

Proof:

To clarify the aforementioned theorem, we proceed with the calculation of the Jacobian matrix concerning the dynamics of the system at the state of disease-free equilibrium (DFE). The Jacobian matrix, represented by $J(S, V, L, A, T, R, P)$, facilitates the determination and estimation of the eigenvalues of the system. The Jacobian matrix is expressed as follows:

$$J = \begin{bmatrix} -\sigma+\mu & 0 & 0 & \rho_1 S & 0 & 0 & \rho_2 S \\ \sigma & -\mu & 0 & 0 & 0 & 0 & 0 \\ 0 & 0 & -(\tau+\mu) & 0 & 0 & 0 & 0 \\ 0 & 0 & \tau & -(a\gamma+(1-a)\gamma+\mu+\delta_2) & 0 & 0 & 0 \\ 0 & 0 & 0 & (1-a)\gamma & -(\theta_2+\mu+\delta_2) & 0 & 0 \\ 0 & 0 & 0 & a\gamma & \theta_2 & -\mu & 0 \\ 0 & 0 & 0 & \delta_1 & 0 & \delta_2 & -(\mu_p+\eta-\xi) \end{bmatrix} \quad \textbf{(17)}$$

Now, we calculate the eigenvalue, $|J-\lambda I|=0$, where λ represents our eigenvalue.

$$|J-\lambda I| = \begin{vmatrix} -(\mu-\sigma)-\lambda & 0 & 0 & \rho_1 S & 0 & 0 & \rho_2 S \\ \sigma & -\mu-\lambda & 0 & 0 & 0 & 0 & 0 \\ 0 & 0 & -(\tau+\mu)-\lambda & 0 & 0 & 0 & 0 \\ 0 & 0 & \tau & -(a\gamma+(1-a)\gamma+\mu+\delta_2)-\lambda & 0 & 0 & 0 \\ 0 & 0 & 0 & (1-a)\gamma & -(\theta_2+\mu+\delta_2)-\lambda & 0 & 0 \\ 0 & 0 & 0 & a\gamma & \theta_2 & -\mu-\lambda & 0 \\ 0 & 0 & 0 & \delta_1 & 0 & \delta_2 & -(\mu_p+\eta-\xi)-\lambda \end{vmatrix} \tag{18}$$

The eigenvalues of matrix $J(S, V, L, A, T, R, P)$, as depicted in the provided matrix, serve as crucial indicators of system dynamics. It is evident that these eigenvalues solely consist of real values, without any presence of imaginary components. The indication of these eigenvalues holds significant epidemiological ramifications, particularly when assessing the stability of the Disease-Free Equilibrium (DFE). Notably, in this context, all eigenvalues exhibit negative real components, affirming the local asymptotic stability of the model at the DFE.

2.4.2 Analysis of global stability of disease-free equilibrium (DFE)

Theorem 4:

The globally asymptotically stable non-negative equilibrium point of model (2) is guaranteed to be attained under conditions where $G^0 > 1$.

V,

Proof:

In order to assess the worldwide stability of this equilibrium E^0, we construct the ensuing Lyapunov function employing the specified approach.

$$\begin{aligned} &G(S,V,L,A,T,R,P) = \\ &\left(S - S^0 - S^0 \log \frac{S^0}{S}\right) + \left(V - V^0 - V^0 \log \frac{V^0}{V}\right) + \left(L - L^0 - L^0 \log \frac{L^0}{L}\right) \\ &+ \left(A - A^0 - A^0 \log \frac{A^0}{A}\right) + \left(T - T^0 - T^0 \log \frac{T^0}{T}\right) + \left(P - P^0 - P^0 \log \frac{P^0}{p}\right) \end{aligned} \tag{19}$$

The derivative of G along the solution path of (2) can be obtained through direct calculation as follows:

$$\frac{dG}{dt}=\left(\frac{S-S^0}{S}\right)+\left(\frac{V-V^0}{V}\right)+\left(\frac{L-L^0}{L}\right)+\left(\frac{A-A^0}{A}\right)+\left(\frac{T-T^0}{T}\right)+\left(\frac{R-R^0}{R}\right) \quad (20)$$

We proceed to extend the aforementioned equation and partition it into distinct positive and negative components. Let the positive term be symbolized as P_t, and the negative term as N_t. Consequently, we derive:

$$\frac{dG}{dt}=P_t-N_t$$

$$S=\left(1-\frac{S^0}{S}\right)(\omega+\sigma+\mu)+\left(1-\frac{V^0}{V}\right)\mu+\left(1-\frac{L^0}{L}\right)(\tau+\mu)+\left(1-\frac{A^0}{A}\right)(a\gamma+(1-a)\gamma+\mu+\delta_1)+\left(1-\frac{T^0}{T}\right)(\theta_2+\mu+\delta_2)+\left(1-\frac{P^0}{P}\right)(\mu_p+\eta-\xi) \quad (21)$$

Similarly,

$$E=\frac{(S-S^0)^2}{S}(\phi_2+\mu_P)+\frac{(V-V^0)^2}{V}(\theta_1+\theta_1+\mu_P)+\frac{(L-L^0)^2}{L}(\mu_P+\delta_P+(1-\alpha_1)\theta_4+\alpha_1\theta_3)+\frac{(A-A^0)^2}{A}(\mu_P+\delta_P+\alpha_2)+\frac{(T-T^0)^2}{T}(\mu_P+\delta_P+\theta_5)+\frac{(P-P^0)^2}{P}(\phi_1+\mu_H) \quad (22)$$

Given the condition that $P_t<N_t$, it follows that $\frac{dG}{dt}$ will exhibit negativity definiteness along the trajectory of the solution space of the system. Consequently, this implies that exclusively at the Disease-Free Equilibrium (E0), $\frac{dG}{dt}\le 0$ will hold. This observation suggests the global stability of the system at the Disease-Free Equilibrium

2.4.3 The presence of the endemic equilibrium points

In this investigation, we delve into the analysis of endemic equilibrium configurations, denoting stable solutions inherent to the model, wherein Hepatitis A and E endure within the populace perpetually. These equilibrium points denote the steady disease states where the number of infected individuals and other compartments stabilizes.

The endemic equilibrium points are defined as $\left(S^*(t), 0, 0, 0, 0, 0, 0\right)$ that satisfy $S' = V' = L' = A' = T' = R' = P' = 0$. By setting equation (2) to 0, we have

$$\left.\begin{array}{l} 0 = (1-\phi)\Gamma - (\omega + \sigma + \mu)S^* \\ 0 = \phi\Gamma + \sigma S^* - \mu V^* \\ 0 = \omega S^* - (\tau + \mu)L^* \\ 0 = \tau L^* - (a\gamma + (1-a)\gamma + \mu + \delta_1)A^* \\ 0 = (1-a)\gamma A^* - (\theta_2 + \mu + \delta_2)T^* \\ 0 = a\gamma A^* + \theta_2 T^* - \mu R^* \\ 0 = \delta_1 A^* + \delta_2 R^* - \left(\mu_p + \eta - \xi\right)P^* \end{array}\right\} \quad \textbf{(23)}$$

Where $\omega = \rho_1 A + \rho_2 P$

$$S^* = \frac{(1-\phi)\Gamma}{(\omega + \sigma + \mu)};\; V^* = \frac{(\phi\Gamma + \sigma)(1-\phi)\Gamma}{\mu(\omega + \sigma + \mu)};\; L^* = \frac{\omega(1-\phi)\Gamma}{(\tau + \mu)(\omega + \sigma + \mu)}$$

$$A^* = \frac{\tau\omega(1-\phi)\Gamma}{(a\gamma + (1-a)\gamma + \mu + \delta_1)(\tau + \mu)(\omega + \sigma + \mu)};$$

$$T^* = \frac{(1-a)\gamma\tau\omega(1-\phi)\Gamma}{(\theta_2 + \mu + \delta_2)(a\gamma + (1-a)\gamma + \mu + \delta_1)(\tau + \mu)(\omega + \sigma + \mu)};$$

$$R^* = \frac{a\gamma\tau\omega(1-\phi)\Gamma}{\mu(a\gamma + (1-a)\gamma + \mu + \delta_1)(\tau + \mu)(\omega + \sigma + \mu)} + \frac{\theta_2(1-a)\gamma\tau\omega(1-\phi)\Gamma}{\mu(\theta_2 + \mu + \delta_2)(a\gamma + (1-a)\gamma + \mu + \delta_1)(\tau + \mu)(\omega + \sigma + \mu)} \quad \textbf{(24)}$$

$$P^* = \frac{1}{\left(\mu_p + \eta - \xi\right)}\left(\begin{array}{l} \delta_1\left(\dfrac{\tau\omega(1-\phi)\Gamma}{(a\gamma + (1-a)\gamma + \mu + \delta_1)(\tau + \mu)(\omega + \sigma + \mu)}\right) \\ + \delta_2\left(\begin{array}{l} \dfrac{a\gamma\tau\omega(1-\phi)\Gamma}{\mu(a\gamma + (1-a)\gamma + \mu + \delta_1)(\tau + \mu)(\omega + \sigma + \mu)} \\ + \dfrac{\theta_2(1-a)\gamma\tau\omega(1-\phi)\Gamma}{\mu(\theta_2 + \mu + \delta_2)(a\gamma + (1-a)\gamma + \mu + \delta_1)(\tau + \mu)(\omega + \sigma + \mu)} \end{array}\right) \end{array}\right)$$

Employing conventional methodologies, the model demonstrates disease-free dynamics at equilibrium point E^0.

2.5 Sensitivity Analysis of the Model

This section focuses on performing a sensitivity analysis of the model, wherein the impact of parameter fluctuations on model prognostications is investigated. The aim is to identify significant parameters, elucidate their impact, and enhance the model's robustness.

In sensitivity analysis, a comprehensive exploration is conducted wherein parameters are systematically varied within their respective feasible ranges, while meticulously observing the consequent dynamics of the model. Such variation can be executed either in isolation (commonly denoted as one-at-a-time sensitivity analysis) or collectively (referred to as global sensitivity analysis) for multiple parameters concurrently.

We conducted an assessment of the model's reproductive ratio R_n to evaluate variations and the impact of parameter alterations (Table 2) and the results graphically displaced in figure 2.

2.5.1 Definition

The elucidation of the Normalized Forward-Sensitivity Index concerning variable V, dependent on parameter U, is expounded upon as follows:

$$X_U^V = \frac{\partial V}{\partial U} \cdot \frac{U}{V} \tag{25}$$

In reference to the model parameters, we shall undertake the computation of sensitivity indices pertaining to the basic reproductive ratio, designated as R_n.

2.5.2 Sensitivity index for Γ

The calculated metric denoted as the Normalized Forward-Sensitivity Index for λ is expressed as:

$$X_\Gamma^{R_n} = \frac{\partial R_n}{\partial \Gamma} \cdot \frac{\Gamma}{R_n} \tag{26}$$

$$R_n = \frac{\tau(1-\phi)\Gamma}{\mu(\tau+\mu)(a\gamma+(1-a)\gamma+\mu+\delta_1)}\left(\rho_1+\frac{\delta_1\rho_2}{(\mu_p+\eta-\xi)}\right)$$

Evaluating the derivatives in equation (43), we obtain:

$$\frac{\partial R_n}{\partial \Gamma} = \frac{1}{\Gamma} R_n \tag{27}$$

Then,

$$X_{\Gamma}^{R_n} = \frac{\partial R_n}{\partial \Gamma}.\frac{\Gamma}{R_n} = \frac{1}{\Gamma} R_n.\frac{\Gamma}{R_n}$$

$$\therefore X_{\Gamma}^{R_n} = +1 \tag{28}$$

This gives us the sensitivity index Γ.

The sensitivity analyses for the remaining parameters contributing to the basic reproductive ratio are conducted using a standardized methodology, ensuring uniformity in the computational process. Consequently, the sensitivity measures for these parameters are delineated as follows:

Table 2*. Indices of sensitivity regarding additional parameters within the framework of the basic reproductive rate are assessed.*

Variables	Values	Index indicator
ϕ	-0.6666667	-
Γ	1	+
ρ_1	0.5238095238	+
ρ_2	0.4761904762	+
μ	-1.081097152	-
τ	0.07918968688	+
a	0.00000	+
γ	-0-1108991705	-
δ_1	-0.4110028875	-
μ_p	-0.2245670995	-
η	-0.4491341991	-
ξ	0.1975108225	+

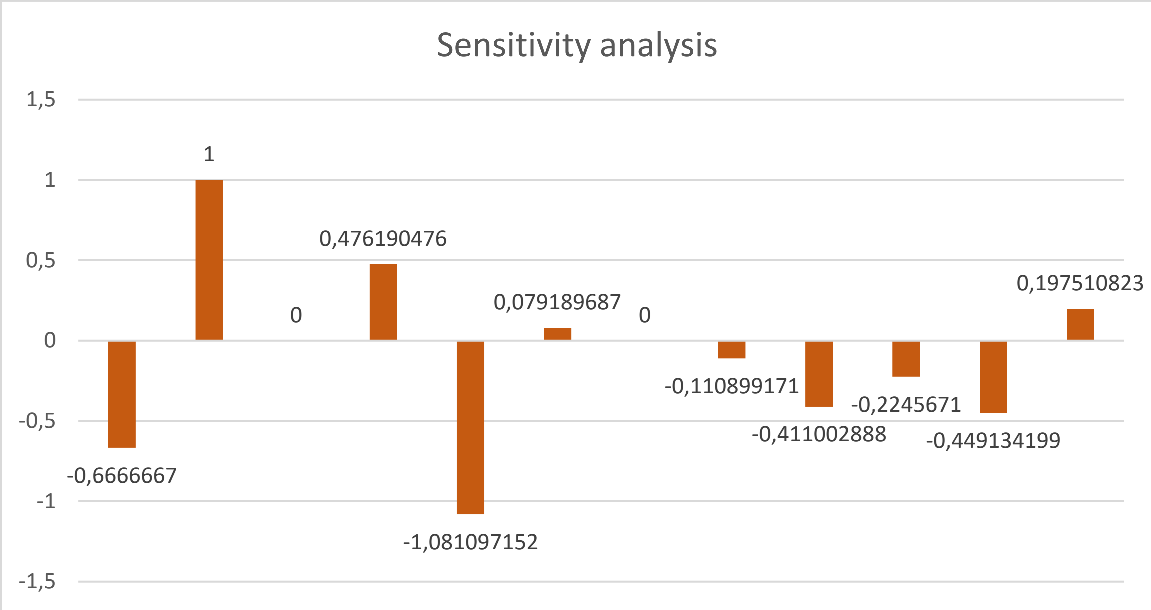

***Figure 2**. Sensitivity analysis.*

2.5.3 Interpretation of sensitivity analysis

A sensitivity index with a negative value signifies an inverse correlation between the parameter R_n (Table 2). Conversely, a sensitivity index with a positive value indicates that an increment in the parameter value results in a corresponding elevation in R_n. This analytical approach aids in discerning the parameters exerting significant influence on the outcomes of our analysis.

2.6 Optimal Strategies for Controlling the Model

The aim is to curtail disease transmission and its repercussions, considering resource constraints and optimizing the implementation of available interventions. These strategies typically entail a blend of preventive measures, surveillance, vaccination initiatives, and prompt case management. Several key components contribute to effective hepatitis control measures. These encompass adjusting transmission dynamics by lowering transmission rates through interventions such as health education $(1-\vartheta_1)$ campaigns, where ϑ_1 denotes health education and awareness. These public health endeavors raise awareness about hepatitis A and E transmission routes and preventive measures, thereby empowering individuals and communities to safeguard against infection. Vaccination campaigns target susceptible individuals (ϑ_2), while treatment efforts focus on acute cases (ϑ_3).

Sanitation initiatives (ϑ_4) address the removal of pathogens, further contributing to disease control. Building upon these foundations, we formulate a set of novel equations:

Building upon these premises, we formulate the following set of novel equations:

$$\left.\begin{aligned}
\frac{dS}{dt} &= (1-\phi)\Gamma - ((1-\vartheta_1)(\rho_1 A + \rho_2 P) + \vartheta_2 + \mu)S \\
\frac{dV}{dt} &= \phi\Gamma + \vartheta_2 S - \mu V \\
\frac{dL}{dt} &= (1-\vartheta_1)(\rho_1 A + \rho_2 P)S - (\tau + \mu)L \\
\frac{dA}{dt} &= \tau L - (a\vartheta_3 + (1-a)\vartheta_3 + \mu + \delta_1)A \\
\frac{dT}{dt} &= (1-a)\vartheta_3 A - (\theta_2 + \mu + \delta_2)T \\
\frac{dR}{dt} &= a\vartheta_3 A + \theta_2 T - \mu R \\
\frac{dP}{dt} &= \delta_1 A + \delta_2 R - (\mu_p + \vartheta_4 - \xi)P
\end{aligned}\right\} \qquad \textbf{(29)}$$

2.7 Examination of the Model Integrating Preventive Interventions

In this segment, we have developed a structured model, placing significant focus on leveraging Pontryagin's Maximum Principle for potential manipulation. Emphasizing the optimal solution delineated in equation set (29), a significant concern related to control has been identified and subsequently expounded upon before embarking on its comprehensive global optimization. The intricate process of selecting the most effective strategies is encapsulated by the objective function represented as F. The primary objective is to minimize the population susceptible to, exposed to, and affected by the disease, covering both asymptomatic and symptomatic cases, over a specified time interval [0, T].

Let $W = \{(\vartheta_1, \vartheta_2, \vartheta_3, \vartheta_4) \in W\}$ define over a Lebesgue measurable set on $[0,1]$

For $0 \le \vartheta_i(t) \le 1 \in [0,1], i = 1, 2, 3, 4$

Subsequently, the establishment of the objective function, designated as G, is undertaken.

$$G(\vartheta_1,\vartheta_2,\vartheta_3,\vartheta_4)=\int_0^T\left(Q_1L+Q_2V+Q_3T+Q_4P+\frac{1}{2}\left(V_1\vartheta_1^{\,2}+V_2\vartheta_2^{\,2}+V_3\vartheta_3^{\,2}+V_4\vartheta_4^{\,2}\right)\right)dt \quad \textbf{(30)}$$

Constraint to

$$\left.\begin{aligned}
\frac{dS}{dt}&=(1-\phi)\Gamma-((1-\vartheta_1)(\rho_1A+\rho_2P)+\vartheta_2+\mu)S\\
\frac{dV}{dt}&=\phi\Gamma+\vartheta_2S-\mu V\\
\frac{dL}{dt}&=(1-\vartheta_1)(\rho_1A+\rho_2P)S-(\tau+\mu)L\\
\frac{dA}{dt}&=\tau L-(a\vartheta_3+(1-a)\vartheta_3+\mu+\delta_1)A\\
\frac{dT}{dt}&=(1-a)\vartheta_3A-(\theta_2+\mu+\delta_2)T\\
\frac{dR}{dt}&=a\vartheta_3A+\theta_2T-\mu R\\
\frac{dP}{dt}&=\delta_1A+\delta_2R-(\mu_p+\vartheta_4-\xi)P
\end{aligned}\right\} \quad \textbf{(31)}$$

The parameter denoting the final time point is represented by T, with coefficients Q_1 through Q_4 signifying the weight coefficients assigned to the virus across various demographic categories, including latent classes, vaccinated individuals, treatment of acute individuals, and pathogens.

The primary focus of this section is to reduce operational costs, as outlined in equation (30). Additionally, our investigation extends to encompass an analysis of the social and economic implications $V_1\vartheta_1^{\,2}, V_2\vartheta_2^{\,2}, V_3\vartheta_3^{\,2}$, and $V_4\vartheta_4^{\,2}$ linked to the outlined scenario.

In pursuit of addressing the control challenge, our endeavors are aimed at understanding the functionalities.

$\left(\vartheta_1^*(t),\vartheta_2^*(t),\vartheta_3^*(t),\vartheta_4^*(t)\right)$ such that

$$G\left(\vartheta_1^*(t),\vartheta_2^*(t),\vartheta_3^*(t),\vartheta_4^*(t)\right)=\min\left\{G(\vartheta_1,\vartheta_2,\vartheta_3,\vartheta_4),(\vartheta_1,\vartheta_2,\vartheta_3,\vartheta_4)\in W\right\} \quad \textbf{(32)}$$

2.7.1 The presence of an optimal control solution

Theorem:

Following equation (30), it is crucial to examine $G(\vartheta_1, \vartheta_2, \vartheta_3, \vartheta_4)$ within the constraints specified in (31), with t=0 representing the initial condition. Thus, in determining the optimal control, ensuring the aforementioned condition to be $\vartheta^* = \vartheta_1^*(t), \vartheta_2^*(t), \vartheta_3^*(t), \vartheta_4^*(t)$ is imperative.

$$G(\vartheta_1^*(t), \vartheta_2^*(t), \vartheta_3^*(t), \vartheta_4^*(t)) = \min \{G(\vartheta_1, \vartheta_2, \vartheta_3, \vartheta_4), (\vartheta_1, \vartheta_2, \vartheta_3, \vartheta_4) \in W\}$$

Proof:

Due to the convexity exhibited by the integrand G regarding control measures $\vartheta_1, \vartheta_2, \vartheta_3, \vartheta_4$, the presence of an optimal control solution is guaranteed.

Subsequently, it is crucial to elucidate the most effective remedy. The Lagrangian function is formulated as follows:

$$L = Q_1 L + Q_2 V + Q_3 T + Q_4 P + \frac{1}{2}\left(V_1 \vartheta_1^2 + V_2 \vartheta_2^2 + V_3 \vartheta_3^2 + V_4 \vartheta_4^2\right) \quad \textbf{(33)}$$

The Hamiltonian function is given as;

$$\begin{aligned}
\Pi = {} & Q_1 L + Q_2 V + Q_3 T + Q_4 P + \frac{1}{2}\left(V_1 \vartheta_1^2 + V_2 \vartheta_2^2 + V_3 \vartheta_3^2 + V_4 \vartheta_4^2\right) \\
& + \Omega_S\left[(1-\phi)\Gamma - ((1-\vartheta_1)(\rho_1 A + \rho_2 P) + \vartheta_2 + \mu)S\right] \\
& + \Omega_V\left[\phi\Gamma + \vartheta_2 S - \mu V\right] \\
& + \Omega_L\left[(1-\vartheta_1)(\rho_1 A + \rho_2 P)S - (\tau + \mu)L\right] \\
& + \Omega_A\left[\tau L - (a\vartheta_3 + (1-a)\vartheta_3 + \mu + \delta_1)A\right] \\
& + \Omega_T\left[(1-a)\vartheta_3 A - (\theta_2 + \mu + \delta_2)T\right] \\
& + \Omega_R\left[a\vartheta_3 A + \theta_2 T - \mu R\right] \\
& + \Omega_P\left[\delta_1 A + \delta_2 R - (\mu_p + \vartheta_4 - \xi)P\right]
\end{aligned} \quad \textbf{(34)}$$

Given $\Omega_k, k \in \{S, V, L, A, T, R, P\}$ are distinct and non-overlapping variables.

Currently, we are poised to implement the requisite variables into the Hamiltonian Π for thorough examination.

In our pursuit of clarifying the adjoint equation and satisfying the transversality condition, we employ the Hamiltonian function Π as our analytical instrument. Through differential calculus, we ascertain the derivatives of the variables S,V,L,A,T,R,P relative to the Hamiltonian. This methodical process results in the derivation of the adjoint equation, as presented below:

$$\begin{aligned}
\frac{d\Omega_S}{dt} &= -\frac{\partial\Pi}{dS} = \begin{bmatrix} \Omega_S\left[\left((1-\vartheta_1)(\rho_1 A+\rho_2 P)+\vartheta_2+\mu\right)\right]-\Omega_V\left[\vartheta_2\right] \\ -\Omega_L\left[(1-\vartheta_1)(\rho_1 A+\rho_2 P)\right] \end{bmatrix} \\
\frac{d\Omega_V}{dt} &= \frac{-\partial\Pi}{dV} = \left[-Q_2 V+\Omega_V[\mu]\right] \\
\frac{d\Omega_L}{dt} &= -\frac{\partial\Pi}{dL} = \left[\Omega_L[(\tau+\mu)]-\Omega_A[\tau]\right] \\
\frac{d\Omega_A}{dt} &= -\frac{\partial\Pi}{dA} = \begin{bmatrix} \Omega_S\left[(1-\vartheta_1)\rho_1 S\right]-\Omega_L\left[(1-\vartheta_1)\rho_1 S\right]+\Omega_A\left[(a\vartheta_3+(1-a)\vartheta_3+\mu+\delta_1)\right] \\ -\Omega_T\left[(1-a)\vartheta_3\right]-\Omega_R\left[a\vartheta_3\right]-\Omega_P\left[\delta_1\right] \end{bmatrix} \\
\frac{d\Omega_T}{dt} &= -\frac{\partial\Pi}{dT} = \left[-Q_3+\Omega_T[(\theta_2+\mu+\delta_2)]-\Omega_R[\theta_2]\right] \\
\frac{d\Omega_R}{dt} &= -\frac{\partial\Pi}{dR} = \left[\Omega_R[\mu]-\Omega_P[\delta_2]\right] \\
\frac{d\Omega_P}{dt} &= -\frac{\partial\Pi}{dP} = \left[-Q_4+\Omega_S\left[(1-\vartheta_1)\rho_2 S\right]-\Omega_L\left[(1-\vartheta_1)\rho_2 S\right]+\Omega_P\left[(\mu_p+\vartheta_4-\xi)P\right]\right]
\end{aligned} \quad \textbf{(35)}$$

Given the conditions of transversally to be $\Omega_k(T)=0, k\in\{S,V,L,A,T,R,P\}$.

In the quest for minimizing the Hamiltonian, symbolized as H, concerning the optimal control variables, we engage in the differentiation process with respect to $\vartheta_1,\vartheta_2,\vartheta_3,\vartheta_4$. This yields a set of equations, which we subsequently equate to zero to determine the optimal control configuration. This methodology culminates in the attainment of the desired optimal control solution.

With $S=S^*,V=V^*,L=L^*,A=A^*,T=T^*,R=R^*,P=P^*$

Then, we have

$$\begin{aligned}
\frac{d\Pi}{d\vartheta_1} &= V_1\vartheta_1^{*}-(\rho_1 A+\rho_2 P)S(\Omega_L-\Omega_S)=0 \\
\frac{d\Pi}{d\vartheta_2} &= V_2\vartheta_2^{*}-(\Omega_S-\Omega_V)S=0 \\
\frac{d\Pi}{d\vartheta_3} &= V_3\vartheta_3^{2}-(1-a)A(\Omega_A-\Omega_T)-aA(\Omega_A-\Omega_R)=0 \\
\frac{d\Pi}{d\vartheta_4} &= V_4\vartheta_4^{*}-\Omega_P P=0
\end{aligned} \quad \textbf{(36)}$$

By simplifying the expressions, we arrive at a solution for the optimal control strategy.

$$\begin{aligned}
\vartheta_1^* &= \frac{(\rho_1 A + \rho_2 P)S(\Omega_L - \Omega_S)}{V_1} \\
\vartheta_2^* &= \frac{(\Omega_S - \Omega_V)S}{V_2} \\
\vartheta_3^* &= \frac{(1-a)A(\Omega_A - \Omega_T) + aA(\Omega_A - \Omega_R)}{V_3} \\
\vartheta_4^* &= \frac{\Omega_P P}{V_4}
\end{aligned} \tag{37}$$

Applying the boundary conditions, the solution is provided as follows.

$$\begin{aligned}
\vartheta_1 &= \min\left\{1, \max\left\{0, \frac{(\rho_1 A + \rho_2 P)S(\Omega_L - \Omega_S)}{V_1}\right\}\right\}, \\
\vartheta_2 &= \min\left\{1, \max\left\{0, \frac{(\Omega_S - \Omega_V)S}{V_2}\right\}\right\}, \\
\vartheta_3 &= \min\left\{1, \max\left\{0, \frac{(1-a)A(\Omega_A - \Omega_T) + aA(\Omega_A - \Omega_R)}{V_3}\right\}\right\}, \\
\vartheta_4 &= \min\left\{1, \max\left\{0, \frac{\Omega_P P}{V_4}\right\}\right\}.
\end{aligned} \tag{38}$$

Proved.

3 RESULTS

3.1 Numerical Simulation

In this computational model, we present a method to analyze the temporal propagation of the ailment, fluctuations across various parameters, and the evaluation of intervention effects. This facilitates researchers and public health officials in gaining insights into disease behavior across diverse scenarios and evaluating the efficacy of various control strategies.

Table 3. *Parameters with their values.*

Parameters	Values	Source
ϕ	0.4	S. E. Mwaijande et al. [2]
Γ	1000	S. E. Mwaijande et al. [2]
ϑ_1	0.99	Assumed
ρ_1	0.1	S. E. Mwaijande et al. [2]
ρ_2	0.2	S. E. Mwaijande et al. [2]
ϑ_2	0.9	Assumed
μ	0.00172	S. E. Mwaijande et al. [2]
τ	0.02	Assumed
a	0.02	Estimated
γ	0.1	Estimated
δ_1	0.8	Sholicah et al. [1]
θ_2	0.02	Estimated
δ_2	0.8	Sholicah et al. [1]
ϑ_3	0.5	Assumed
μ_p	0.83	S. E. Mwaijande et al. [2]
η	$2 \bullet \mu_p$	S. E. Mwaijande et al. [2]
ξ	0.73	S. E. Mwaijande et al. [2]

The state variables' initial conditions are as follows; $S(0)=1500,$ $E(0)=1400,$ $I_A(0)=880,$ $I_S(0)=550,$ $Q(0)=500,$ $I(0)=800,$ and $R(0)=1100$. The requisite parameter values essential for conducting the simulation are delineated within the confines of Table 3.

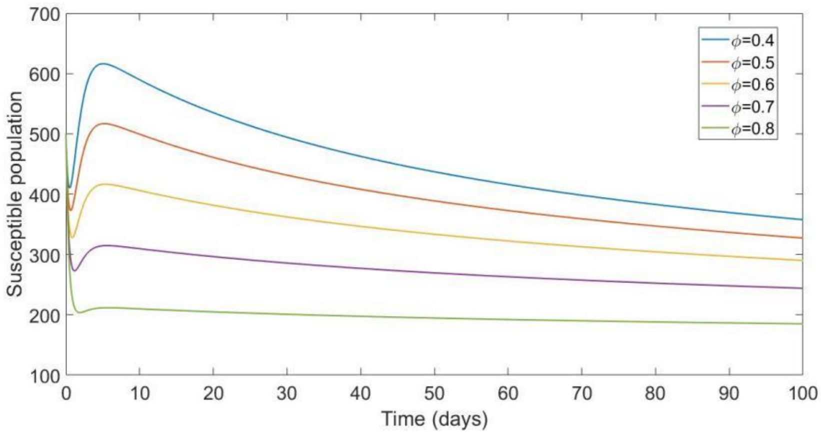

Figure 3. *Variation of susceptible population with different phi values.*

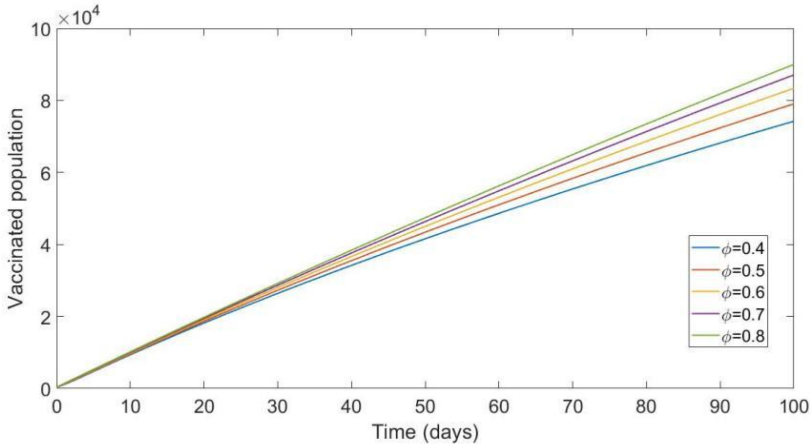

Figure 4*. Variation of vaccinated population with different phi values.*

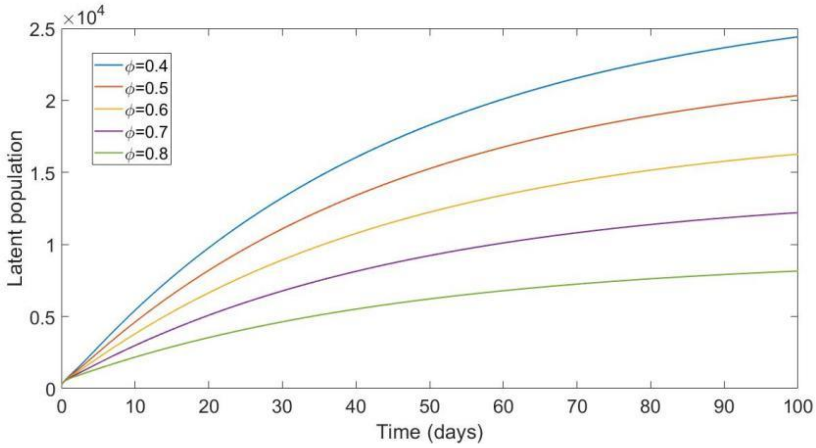

Figure 5. *Variation of latent population with different phi values.*

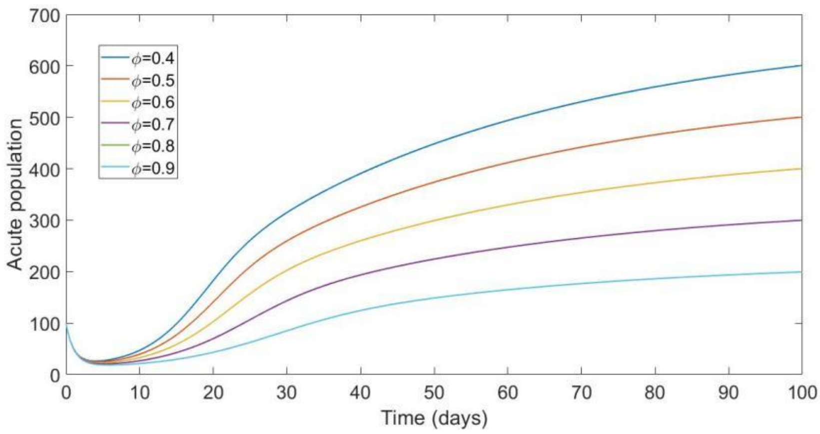

Figure 6. *Variation of acute population with different phi values.*

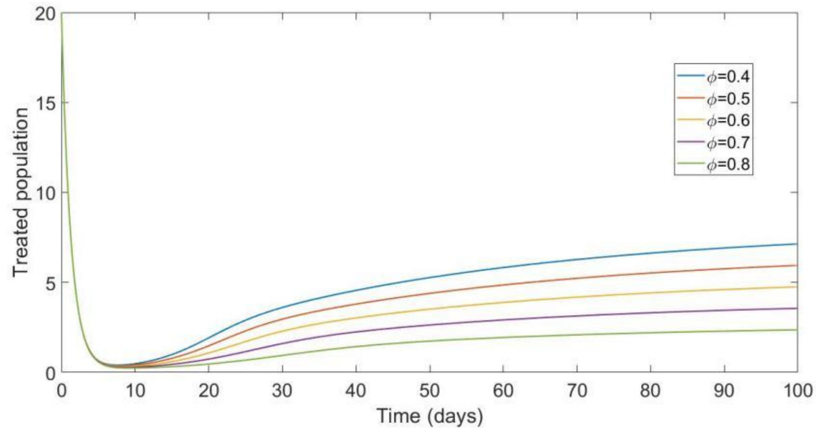

Figure 7*. Variation of treated population with different phi values.*

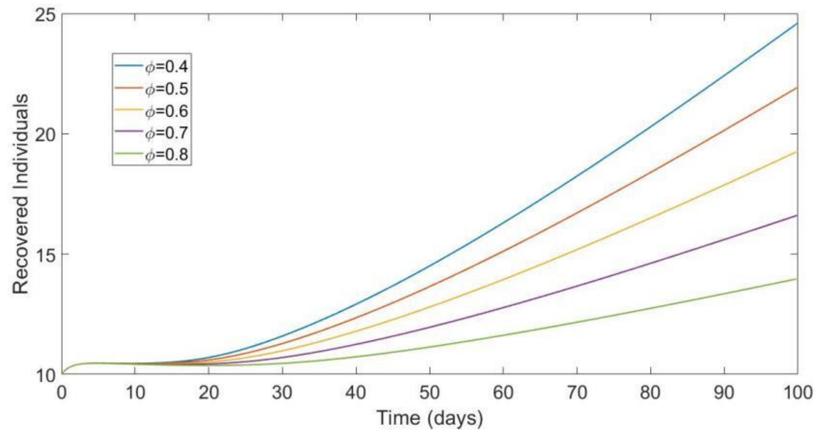

Figure 8*. Variation of recovered population with different phi values.*

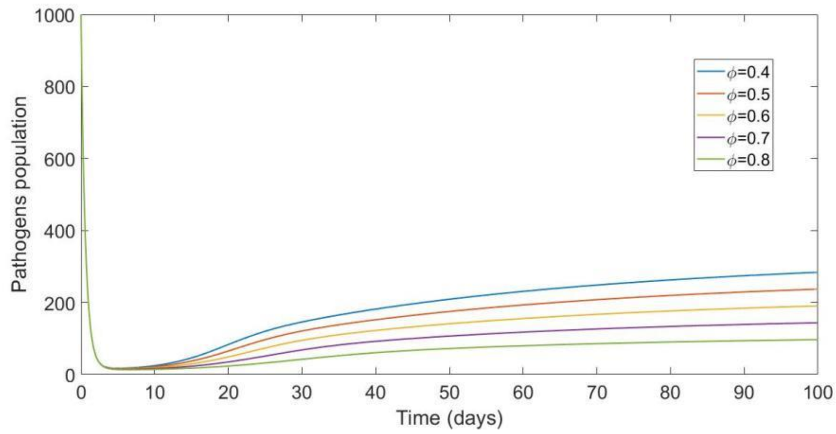

Figure 9*. Variation of pathogens population with different phi values.*

2. Figure 10 through Figure 12 shows the effect of the pathogens shed rate by the acute individuals in the water or food.

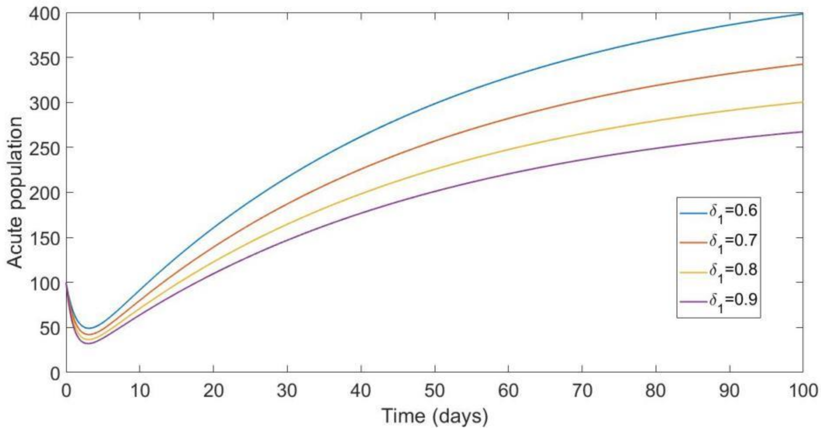

Figure 10*. Variation of acute population with different shed rates.*

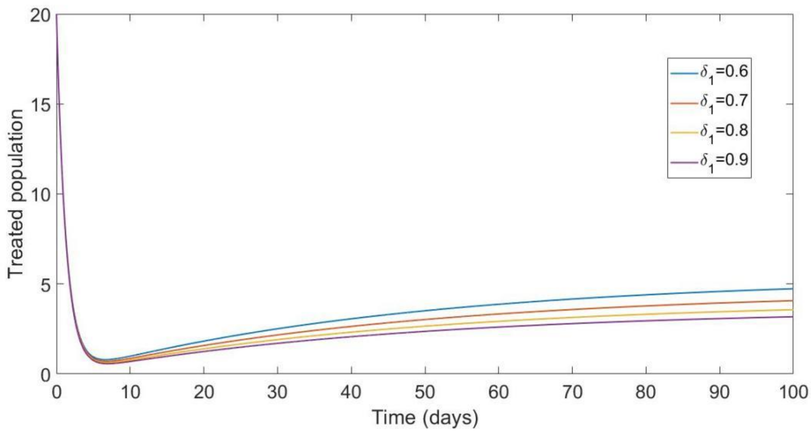

Figure 11*. Variation of treated population with different shed rates.*

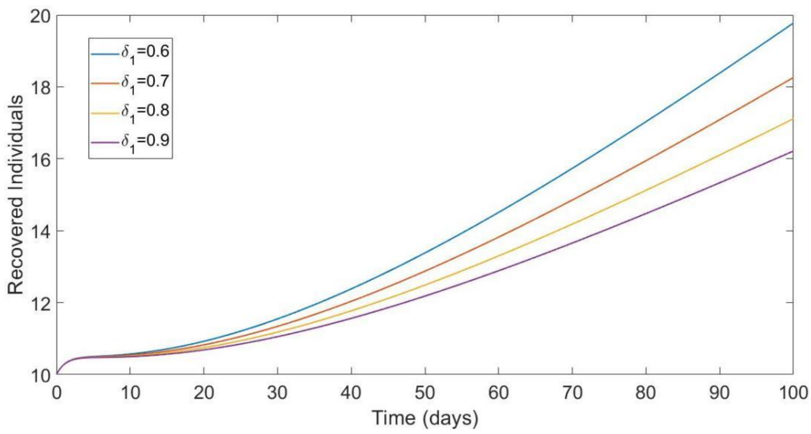

Figure 12*. Variation of recovered population with different shed rates.*

3. Figure 13 through Figure 19 shows the effect of the control strategies on the population.

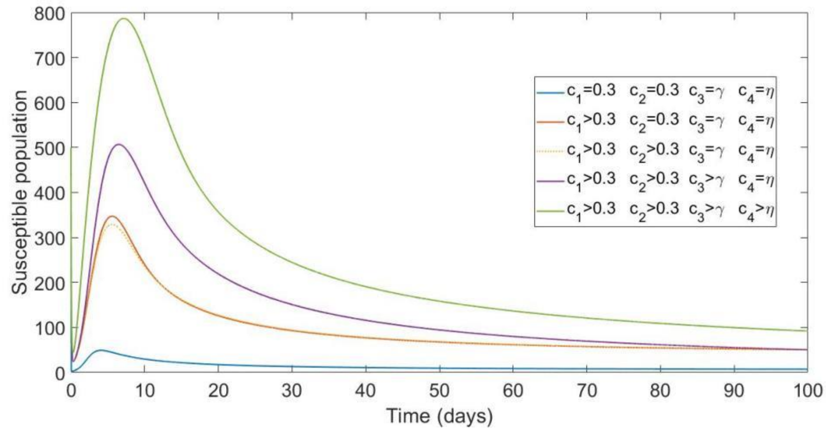

Figure 13. *Variation of susceptible population with control measures.*

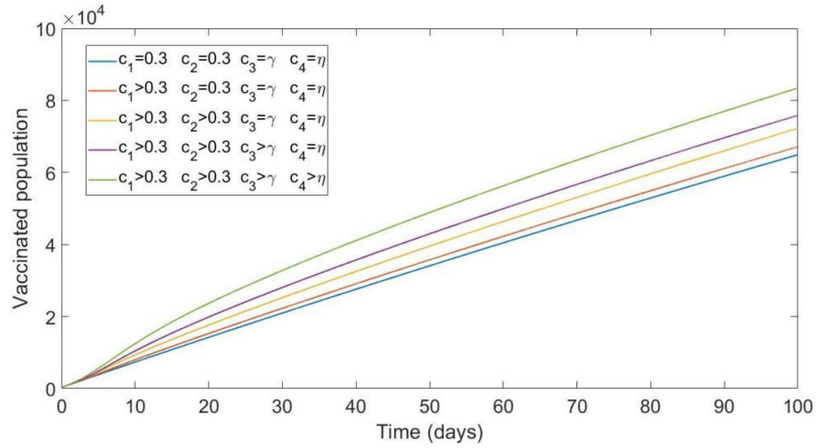

Figure 14. *Variation of vaccinated population with control measures.*

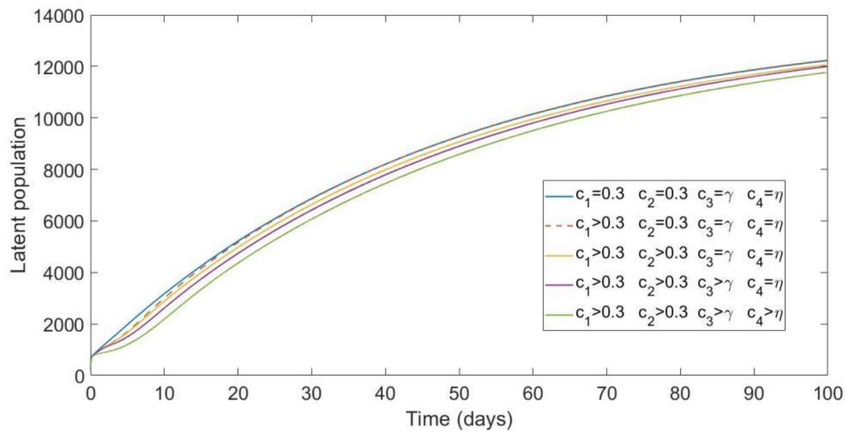

Figure 1 *Variation of latent population with control measures.*

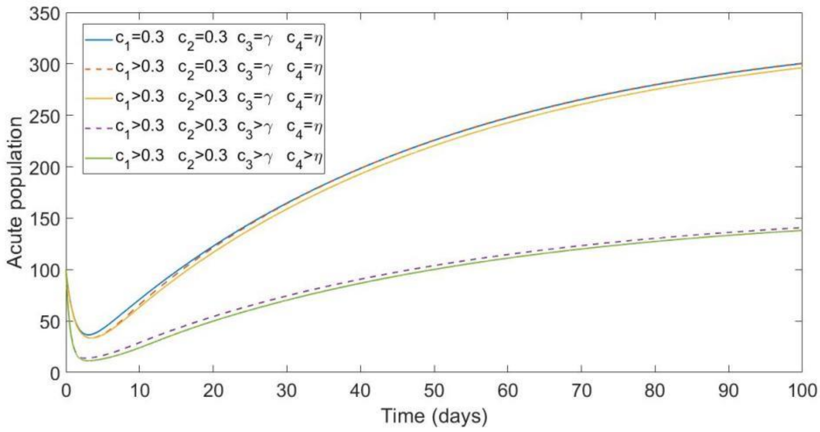

Figure 2 *Variation of acute population with control measures.*

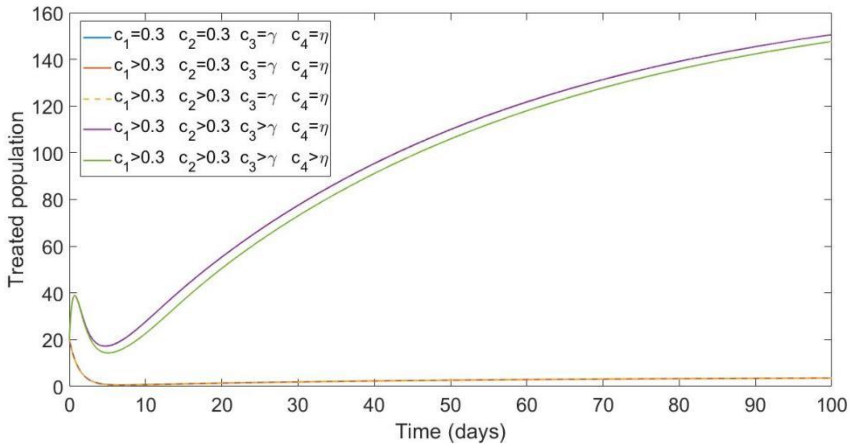

Figure 3*Variation of treated population with control measures.*

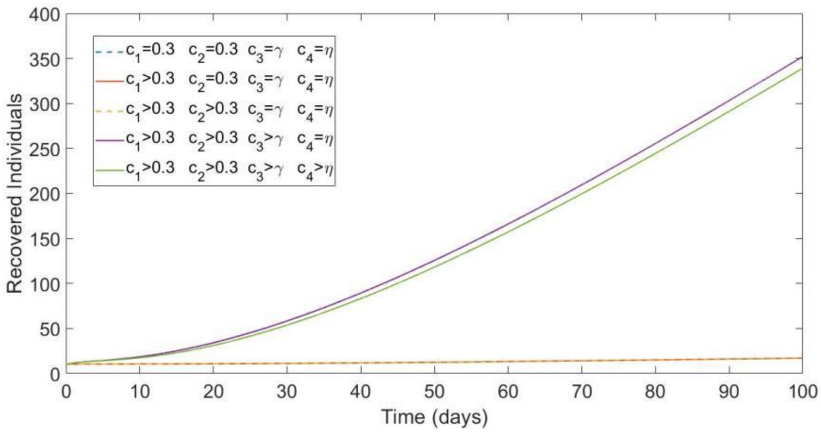

Figure 4*Variation of recovered population with control measures.*

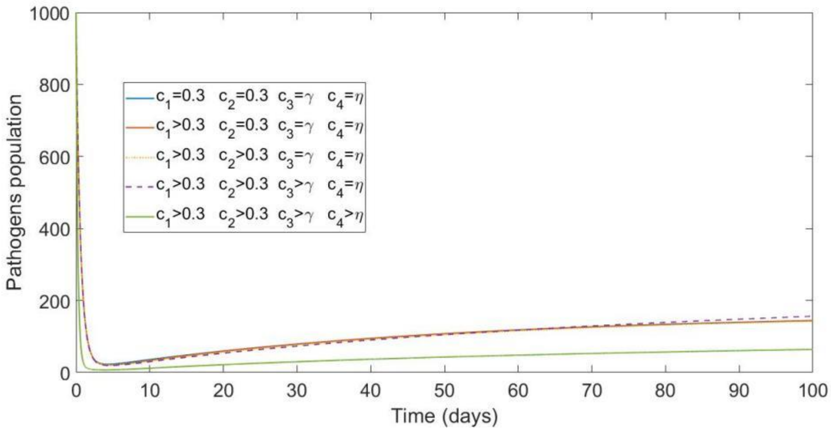

Figure 5*Variation of pathogens population with control measures.*

3.2 Discussion

Figure 3 depicts a decline in the susceptible population as the vaccination coverage increases. This trend aligns with expectations, as vaccination diminishes the pool of individuals vulnerable to infection. In Figure 4, the rise in the proportion of vaccinated susceptible corresponds with an uptick in the vaccinated population, indicating the efficacy of vaccination drives in augmenting the immunized cohort. Figure 5 illustrates a downturn in the latent population, suggesting the efficacy of vaccination in curbing the number of individuals exposed to infection but not yet symptomatic. This decline may signify either a direct impact of vaccination on transmission or an indirect effect stemming from the reduced pool of susceptible. Similarly, Figure 6 demonstrates that as the vaccination rate climbs, the count of individuals in the acute infection phase diminishes, hinting at vaccination's potential in mitigating the prevalence of actively infected individuals in the populace.

In Figure 7, the reduced incidence of acute infections due to vaccination results in fewer individuals necessitating treatment, implying that vaccination not only averts infection but also alleviates the strain on healthcare systems by decreasing the number of cases necessitating medical attention. Figure 8 showcases a decline in the recovered population, plausibly attributed to the reduction in the number of individuals contracting and subsequently recuperating from infections. This decline may stem from an overall reduction in infections owing to vaccination efforts. Moreover, Figure 9 reveals that the collective population of Hepatitis A and E pathogens within the community diminishes as vaccination diminishes the pool of susceptible individuals available for transmission, thus constraining the diseases' spread.

Figure 10 illustrates a negative correlation between the rate of pathogen excretion and the population of actively infected individuals displaying clinical symptoms. This correlation suggests that an increase in pathogen excretion leads to a decrease in the number of individuals manifesting acute symptoms. Correspondingly, Figure 11 indicates a reduction in the count of acutely infected individuals undergoing treatment as pathogen excretion rises. Figure 12 implies a decline in the overall count of recovered individuals, despite some recovering from the infection, possibly due to a higher rate of new infections outpacing the rate of recovery. These observations indicate that elevated pathogen excretion by individuals in the acute stage contributes to diminishing counts of acute infections, treated cases, and ultimately, recoveries. This underscores the necessity of regulating pathogen transmission to mitigate the spread of infectious diseases such as Hepatitis A and E. In Figure 13, the susceptible population experiences a noticeable increase, likely attributed to heightened awareness campaigns leading to heightened case reporting or a more accurate estimation of the true susceptible population due to enhanced surveillance. Figure 14 illustrates the positive impact of targeted vaccination efforts in augmenting the vaccinated population, thereby reducing the pool of susceptible individuals over time. Simultaneously, Figure 15 depicts a decline in the latent population, indicating the efficacy of control measures in restraining the transmission dynamics of Hepatitis A and E. Health education initiatives are presumed to play a crucial role in shortening the duration of individuals in the latent stage by advocating for early detection and diagnosis.

Moreover, Figure 16 illustrates a consistent decrease in the acute population, indicative of successful intervention strategies. Vaccination campaigns and treatment efforts synergistically act to mitigate the burden of acute infections, thereby limiting the propagation of the disease within the population. However, Figures 17 and 18 show nuanced responses of the treated and recovered populations, respectively, to the different control strategies. While the implementation of health education, vaccination, and treatment leads to an increase in both populations, the emphasis on sanitation appears to yield a reduction. This observation underscores the importance of a multifaceted approach in disease control, wherein sanitation efforts complement but do not replace other essential interventions aimed at treatment and prevention. Interestingly, Figure 19 reveals that the pathogen population experiences a significant reduction as control strategies intensify. This decline underscores the effectiveness of sanitation initiatives in mitigating environmental contamination and interrupting the transmission cycle of Hepatitis A and E. By targeting the removal of pathogens from water or food supplies, sanitation measures contribute substantially to disease control efforts.

Overall, findings underscore the transformative potential of multifaceted intervention strategies in taming Hepatitis A and E infections. Vaccination emerges as a cornerstone of disease control, reducing susceptibility and transmission rates. Concurrently, targeted treatment and health education initiatives bolster disease management and prevention efforts. Importantly, sanitation measures play a pivotal role in interrupting transmission cycles, mitigating environmental contamination, and enhancing overall disease control. This study represents a paradigm shift in public health dynamics, offering a holistic approach to infectious disease modeling and intervention design. By integrating mathematical modeling with real-world applications, this study provides actionable insights for policymakers, healthcare professionals, and public health practitioners. Findings herein pave the way for more effective, evidence-based strategies to combat Hepatitis A and E infections, ultimately advancing global health and well-being.

4 CONCLUSION

The analysis of the epidemiological dynamics of Hepatitis A and E infections demonstrates the critical importance of integrating diverse control strategies to mitigate the burden of these diseases on public health. This study highlights vaccination campaigns as a cornerstone for reducing the susceptible population, curtailing transmission, and alleviating pressure on healthcare systems. In tandem, health education initiatives play an essential role in fostering early detection, accurate diagnosis, and effective prevention, thereby curbing latent infections and empowering communities to adopt healthier behaviors.

The findings also underscore the efficacy of a multifaceted intervention framework, as reductions in acute infections and subsequent treatment needs highlight the synergistic effects of combining vaccination, treatment, and health education. While vaccination directly reduces the number of actively infected individuals, it also indirectly decreases the healthcare burden by minimizing the demand for treatment and related resources. However, the nuanced responses of treated and recovered populations to different measures emphasize the necessity of a balanced approach. Specifically, sanitation efforts emerge as a pivotal component for reducing environmental contamination, interrupting pathogen transmission cycles, and complementing other strategies such as vaccination and treatment.

Future research should build upon this comprehensive framework by exploring the long-term implications of these strategies under varying epidemiological and environmental conditions. Key areas for further study include:

-Model refinement: Incorporating more complex variables such as regional disparities, climate change effects, and socioeconomic factors to enhance predictive accuracy.

- Cost-effectiveness analysis: Evaluating the economic feasibility of different intervention strategies to guide policymakers in resource allocation.

- Dynamic intervention design: Investigating adaptive strategies that respond to real-time epidemiological data for improved disease management.

- Pathogen evolution: Studying the impact of mutations in Hepatitis A and E viruses on the effectiveness of current interventions.

- Community resilience: Assessing the role of integrated interventions in improving population resilience against future outbreaks.

In summary, this study provides a robust framework for understanding and controlling Hepatitis A and E infections. By emphasizing the importance of a coordinated and evidence-based approach, it lays a strong foundation for future research and public health initiatives aimed at reducing disease burden and safeguarding global health.

Acknowledgement

The author appreciates the extraordinary input of Sunday Gbodogbe.

Statement of Research and Publication ethics.

The study is compiled within research and publications ethics.

Artificial Intelligence (AI) Contribution Statement

This manuscript was entirely written, edited, analyzed, and prepared without the assistance of any artificial intelligence (AI) tools. All content, including text, data analysis, and figures, was solely generated by the author.

REFERENCES

[1] M. Sholikah, C. Alfiniyah and Miswanto, "Stability analysis and optimal control of mathematical model for the spread of hepatitis E," *Commun. Math. Biol. Neurosci.*, vol. 37, pp. 1–24, 2020.

[2] S. E. Mwaijande and G. E. Mpogolo, "Modeling the Transmission Dynamics of Hepatitis A with Combined Vaccination and Sanitation Mitigation," *Comput. Math. Methods Med.*, pp. 1-19, 2023.

[3] WHO, *A. Hepatitis and World Health Organization*, 2022. [Online]. Available: http://www.who.int/mediacentre/factsheets/fs328/en/.

[4] MMWR, "Prevention of hepatitis A through active or passive immunization: Recommendations of the Advisory Committee on Immunization Practices (ACIP)," *MMWR Recomm. Rep.*, vol. 48, no. 12, pp. 1-37, 1999.

[5] J. T. Stapleton and S. M. Lemon, "Infectious Diseases," in *Hepatitis A and Hepatitis E*, Lippincott Co, Philadelphia, US, pp. 790–797, 1994.

[6] J. L. Trujillo-Ochoa, O. Viera-Segura, and N. A. Fiery, "Challenges in management of hepatitis A virus epidemiological transition in Mexico," *Ann. Hepatol.*, vol. 18, no. 1, pp. 14-22, 2019.

[7] C. J. Staes, T. L. Schlenker, I. Risk et al., "Sources of infection among persons with acute hepatitis A and no identified risk factors during a sustained community-wide outbreak," *Pediatrics*, vol. 106, no. 4, p. E54, 2000.

[8] E. Bianco, A. Mariano, A. Mele, E. Spada, and M. Tosti, "Epidemiology of acute viral hepatitis: twenty years of surveillance through SEIEVA in Italy and a review of the literature," *Rapporti Istisan*, vol. 12, 2006.

[9] R. Aggarwal and S. Naik, "Epidemiology of hepatitis E: current status," *J. Gastroenterol. Hepatol.*, vol. 24, no. 9, pp. 1484–1493, 2009.

[10] J. Zuckerman, "Hepatitis Viruses," in *Medical Microbiology*, 4th ed., S. Baron, Ed. Galveston, TX: Univ. Texas Med. Branch, 1996, ch. 70. [Online]. Available: https://www.ncbi.nlm.nih.gov/books/NBK7864

[11] G. J. Ebrahim, "The Five Hepatitis Viruses," *J. Trop. Pediatr.*, vol. 57, no. 6, pp. 401-404, 2011.

[12] D. K. Owens et al., "Screening for Hepatitis B Virus Infection in Pregnant Women: U.S. Preventive Services Task Force Reaffirmation Recommendation Statement," *JAMA*, vol. 322, no. 4, pp. 349–354, 2019.

[13] A. C. Loyinmi, and S. O. Gbodogbe, "Epidemiological viability and control of rotavirus: A mathematical modelling approach," *Fnaps journal*, vol. 6, no. 2, pp. 18-43, 2025.

[14] R. Ragusa, L. S. Corsaro, E. Frazzetto, E. Bertino, M. A. Bellia and G. Bertino, "Hepatitis C Virus Infection in Children and Pregnant Women," *AJP Rep.*, vol. 10, no. 1, pp. 121–127, 2020.

[15] S. Saab, R. Kullar, C. Amini and P. Gounder, “The next frontier: universal hepatitis C virus screening in pregnant women,” *Am. J. Obstet. Gynecol.*, 2020, doi:10.1016/j.ajog.2020.01.058.

[16] T. Ahmad, J. Hui, T. H. Musa, M. Behzadifar and M. Baig, “Seroprevalence of hepatitis E virus infection in pregnant women: a systematic review and meta-analysis,” *Ann. Saudi Med.*, vol. 40, no. 2, pp. 136–146, 2020.

[17] M. S. Khuroo, S. Kamili and M. S. Khuroo, “Clinical course and duration of viremia in vertically transmitted hepatitis E virus (HEV) infection in babies born to HEV-infected mothers,” *J. Viral Hepat.*, vol. 16, no. 7, pp. 519–523, 2009.

[18] WHO, “Hepatitis E,” WHO, 2018. [Online]. Available: https://www.who.int/news-room/fact-sheets/detail/hepatitis-e [Accessed: Aug. 29, 2018].

[19] G. S. Oluwafemi, and A.C. Loyinmi, “Model of optimal control strategies for the transmission of diphtheria,” *Journal of Information & Optimization Sciences* ISSN 0252-2667 (Print), ISSN 2169-0103 (Online). Available: https://tarupublication.s3.ap-south-1.amazonaws.com/articles/jios-1587.pdf DOI : 10.47974/JIOS-1587

[20] H. Sooryanarain and X. J. Meng, “Swine hepatitis E virus: Cross-species infection, pork safety and chronic infection,” *Virus Res.*, vol. 284, 197985, 2020. doi:10.1016/j.virusres.2020.197985

[21] H. Ren, J. Li, Z. Yuan, J. Hu, Y. Yu and Y. Lu, “The development of a combined mathematical model to forecast the incidence of hepatitis E in Shanghai, China,” *BMC Infect. Dis.*, vol. 13, no. 421, 2013.

[22] WHO, “Viral hepatitis,” WHO, 2010. [Online]. Available: http://apps.who.int/gb/ebwha/pdf_files/A62/A62_22-en.pdf

[23] N. Chitnis, J. M. Hyman and J. M. Cushing, “Determining important parameters in the spread of malaria through the sensitivity analysis of a mathematical model,” *Bull. Math. Biol.*, vol. 70, no. 5, 2008.

[24] C. Loyinmi and A. L. Ijaola, “Investigating the effects of some control measures on the dynamics of diphtheria infection using fractional order model,” *Math. Comput. Sci.*, vol. 5, no. 4, pp. 26–47, 2024. doi:10.30511/MCS.2024.2032110.1183

[25] Castillo-Chavez and B. Song, “Dynamical models of tuberculosis and their applications,” *Math. Biosci. Eng.*, vol. 1, no. 2, pp. 361–404, 2004.

[26] S. O. Gbodogbe, “Harmonizing epidemic dynamics: A fractional calculus approach to optimal control strategies for cholera transmission,” *Sci. Afr.*, vol. 27, 2025.

[27] Korobeinikov, “Global properties of infectious disease models with non-linear incidence,” *Bull. Math. Biol.*, vol. 69, no. 6, 2007.

[28] J. T. Stapleton and S. M. Lemon, “Infectious Diseases, (Chapter) Hepatitis A and Hepatitis E,” Lippincott Co, Philadelphia, US, pp. 790–797, 1994.

[29] K. Ayouni et al., “Hepatitis A virus infection in Central-West Tunisia: an age structured model of transmission and vaccination impact,” *BMC Infect. Dis.*, vol. 20, no. 1, pp. 1–13, 2020.

[30] F. Brouwer et al., “The impact of vaccination efforts on the spatiotemporal patterns of the hepatitis A outbreak in Michigan, 2016–18,” *Epidemiology*, vol. 31, no. 5, 2020.

[31] T. Van Effelterre, C. Marano and K. H. Jacobsen, “Modeling the hepatitis A epidemiological transition in Thailand,” *Vaccine*, vol. 34, no. 4, pp. 555–562, 2016.

[32] M. Ajelli, L. Fumanelli, P. Manfredi and S. Merler, “Spatiotemporal dynamics of viral hepatitis A in Italy,” *Theor. Popul. Biol.*, vol. 79, no. 1–2, pp. 1–11, 2011.

[33] M. Ajelli, M. Iannelli, P. Manfredi and M. L. C. degli Atti, “Basic mathematical models for the temporal dynamics of HAV in medium-endemicity Italian areas,” *Vaccine*, vol. 26, no. 13, pp. 1697–1707, 2008.

[34] A. C. Loyinmi, and S. O. Gbodogbe, “Mathematical modeling and control strategies for Nipah virus transmission incorporating bat-to-pig-to-human pathway,” *EDUCATUM Journal of Science, Mathematics and Technology*, vol. 11, no. 1, pp. 54-80, 2024.

[35] E. Fiore, A. Wasley and B. P. Bell, “Prevention of hepatitis A through active or passive immunization: recommendations of the Advisory Committee on Immunization Practices (ACIP),” *MMWR Recomm. Rep.*, vol. 55, no. 7, 2006.

[36] T. P. Van Effelterre, T. K. Zink, B. J. Hoet, W. P. Hausdorff and P. A. Rosenthal, “Mathematical model of hepatitis A transmission in the United States indicates value of universal childhood immunization,” *Clin. Infect. Dis.*, vol. 43, no. 2, pp. 158–164, 2006.

[37] M. A. D. Guimaraens and C. T. Codeço, “Experiments with mathematical models to simulate hepatitis A population dynamics under different levels of endemicity,” *Cad. Saúde Pública*, vol. 21, no. 5, pp. 1531–1539, 2005.

[38] R. S. Koff, “Clinical manifestations and diagnosis of hepatitis A virus infection,” *Vaccine*, vol. 10, no. Suppl. 1, pp. S15–S17, 1992.

[39] S. Krugman and J. P. Giles, “Viral hepatitis,” *JAMA*, vol. 212, no. 6, pp. 1019–1029, 1970.

[40] C. J. Staes et al., “Sources of infection among persons with acute hepatitis A and no identified risk factors during a sustained community-wide outbreak,” *Pediatrics*, vol. 106, no. 4, 2006.

[41] C. Loyinmi, S. O. Gbodogbe and K. O. Idowu, “On the interaction of the human immune system with foreign body: Mathematical modelling approach,” *Kathmandu Univ. J. Sci. Eng. Technol.*, vol. 17, no. 2, pp. 1-17, 2023. [Online]. Available: https://journals.ku.edu.np/kuset/article/view/137

[42] K. M. Bisgard, A. Kao and J. Leake, “Haemophilus influenzae invasive disease in the United States, 1994–1995: near disappearance of a vaccine-preventable childhood disease,” *Emerg. Infect. Dis.*, vol. 4, pp. 229–237, 1998.

[43] B. P. Bell, D. Kruszon-Moran and C. N. Shapiro, “Hepatitis A virus infection in the United States: serologic results from the third national health and nutrition examination survey,” *Vaccine*, vol. 23, pp. 5798–5806, 2005.

[44] F. Averhoff, C. N. Shapiro and B. P. Bell, “Control of hepatitis A through routine vaccination of children,” *JAMA*, vol. 286, pp. 2968–2973, 2001.

[45] R. Singh, P. Preeti and A. A. Raina, “Markovian epidemic queueing model with exposed, infection and vaccination based on treatment,” *World Sci. News*, vol. 106, pp. 141–150, 2018.

[46] Din and Y. Li, “Optimizing HIV/AIDS dynamics: stochastic control strategies with education and treatment,” *Eur. Phys. J. Plus*, vol. 139, no. 9, p. 812, 2024.

[47] S. M. A. Shah, H. Tahir, A. Khan and A. Arshad, “Stochastic model on the transmission of worms in wireless sensor network,” *J. Math. Tech. Model.*, vol. 1, no. 1, pp. 75–88, 2024.

[48] Q. T. Ain, “Nonlinear stochastic cholera epidemic model under the influence of noise,” *J. Math. Tech. Model.*, vol. 1, no. 1, pp. 52–74, 2024.

[49] Din, “Bifurcation analysis of a delayed stochastic HBV epidemic model: Cell-to-cell transmission,” *Chaos Solitons Fractals*, vol. 181, 114714, 2024.

[50] S. Ullah, “Investigating a coupled system of Mittag-Leffler type fractional differential equations with coupled integral boundary conditions,” *J. Math. Tech. Model.*, vol. 1, no. 2, pp. 16–28, 2024.

BİTLİS EREN UNIVERSITY
JOURNAL OF SCIENCE AND TECHNOLOGY

E-ISSN: 2146-7706

OPTIMIZATION STUDY OF FUEL BLENDS IN AN SI ENGINE RUNNING WITH GASOLINE/ISOPROPANOL/ISOAMYL ALCOHOL BLENDS

Doğan Şimşek [1], Yusuf Karabacak [2], Niyazi Yılmaz Çolak [3,*], Bahri Aksu [4]

[1] *National Defence University, Department of Mechanical Engineering, Türkiye, dogan.simsek@msu.edu.tr*
[2] *National Defence University, Department of Mechatronics Technology, Türkiye, yusuf.karabacak@msu.edu.tr*
[3] *Bitlis Eren University, Department of Motor Vehicles and Transportation Technologies, Türkiye, nycolak@beu.edu.tr*
[3] *Balikesir University, Department of Electrical and Energy Technologies, Türkiye, bahri.aksu@balikesir.edu.tr*
* *Corresponding author*
[4] *Balıkesir University, Vocational School, Türkiye, bahri.aksu@balikesir.edu.tr*

KEYWORDS
RSM
Gasoline alcohol blends
Propanol
Isoamyl
Emissions
Optimization

ARTICLE INFO
Research Article
Doi
10.17678/beuscitech.1500673

Received	June 13, 2024
Revised	April 29, 2025
Accepted	May 26, 2025
Year	2025
Volume	15
Issue	1
Pages	37-55

ABSTRACT

In this study, was focused on determining the optimum alcohol mixtures of gasoline iso-propanol and isoamyl alcohol mixtures according to minimum exhaust emission and BSFC (Brake Specific Fuel Consumption) and maximum CGP (Cylinder Gas Pressure) parameters. In the optimization study, 3 different iso-propanol (vol. 10, 20 and 30) and 3 different iso-amyl (vol. 5, 10 and 20) rate were used as input parameters at maximum power and torque speed. The experimental study, it was performed in a single-cylinder air-cooled, spark-ignition engine (SI), at full throttle position, maximum power speed (3600 min^{-1}) and maximum torque speed (2400 min^{-1}). In the optimization study, ANOVA supported RSM (Response Surface Methodology) and CCD (Central Composite Design) were used as the experimental design. In the results obtained, it was determined as an effective parameter for BSFC of engine speed, and for CGP were effective also alcohol types along with engine speed. As a result of the optimization, as the optimum operating parameters were determined as 3600 min^{-1} engine speed, 27.7778% iso-propanol and 13.9394% iso-amyl alcohol. In the confirmation tests, the error rates were obtained as 3.36%, 3.45%, 9.81%, 4.76% and 4.67% for BSFC, CGP, HC, CO and NO_X, respectively.

1 INTRODUCTION

Exhaust emissions from road vehicles are one of the leading causes of air pollution in both developing and developed countries. Emissions from road vehicles account for approximately 50% of total pollution [1,2]. Incomplete combustion of gasoline in ICE (Internal Combustion Engine) increases CO and HC emission levels. However, at high operating temperatures, excess oxygen causes NOX emissions to increase [3]. The catalytic converter used in the exhaust system reduces the pollution rate. However, these systems used cause an increase in fuel consumption by about 15% [4]. For this reason, in many studies, it is seen that researchers are trying to exploration cleaner alternative fuels [5-7]. In these exploration efforts, biofuels have been a serious research topic. Alcohol-based fuels are accepted as one of the renewable solutions with almost zero CO_2 potential through efficiently conversion of biomass [8]. The higher-octane number, higher oxygen content and single boiling point of alcohols make it possible to use them in spark ignition engines. Besides, as an additive, alcohols can be a good solution to improve fuel properties. Due to the high research octane number (RON) and engine octane number (MON), the octane number increases rapidly when oxygenated fuels are mixed with gasoline [9-10]. Mourad and Mahmoud [11] investigated the performance and exhaust emissions of a spark ignition engine using gasoline-propanol fuel mixtures. In their results, they reported that fuel economy increased by approximately 2.84%, and there was an improvement over 10% in exhaust emissions, especially in HC and CO emissions. Similarly, Kaisan et al.,[12] stated in their study that as the alcohol percentage in gasoline-propanol-camphor mixtures increased, engine performance increased and exhaust emissions decreased. In addition, Uslu and Celik [13] investigated the effect on performance and exhaust emissions of engine of isoamyl alcohol addition at 3 different rates (10%, 20% and 30%) to gasoline. In their results, they stated that there were significant improvements in the exhaust emissions of the fuel mixture with 30% isoamyl alcohol added, compared to the use of gasoline at all compression ratios. In the engine performance, they stated that with the increase of the compression ratio, the engine torque and power increased with the fuel mixture added with 20% isoamyl alcohol.

In order to improve the performance and emission characteristics of internal combustion engines, different optimization methods have been used to optimize operating conditions such as ignition timing, injection timing, speed, load, compression ratio, air-fuel ratio, especially with alternative fuel [14-17]. In general, the technical approach of the studies done in the literature is to use the optimized mixture in a spark ignition engine without modification as well as increase performance and reduce emissions. Response Surface Methodology (RSM) is a good method for performing this experimental design. RSM is a widely used technique to solve many industrial problems. It is one of the practical and economical solutions to evaluate single and combined factors of experimental variables [18]. The main advantage of the method requires less testing, and less time is spent compared to a real experimental study. This approach is widely used and has been applied in much research. Uslu and Celik [17] experimentally investigated the effects engine performance and emissions of use isoamyl alcohol/gasoline fuel mixture in a spark ignition engine (SI). In addition, the obtained results were estimated with Artificial Neural Network (ANN) and optimized with Response Surface Methodology (RSM). In the RSM results, they stated that 15% isoamyl alcohol ratio at 8.31 CR (Compression Ratio) and 2957.58 rpm engine speed are the optimum engine operating parameters. In their results, they reported that the RSM supported ANN model is an effective method for estimating and optimizing engine outputs with minimum testing. In a study by Adebili et al., [20] were used RSM for the optimization of gasoline/fuseoil mixtures. In the optimization results, they founded that as 47.21% engine load and 25% fuse oil of the optimum operating parameters. They stated that the confirmation tests were performed successfully, and all the results were significant at the 5% level. However, a high desirability value of 0.63 for the regression model reported that RSM could be used efficiently for modelling and optimization of engine operating parameters. When the studies in the literature examined, it is seen that the effects of gasoline/propanol and gasoline/isoamyl alcohol mixtures on engine performance and exhaust emissions were examined. However, there are not many studies on triple fuel mixtures such as gasoline/propanol/isoamyl. Also, the ability to optimize the input-response factors of gasoline/isopropanol/isoamyl alcohol fuel blends in SI engines with a statistical approach (RSM) has not yet been investigated. This study is focused to the optimization of input parameters based on the response factors of fuel mixtures comprising gasoline, isopropanol, and isoamyl alcohol for use in a gasoline engine. The aim of this research is to address and contribute to the existing gap in the literature on this subject.

2 MATERIALS AND METHOD

2.1 Test Fuel

In the study, iso-propanol was added to the gasoline at 3 different rates (10%, 20% and 30% vol.). Different fuel combinations were created by adding alcohol in 3 different ratios (5%, 10% and 20% vol.) to this prepared gasoline/iso-propanol fuel mixture. Fuel properties of gasoline and alcohols used in the study were given in Table 1.

Table 1. *Properties of Fuels.*

Properties	Gasoline	Iso-propanol	Iso-amyl
Chemical Formula	C_8H_{18}	C_3H_8O	$C_5H_{12}O$
Molecular weight (kg/kmol)	114.18	60.10	88.1
Lower Heating Value (Mj/kg)	44.0	32.940	35.370
Stoichiometric air/fuel ratio	14.6	10.28	11.76
Heat of evaporation (kj/kg)	225	761	621
Research octane number	95	112.5	113
Engine octane number	85	---	84
Density	720-775	785	801.4

2.2 Experimental Procedure

In the experiments was used Single-cylinder, spark-ignition, air-cooled (ATIMAX AG 210 E) engine. Before starting the tests, the carburetor was adjusted using the exhaust emission data specified in the catalogue values. In all test conditions, the excess air coefficient was adjusted (HFK - λ=1) using a conical-tipped adjusting screw. The adjustment process was repeated for all fuel types used. Experiments were started when the engine reaches operating temperature. Measurements were made at maximum torque and power speeds in the experiments. In-cylinder pressure measurement was made with the help of Piezoresistive high pressure sensor and oscilloscope. The technical features of the engine used in the experiments are given in Table 2. The engine performance test stand is shown schematically in Figure 1. In the test system, an electric dynamometer is used with

26 kW power, 80 Nm torque and a speed of max 5000 rpm. In the test system, fuel consumption, engine torque and engine power data were instantly recorded digitally with the interface program used.

Table 2. *Features of the test engine*.

Model	Atimax 210 E
Engine Type	Four Stroke, Single Cylinder
Engine Volume (cm^3)	196
Compression Ratio	8.5/1
Maximum Speed (rpm)	4200
Ignition System Type	Transistorized Coil
Fuel System	Carburetor
Cooling System	Air Cooled

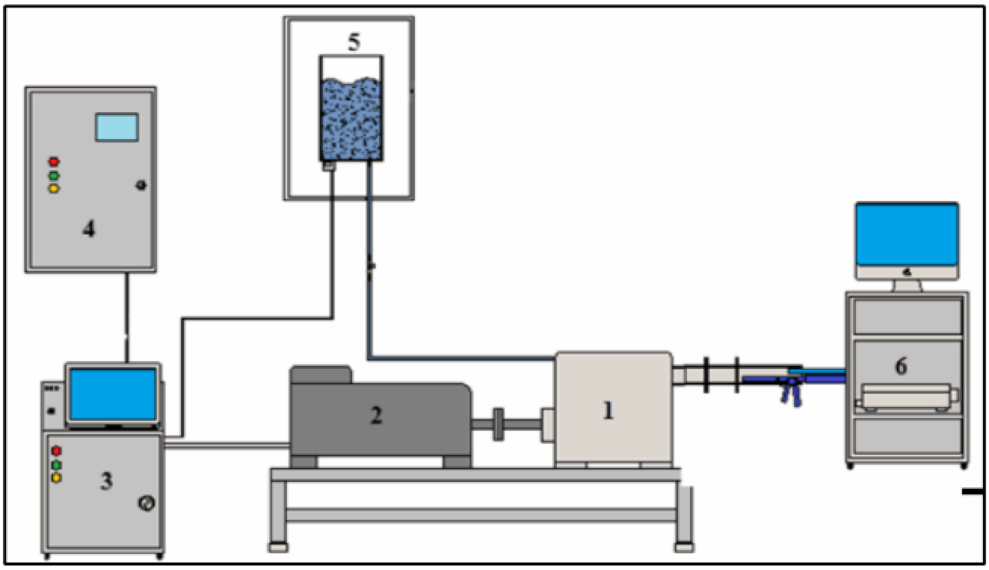

Figure 1. *Engine test setup*.

Emission measurements were measured at specified (max torque and max power) engine speeds. Mobydic-5000 gas analyzer was used for emission measurements. The technical features of the emission device used were given in Table 3.

Table 3. *Features of the exhaust gas analyser*.

MOBYDIC 5000 GAS ANALYSIS DEVICE	
CO % Vol.	0 - 10
CO_2 % Vol.	0 - 20
HC ppm	0 - 20000
O_2 % Vol.	0 - 21
NO_X ppm	0 - 5000
Lambda	- 5

2.3 Response Surface Methodology

Response Surface Methodology (RSM), which has achieved successful results in applications in many different fields, is a computer-based application. This application is widely used for modelling and optimization of the performance and emissions of internal combustion engines [21-23]. RSM establishes a relationship between input and output parameters. It optimizes the responses according to the input factors, according to the relationship between the input and output parameters. For this purpose, RSM uses the least squares technique. According to the RSM, each of the motor input parameters is assumed to be computable and can be expressed by the following equation: [23]

$$y = f(X_1, X_2, \ldots, X_n) \quad \textbf{(1)}$$

Here; X_1, $X_2 \ldots . X_n$ the input parameters, respectively, and y is the output parameter. The first step in RSM consists of the field or independent variables of the process and empirical statistical modelling in order to develop empirical relationships for estimation and optimization, and to develop an appropriate approximation relationship between response and process variables. A quadratic equation model is applied for this relationship as shown below.

$$y = \beta_0 + \sum_{i=1}^{k} \beta_i x_i + \sum_{i=1}^{k} \sum_{j\geq 1}^{k} \beta_{ij} x_i x_j + \sum_{i=1}^{k} \beta_{ii} x_i^2 + \varepsilon \quad \textbf{(2)}$$

Here, i is the linear coefficient, j is the quadratic coefficient, β is the regression coefficient, k is the number of parameters, and ε is the error discovered in the response. In this study, Central Composite Design (CCD), which gives relatively more precise results compared to other experimental designs, has been applied. Input variables were selected as engine speed (ES), Fuel type 1 (Iso-propanol) and Fuel type 2 (Iso-amyl alcohol). Input variables and levels were given in Table 4. As the output parameters of the model, Brake Specific Fuel Consumption (BSFC), Cylinder Gas Pressure (CGP), Hydrocarbon (HC), Carbon Monoxide (CO) and Nitrogen Oxide (NOX) were selected. The independent variables related to the experimental study were given in Table 5.

Table 4. *Input parameters.*

Input Factor	Code	Levels		
Engine Speed min^{-1}	X_1	2400	3600	-
Iso-propanol (%)	X_2	10	20	30
Iso-amyl (%)	X_3	5	10	20

Table 5. *The independent variables related to the experimental study.*

Run Order	Engine Load	Iso-Propanol	Iso-amyl	BSFC (g/kWh)	CGP (bar)	HC (ppm)	CO (%)	NO_X (ppm)
1	2400	1	5	183.0341	29.80	38	2.75	1598
2	2400	10	10	180.0341	31.60	32	2.38	1756
3	2400	10	20	185.8102	28.70	35	2.12	1328
4	3600	10	5	146.5268	26.40	31	2.29	1892
5	3600	10	10	142.5685	28.60	25	1.84	2068
6	3600	10	20	144.0366	25.00	28	1.57	1696
7	2400	20	5	170.6845	30.70	36	1.91	1762
8	2400	20	10	167.2685	32.90	28	1.52	1863
9	2400	20	20	171.6385	29.10	33	1.32	1457
10	3600	20	5	132.6249	27.80	27	1.28	2035
11	3600	20	10	129.2836	29.30	20	1.08	2082
12	3600	20	20	143.9541	26.50	24	0.92	1949
13	2400	30	5	187.6215	30.40	31	2.29	1429
14	2400	30	10	184.0137	31.40	27	1.84	1598
15	2400	30	20	184.9688	29.20	32	1.57	1226
16	3600	30	5	149.3599	27.10	39	1.95	1321
17	3600	30	10	148.7166	29.10	32	1.53	1458
18	3600	30	20	150.0249	27.30	35	1.39	1272

3 RESULTS AND DISCUSSION

3.1 RSM Results

Analysis of variance (ANOVA) results for BSFC and CGP are given in Table 6, analysis of variance (ANOVA) results for HC CO and NO_X were given in Table 7.

Table 6. *Analysis of Variance for BSFC and CGP.*

		BSFC			CGP		
	DF	Sum of Sequare	F-valuare	p-valuare	Sum of Sequare	F-valuare	p-valuare
Model	8	6774.69	82.66	0.000	69.0281	52.66	0.000
Linear	3	5869.79	190.98	0.000	43.4818	88.46	0.000
(X_1) Engine Speed	1	5820.14	568.10	0.000	38.2571	233.49	0.000
(X_2) Iso-Propanol	1	40.32	3.94	0.079	1.8113	11.05	0.009
(X_3) Iso-amyl	1	9.33	0.91	0.365	3.4133	20.83	0.001
Square	2	723.83	35.33	0.000	19.4236	59.27	0.000
X_2^2	1	674.33	65.82	0.000	1.7778	10.85	0.009
X_3^2	1	49.50	4.83	0.056	17.6458	107.69	0.000
2-Way Interaction	3	11.92	0.39	0.765	1.1509	2.34	0.141
X_1xX_2	1	4.37	0.43	0.530	0.5633	3.44	0.097
X_1xX_3	1	6.37	0.62	0.451	0.1575	0.96	0.352
X_2xX_3	1	1.18	0.12	0.742	0.4301	2.62	0.140
Error	9	92.20			1.4747		
Total	17	6866.89			70.5028		

Table 7. *Analysis of Variance for HC CO and NOX.*

		HC			CO			NO_X		
	DF	Sum of Sequare	F-valuare	p-valuare	Sum of Sequare	F-valuare	p-valuare	Sum of Sequare	F-valuare	p-valuare
Model	8	363.627	6.02	0.007	3.98756	89.05	0.000	1333169	25.80	0.000
Linear	3	78.624	3.47	0.064	2.31498	137.87	0.000	612708	31.62	0.000
(X_1) Engine speed	1	55.269	7.32	0.024	0.78874	140.92	0.000	184438	28.56	0.000
(X_2) Iso-Prop.	1	4.605	0.61	0.455	0.4582	81.86	0.000	325780	50.44	0.000
(X_3) Iso-amyl	1	18.750	2.48	0.150	1.06803	190.82	0.000	102490	15.87	0.003
Square	2	183.373	12.14	0.003	1.67240	149.40	0.000	514473	39.83	0.000
X_2^2	1	66.694	8.83	0.016	1.54588	276.19	0.000	370881	57.42	0.000
X_2^2	1	116.679	15.15	0.003	0.12652	22.60	0.001	143592	22.23	0.001
2-Way Interaction	3	117.349	5.18	0.024	0.05149	3.07	0.084	143471	7.40	0.008
X_1xX_2	1	114.083	15.10	0.004	0.04320	7.72	0.021	115248	17.84	0.002
X_1xX_3	1	2.099	0.28	0.611	0.00734	1.31	0.282	21047	3.26	0.105
X_2xX_3	1	1.167	0.15	0.703	0.00095	0.17	0.690	7176	1.11	0.319
Error	9	67.984			0.05037			58131		
Total	17	431.611			4.03796			1391300		

Analysis of variance (ANOVA) provides numerical information for the probability value [24]. In this study, ANOVA was used to verify the stability of the models [25]. The “p” value is an important parameter in ANOVA results. For the “p” value, 0.05 is accepted as the reference limit. "p" value greater than 0.05 indicates that the model is unimportant. If the “p” value is less than 0.05, it means that the factor has a high effect on the model being developed [8]. When the linear coefficients obtained for BSFC in Table 6 are examined, the “p” value of the engine speed is less than 0.05 and it is greater than 0.05 for alcohol types. In terms of second order coefficients, the “p” value for the percent iso-propanol is less than 0.05, and the “p” value for the engine speed and percent isoamyl alcohol is greater than 0.05. This indicates that engine speed has a greater influence on BSFC optimization. Considering the linear and second order coefficients obtained for CGP, the “p” value of the percentage of motor speed and alcohol species in linear coefficients is less than 0.05. Additionally, all “p” values for second order coefficients are greater than 0.05. The alcohol types used together with the engine speed are also effective parameters for CGP. Similarly, in Table 7, in the ANOVA results for HC CO and NO_X emission results, the “p” value for linear and square coefficients is less than 0.05, except for HC emission. However, in all emission results, p values for the parameters are greater than 0.05 except for the factor X_1xX_2 for the second order coefficients. It is understood that the model is important for the CO and NO_X results. Regression statistical fit (evaluation of the model) is given in Table 8. When the values obtained in the 5% and 95.82%, respectively. It is understood from the obtained results that the developed model is compatible table are examined, BSFC, CGP, HC, CO and NO_X were obtained as 98.66%, 97.91%, 84.25%, 98.7. The R^2 value is an indicator of how well the statistical model developed with the experimental data is matched. If the R^2 value was '0', the obtained correlation line does not fit, and the R^2 value was '1' means perfect fit [26]. The adjusted version of R^2 indicates the fit of the predictors to the conventional estimate. The Predictors R^2 indicates how well a regression model predicts responses from new observations. The Adj. R^2 and Pred. R^2 values given in Table 8, it is shows that the values for BSFC, CGP, CO and NOX are in acceptable agreement. The highest difference between these values is about 9%. In a study by Shameer and Ramesh [27], Adj. R^2 and Pred. R^2 values difference are less than 20% and therefore these values are in reasonable agreement. However, in all these results, it cannot be said that the values for HC are compatible. In HC result Adj. R^2 and Pred. R^2 between difference is about 45%.

Table 8. *Assessment of Model.*

Model	BSFC	CGP	HC	CO	NO_X
R^2 (%)	98.66	97.91	84.25	98.75	95.82
Adj. R^2 (%)	97.46	96.05	70.25	97.64	92.11
Pred. R^2 (%)	93.45	90.13	38.84	94.49	84.02

The second-order regression equations generated by RSM to estimate the output parameters based on the input parameters are given in Equations 3-7 respectively.

$$\begin{aligned} BSFC &= 309.2 - 0.03423\,ES - 5.248\,IPA - 2.05\,IAA + 0.1298\,IPA*IPA \\ &+ 0.0716\,IAA*IAA + 0.000101\,ES*IPA + 0.000159\,ES*IAA \\ &- 0.0050\,IPA*IAA \end{aligned} \quad \textbf{(3)}$$

$$\begin{aligned} CGP &= 32.99 - 0.003486\,ES + 0.160\,IPA \\ &+ 0.863\,IAA - 0.00667\,IPA*IPA - 0.04278\,IAA*IAA + 0.000036\,ES*IPA \\ &+ 0.000025\,ES*IAA + 0.00304\,IPA*IAA \end{aligned} \quad \textbf{(4)}$$

$$\begin{aligned} HC &= 95.4 - 0.01208\,ES - 3.175\,IPA - 2.743\,IAA \\ &+ 0.0408\,IPA*IPA + 0.1100\,IAA*IAA \\ &+ 0.000514\,ES*IPA - 0.000091\,ES*IAA + 0.0050\,IP*IAA \end{aligned} \quad \textbf{(5)}$$

$$\begin{aligned} CO &= 7.000 - 0.000619\,ES - 0.3002\,IPA - 0.1494\,IAA \\ &+ 0.006217\,IPA*IPA + 0.003622\,IAA*IAA + 0.000010\,ES*IP \\ &+ 0.000005\,ES*IA + 0.000143\,IP*IA \end{aligned} \quad \textbf{(6)}$$

$$\begin{aligned} NO_X &= -384 + 0.383\,ES + 149.3\,IPA \\ &+ 48.9\,IAA - 3.045\,IPA*IPA - 3.859\,IAA*IAA - 0.01633\,ES*IPA \\ &+ 0.00914\,ES*IAA + 0.392\,IPA*IAA \end{aligned} \quad \textbf{(7)}$$

Here, ES, IPA and IAA are engine speed, Iso-propanol and Iso-amyl alcohol, respectively.

3.2 Brake Specific Fuel Consumption

In the Figure 2 given common impact of engine speed, Iso-propanol ratio and Iso-amyl ratio on BSFC.

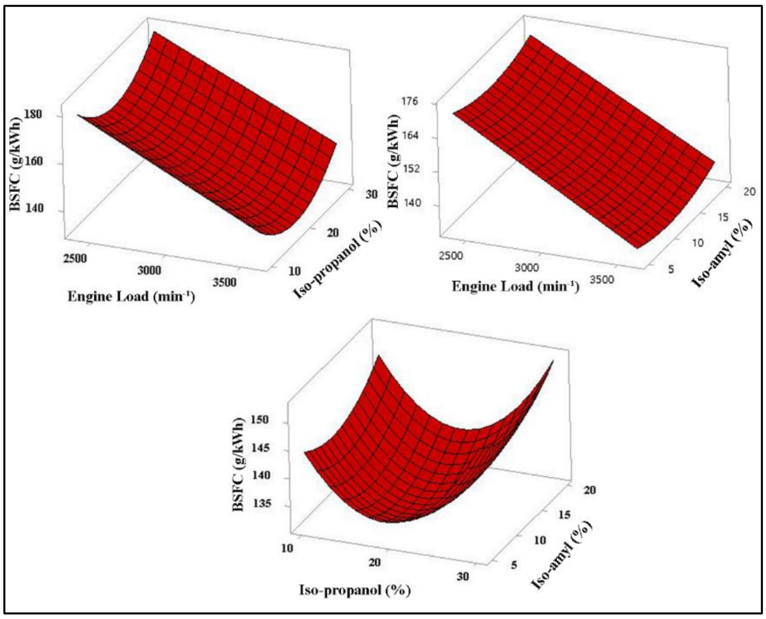

***Figure 2**. Common impact of engine speed, Iso-propanol ratio and Iso-amyl ratio on BSFC.*

When the graph of the joint effect of engine speed, iso-propanol ratio and iso-amyl ratio on BSFC given in Figure 2 is examined, it is understood that BSFC is lower at maximum power speed compared to maximum torque speed. The results obtained were expected. BSFC is the ratio of the fuel consumption rate to the effective power generated from the engine. In other words, it is an indicator of how much of the fuel consumed by the engine is converted into useful work [6]. Similarly, in the same graphs, it is seen that BSFC decreases to a certain extent at all engine speeds with increasing alcohol content in the fuel and increases again with increasing alcohol content. The decrease in BSFC with a certain percentage of alcohol in the fuel can be explained by the combustion efficiency. The oxygen content in the structure of alcohols supports combustion in the cylinder. Both the oxygen content and the high flame speed of alcohols allow unburned hydrocarbons that cannot enter the combustion reaction to react. This improves the combustion efficiency [28]. An increase in combustion efficiency leads to a decrease in BSFC. The BSFC increases again with increasing alcohol content, which can be attributed both to a further decrease in the lower heating value of the blend fuel and to the lower stoichiometric air-fuel ratio of the alcohols. In order to maintain the same engine power, it is necessary to achieve the required stoichiometric value. To achieve this, more fuel must be injected into the cylinder. This leads to an increase in BSFC [29].

3.3 Cylinder Gas Pressure

In the Figure 3 given common impact of engine speed, iso-propanol ratio and iso-amyl ratio on CGP.

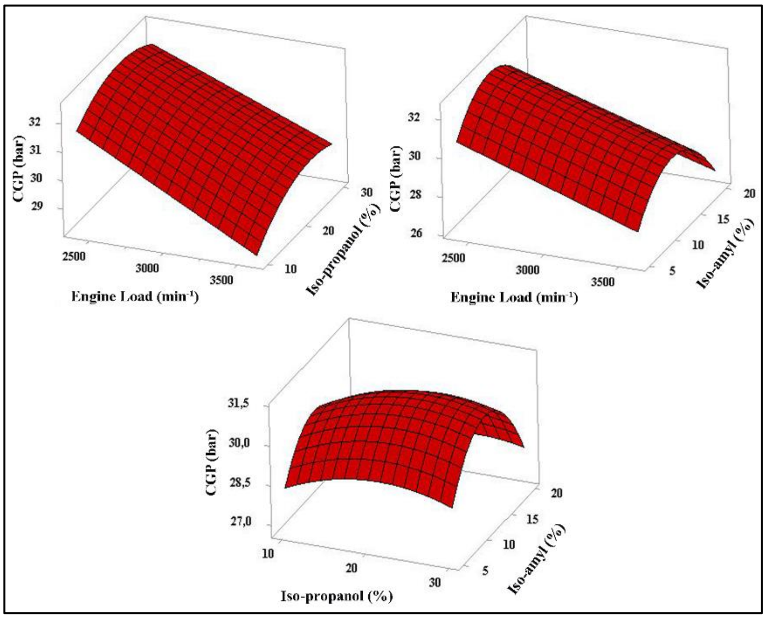

***Figure 3**. Common impact of engine speed, Isopropanol ratio and Isoamyl ratio on CGP.*

When the joint effect of engine speed, iso-propanol ratio and iso-amyl ratio on CGP given in Figure 3 is analyzed, it is seen that CGP decreases with increasing engine speed for both alcohol types. However, CGP increase are show with increasing iso-propanol alcohol in gasoline. Similarly, with the use of iso-amyl alcohol, CGP increases up to a certain rate, while CGP decreases after a certain rate. Increasing alcohol content in the fuel increases the combustion efficiency (due to oxygen content), which leads to an increase in in-cylinder pressure [30]. Masum et al., [31] reported in similarly a study that the peak in-cylinder pressure was higher with P20 (Gasoline + 20% propanol) fuel because P20 has a higher RON and therefore P20 starts heat release earlier than other fuels. However, it is seen that the increased alcohol content in gasoline causes the CGP to decrease again. The high latent heat of vaporization of alcohols increases the charge cooling effect resulting in lower in-cylinder temperature [5]. Due to the charge cooling effect, the end of combustion temperature and pressure are also reduced.

3.4 Exhaust Emissions

In the Figure 4 given common impact of engine speed, iso-propanol ratio and iso-amyl ratio on HC emission.

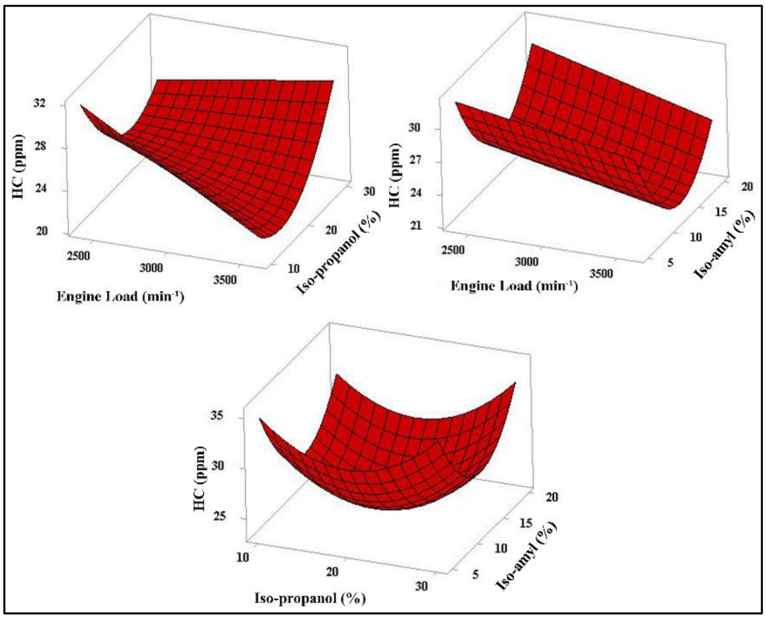

***Figure 4**. Common impact of engine speed, iso-propanol ratio and iso-amyl ratio on HC emission.*

When the joint effects of engine speed, iso-propanol and iso-amyl ratios on HC emissions given in Figure 4 are analyzed, it is seen that HC emissions decrease with increasing engine speed. It is understood that HC emissions decrease with increasing iso-propanol ratio in gasoline fuel and increase again after a certain ratio. HC emissions are seen as at lower levels with decreasing iso-propanol ratio at max power speed compared to max torque speed. The fact that iso-propanol alcohol has a high heat of vaporization negatively affects the combustion efficiency at high engine speeds. In addition, the turbulence of the air taken into the cylinder at high engine speeds has a cooling effect on the cylinder walls and therefore causes an increase in unburned HC emissions [32]. In the Figure 5 given common impact of engine speed, iso-propanol ratio and iso-amyl ratio on CO emission.

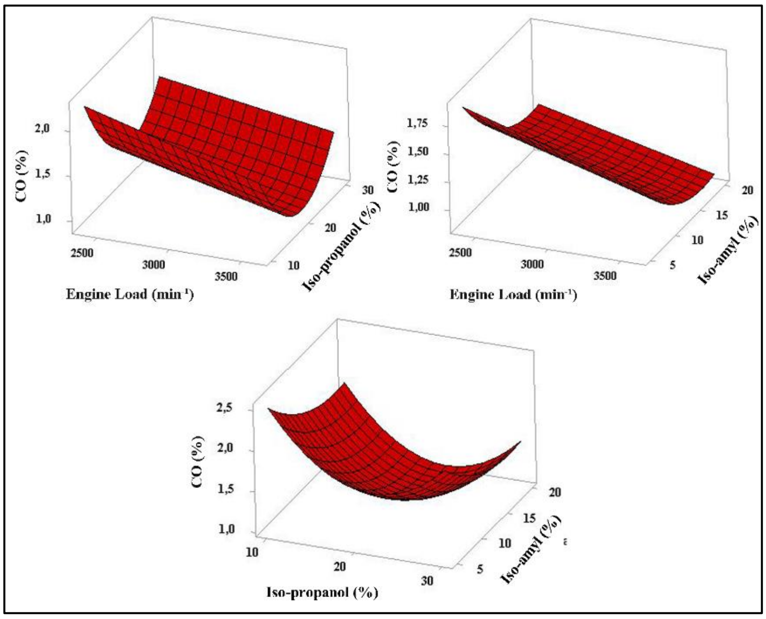

***Figure 5**. Common impact of engine speed, iso-propanol ratio and iso-amyl ratio on CO emission.*

When the joint effects of engine speed, iso-propanol and iso-amyl ratios on CO emissions given in Figure 5 are analyzed, it is seen that CO emissions decrease with increasing engine speed. However, it is seen that CO emissions decrease with the increase of iso-propanol and iso-amyl alcohol ratios up to a certain level at all engine speeds. With further increase in the alcohol ratio, CO emissions increase again. CO emission is a toxic gas resulting from incomplete combustion. The oxygen contained in the structure of alcohols improves the combustion efficiency of the fuel. Therefore, CO emission decreases [33]. In the Figure 6 given common impact of engine speed, iso-propanol ratio and iso-amyl ratio on NO_X emission.

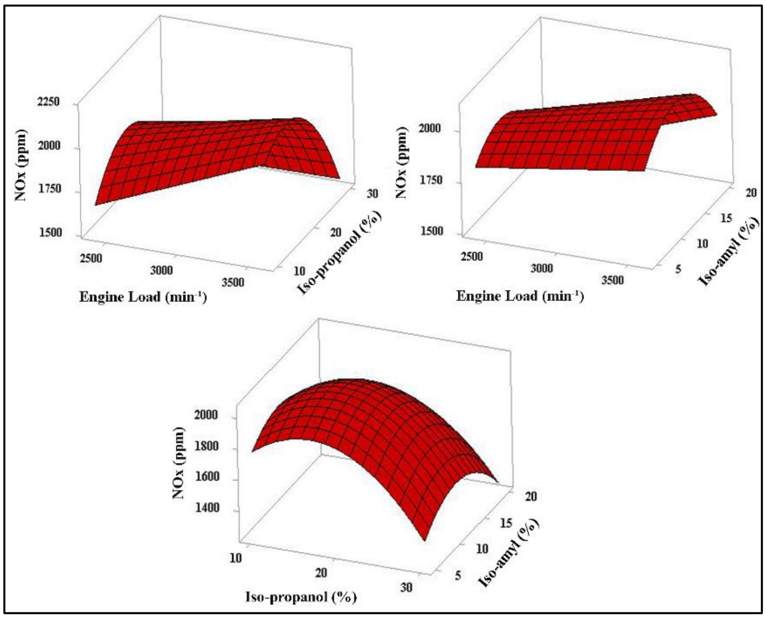

***Figure 6**. Common impact of engine speed, iso-propanol ratio and iso-amyl ratio on NOX emission.*

When the joint effects of engine speed, iso-propanol and iso-amyl alcohol ratios on NO_X emissions given in Figure 6 are analyzed, it is seen that NO_X emissions increase with increasing engine speed. This increase in NO_X emissions can be explained by the increase in combustion efficiency in the cylinder. It is known that NO_X emission formation depends on in-cylinder temperature and pressure. The use of alcohols with high oxygen content causes higher NO_X emissions due to higher in-cylinder pressure and temperature [34,35]. It is seen that NO_X emissions decrease after a certain ratio in both alcohol ratios increasing in gasoline. This decrease in NO_X emissions is due to the high evaporation temperature of alcohols. The high evaporation temperature of the alcohols used causes a cooling effect in the cylinder. This cooling effect causes NO_X emissions to decrease [36].

3.5 Optimization Results

The optimization results of different alcohol and gasoline blended fuels are given in Figure 7.

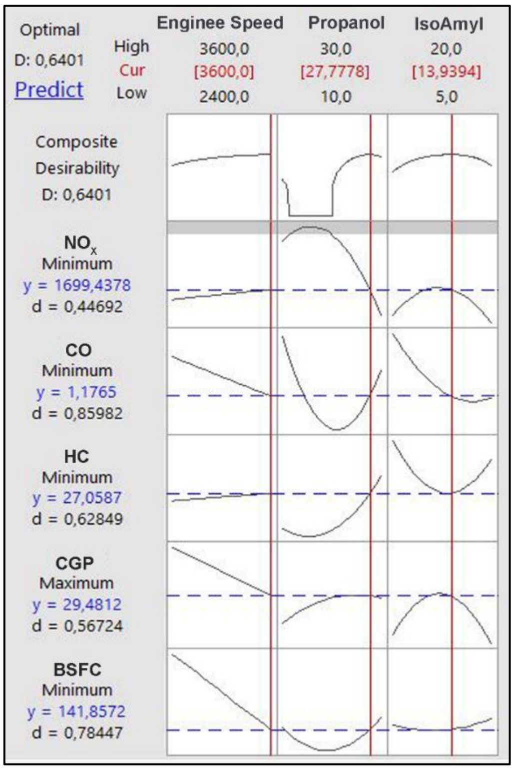

***Figure 7**. Optimization results of alcohol ratios of different alcohol-gasoline blends.*

In this study, an RSM optimization was performed to determine the ratios of iso-propanol and iso-amyl alcohol added to gasoline in a way to maximize CGP while minimizing BSFC and all emissions. The results obtained in the optimization with a desirability value of 0.6401 were 27.7778% iso-propanol, 13.9394% iso-amyl and 3600 min-1 engine speed as shown in Figure 6. In addition, while 29.4812 bar CGP was obtained at optimum engine speed and alcohol ratios, BSFC, HC, CO and NOX results were obtained as 141.857 g/kWh, 27.0587 ppm, 1.1765% and 1699.4378 ppm, respectively. In order to evaluate the optimization results, a verification study was carried out and the results obtained are given in Table 9 comparatively.

***Table 9**. Validation test for predicted and actual values.*

Engine Speed	Iso-propanol	Iso-amyl	Value	BSFC	CGP	HC	CO	NO_X
			Predicted	141.8572	29.4812	25.0587	1.176	1699.4371
3600	27	14	Experimental	146.635	30.50	22.6	1.12	1620
			Error (%)	3.36	3.45	9.81	4.76	4.67

The validation test was based on the optimization results. When the results given in Table 9 are examined, it is seen that BSFC, CGP, CO, NOX results can be evaluated with less than 5% error rate. For HC emissions, this error rate is approximately 10%.

4 CONCLUSIONS

In the present presented study, RSM with ANOVA was applied to determine the optimum iso-propanol and iso-amyl alcohol ratios and engine speed in an SI engine operating with a gasoline alcohol blend to simultaneously find maximum CGP, minimum BSFC, HC, CO and NO_X. The results obtained in the study are given below.

As a result of optimization, engine speed was obtained as 3600 min-1, iso-propanol ratio was 27.7778% and iso-amyl ratio was 13.9394%.

CGP 29.4812 bar, BSFC 141.8572 g/kWh, HC 25.0587 ppm, CO 1.176% and NO_X 1699.4371 ppm were obtained corresponding to the optimum engine speed and alcohol ratios.

R^2 values for BSFC, CGP, HC, CO, NO_X were obtained as 98.66, 97.91, 84.25, 98.75 and 95.82, respectively. The R^2 values were found to be at acceptable levels for BSFC, CGP, CO, NO_X responses.

The validation test showed good agreement between the optimization results and the experimental results for BSFC, CGP, CO and NO_X with less than 5% error rate. For the HC emission result, it showed that there is less than 10% error rate between the optimization and experimental results. It is thought that the high error rate in HC emissions is due to factors such as measurement error and measurement accuracy.

REFERENCES

[1] L. A. Raman, B. Deepanraj, S. Rajakumar, and V. Sivasubramanian, "Experimental investigation on performance, combustion and emission analysis of a direct injection diesel engine fuelled with rapeseed oil biodiesel," *Fuel (Lond.)*, vol. 246, pp. 69-74, 2019.

[2] D. B. Sivakumar, M. Arulmozhi, S. Sathyanarayanan, and M. Sridharan, "Optimization of gasoline engine operating parameters fueled with DIPE-gasoline blend: Comparative evaluation between response surface methodology and fuzzy logic expert system," *Process Saf. Environ. Prot.*, vol. 158, pp. 291-307, 2022.

[3] E. Goh et al., "Prediction of minimum achievable NO levels for fuel-staged combustors," *Combust. Flame*, vol. 200, pp. 276-285, 2019.

[4] Y. S. H. Najjar, “Alternative Fuels for Spark Ignition Engines,” *Open Fuels Energy Sci. J.*, vol. 2, no. 1, pp. 1–9, 2009.

[5] Y. Qian, J. Guo, Y. Zhang, W. Tao, and X. Lu, “Combustion and emission behavior of N-propanol as partially alternative fuel in a direct injection spark ignition engine,” *Appl. Therm. Eng.*, vol. 144, pp. 126–136, 2018.

[6] D. Şimşek, F. Oral, and N. Y. Çolak, “The effect on engine performance and emissions of gasoline-propanol-hexane fuel blends on single cylinder spark-ignition engines,” *Journal of Thermal Sciences and Technology*, vol. 39, pp. 81–89, 2019.

[7] M. Ghanbari, L. Vanani, and G. Najafi, “Investigating the effect of gasoline fuel filter lifetime on fuel pressure and ignition advance using the RSM method,” *Fluid Mechanics & Aerodynamics Journal*, vol. 9, pp. 135–150, 2020.

[8] O. I. Awad et al., “Response surface methodology (RSM) based multi-objective optimization of fusel oil -gasoline blends at different water content in SI engine,” *Energy Convers. Manag.*, vol. 150, pp. 222–241, 2017.

[9] I. M. Yusri, R. Mamat, W. H. Azmi, G. Najafi, N. A. C. Sidik, and O. I. Awad, “Experimental investigation of combustion, emissions and thermal balance of secondary butyl alcohol-gasoline blends in a spark ignition engine,” *Energy Convers. Manag.*, vol. 123, pp. 1–14, 2016.

[10] Z. Zhang, T. Wang, M. Jia, Q. Wei, X. Meng, and G. Shu, “Combustion and particle number emissions of a direct injection spark ignition engine operating on ethanol/gasoline and n-butanol/gasoline blends with exhaust gas recirculation,” *Fuel (Lond.)*, vol. 130, pp. 177–188, 2014.

[11] M. Mourad and K. R. M. Mahmoud, “Performance investigation of passenger vehicle fueled by propanol/gasoline blend according to a city driving cycle,” *Energy (Oxf.)*, vol. 149, pp. 741-749, 2018.

[12] M.U. Kaisan, L.O. Yusuf, I.U. Ibrahim, S. Abubakar, S. Narayan, Effects of propanol and camphor blended with gasoline fuel on the performance and emissions of a spark ignition engine, *ACS Omega*. 5 (2020) 26454–26462.

[13] S. Uslu and M. B. Celik, “Combustion and emission characteristics of isoamyl alcohol-gasoline blends in spark ignition engine,” *Fuel (Lond.)*, vol. 262, no. 116496, p. 116496, 2020.

[14] A. Atmanlı, B. Yüksel, E. İleri, and A. Deniz Karaoglan, “Response surface methodology based optimization of diesel-n-butanol –cotton oil ternary blend ratios to improve engine performance and exhaust emission characteristics,” *Energy Convers. Manag.*, vol. 90, pp. 383-394, 2015.

[15] J. Li, C. Guo, W. B. Wang, and Z. J. Wu, “Optimal Mixture Ratios of Biodiesel Ethanol Diesel for Diesel Engines,” *Energy Power Eng.*, vol. 03, no. 05, pp. 625–629, 2011.

[16] G. Khoobbakht, G. Najafi, M. Karimi, and A. Akram, “Optimization of operating factors and blended levels of diesel, biodiesel and ethanol fuels to minimize exhaust emissions of diesel engine using response surface methodology,” *Appl. Therm. Eng.*, vol. 99, pp. 1006–1017, 2016.

[17] S. Uslu and M. B. Celik, “Performance and exhaust emission prediction of a SI engine fueled with I-amyl alcohol-gasoline blends: An ANN coupled RSM based optimization,” *Fuel (Lond.)*, vol. 265, no. 116922, p. 116922, 2020.

[18] A. Asghar, A. A. Abdul Raman, and W. M. A. W. Daud, “A comparison of central composite design and Taguchi method for optimizing Fenton process,” *ScientificWorldJournal*, vol. 2014, p. 869120, 2014.

[19] L. Ma, Y. Han, K. Sun, J. Lu, and J. Ding, “Optimization of acidified oil esterification catalyzed by sulfonated cation exchange resin using response surface methodology,” *Energy Convers. Manag.*, vol. 98, pp. 46–53, 2015.

[20] S. M. Safieddin Ardebili, H. Solmaz, and M. Mostafaei, “Optimization of fusel oil – Gasoline blend ratio to enhance the performance and reduce emissions,” *Appl. Therm. Eng.*, vol. 148, pp. 1334–1345, 2019.

[21] E. Ileri, A.D. Karaoglan, A. Atmanli, Response surface methodology based prediction of engine performance and exhaust emissions of a diesel engine fuelled with canola oil methyl ester, *J. Renew. Sustain. Energy.* 5 (2013).

[22] S. Simsek and S. Uslu, “Investigation of the effects of biodiesel/2-ethylhexyl nitrate (EHN) fuel blends on diesel engine performance and emissions by response surface methodology (RSM),” *Fuel (Lond.)*, vol. 275, no. 118005, p. 118005, 2020.

[23] Y. Singh, A. Sharma, G. Kumar Singh, A. Singla, and N. Kumar Singh, “Optimization of performance and emission parameters of direct injection diesel engine fuelled with pongamia methyl esters-response surface methodology approach,” *Ind. Crops Prod.*, vol. 126, pp. 218–226, 2018.

[24] M. Krishnamoorthi, R. Malayalamurthi, and P. Mohamed Shameer, “RSM based optimization of performance and emission characteristics of DI compression ignition engine fuelled with diesel/aegle marmelos oil/diethyl ether blends at varying compression ratio, injection pressure and injection timing,” *Fuel (Lond.)*, vol. 221, pp. 283–297, 2018.

[25] M. Pandian, S. P. Sivapirakasam, and M. Udayakumar, “Investigation on the effect of injection system parameters on performance and emission characteristics of a twin cylinder compression ignition direct injection engine fuelled with pongamia biodiesel–diesel blend using response surface methodology,” *Appl. Energy*, vol. 88, no. 8, pp. 2663–2676, 2011.

[26] J. B. Hirkude and A. S. Padalkar, “Performance optimization of CI engine fuelled with waste fried oil methyl ester-diesel blend using response surface methodology,” *Fuel (Lond.)*, vol. 119, pp. 266–273, 2014.

[27] P.M. Shameer, K. Ramesh, Influence of antioxidants on fuel stability of Calophyllum inophyllum biodiesel and RSM-based optimization of engine characteristics at varying injection timing and compression ratio, *J. Brazilian Soc. Mech. Sci. Eng.* 39 (2017) 4251–4273.

[28] R. K. Niven, “Ethanol in gasoline: environmental impacts and sustainability review article,” *Renew. Sustain. Energy Rev.*, vol. 9, no. 6, pp. 535-555, 2005.

[29] I. M. Yusri, R. Mamat, W. H. Azmi, A. I. Omar, M. A. Obed, and A. I. M. Shaiful, “Application of response surface methodology in optimization of performance and exhaust emissions of secondary butyl alcohol-gasoline blends in SI engine,” *Energy Convers. Manag.*, vol. 133, pp. 178–195, 2017.

[30] M. K. Balki, C. Sayin, and M. Canakci, “The effect of different alcohol fuels on the performance, emission and combustion characteristics of a gasoline engine,” *Fuel (Lond.)*, vol. 115, pp. 901–906, 2014.

[31] B. M. Masum, M. A. Kalam, H. H. Masjuki, S. M. Palash, and I. M. R. Fattah, “Performance and emission analysis of a multi cylinder gasoline engine operating at different alcohol–gasoline blends,” *RSC Adv.*, vol. 4, no. 53, pp. 27898–27904, 2014.

[32] M. B. Celik, “Experimental determination of suitable ethanol–gasoline blend rate at high compression ratio for gasoline engine,” *Appl. Therm. Eng.*, vol. 28, no. 5–6, pp. 396–404, 2008.

[33] A. I. Charalampos and K. N. Anastasios, “Panagiotis Gasoline-ethanol, methanol mixtures and a small four-stroke engine,” *Heat and Technology*, vol. 22, pp. 69–73, 2004.

[34] M. N. A. M. Yusoff et al., “Performance and emission characteristics of a spark ignition engine fuelled with butanol isomer-gasoline blends,” *Transp. Res. D Transp. Environ.*, vol. 57, pp. 23–38, 2017.

[35] H. K. Imdadul et al., “Higher alcohol–biodiesel–diesel blends: An approach for improving the performance, emission, and combustion of a light-duty diesel engine,” *Energy Convers. Manag.*, vol. 111, pp. 174–185, 2016.

[36] B.-Q. He, J.-X. Wang, J.-M. Hao, X.-G. Yan, and J.-H. Xiao, “A study on emission characteristics of an EFI engine with ethanol blended gasoline fuels,” *Atmos. Environ. (1994)*, vol. 37, no. 7, pp. 949–957, 2003.

BİTLİS EREN UNIVERSITY
JOURNAL OF SCIENCE AND TECHNOLOGY

E-ISSN: 2146-7706

IMPROVEMENT OF HEAP LEACHING PRACTICES IN UŞAK KIŞLADAĞ GOLD MINE USING LIMESTONE

Aminullah Rashidi [1], **Serdar Yılmaz** [2,*]

[1] *Zonguldak Bülent Ecevit University, Department of Geological Engineering,* Türkiye, emin.resit2010@gmail.com
[2] *Zonguldak Bülent Ecevit University, Department of Mining Engineering,* Türkiye, serdaryilmaz@beun.edu.tr
* *Corresponding author*

KEYWORDS

Gold Recovery
Heap Leach
Limestone
Permeability
Uşak Kışladağ

ARTICLE INFO

Research Article
Doi
10.17678/beuscitech.1573807

Received	October 31, 2024
Revised	April 14, 2025
Accepted	June 23, 2025
Year	2025
Volume	15
Issue	1
Pages	56-79

ABSTRACT

This study focuses on improving gold recovery from ore samples from the Uşak Kışladağ Gold Mine, specifically those sized -18+0 mm. The ore was crushed below 2.36 mm and mixed with locally abundant alkaline limestone to enhance permeability and gold dissolution efficiency. Permeability tests were conducted on the -18+0 mm and -2.36+0 mm sized ores, with results of 1.28 x 10^{-3} cm/s and 0.62 x 10^{-3} cm/s, respectively. Additionally, the -2.36 mm ore was mixed with various limestone sizes (-18+10 mm, -10+5 mm, and -5+0 mm) at ratios of 15%, 50%, 100%, 150%, and 200%. The best permeability results were observed with the -2.36+0 mm ore and -10+5 mm limestone mixture. Consequently, leaching experiments were conducted with 1:1 and 1.5:1 ratio of the -2.36+0 mm sample mixed with limestone, resulting in gold dissolution efficiencies of 63% and 53%, respectively. Furthermore, bottle-roll tests were performed on -2.36+0 mm and -75+0 µm samples for 48 hours, with gold recoveries of 64% and 83%, respectively.

1 INTRODUCTION

Gold and silver extraction methods vary depending on ore quantity, mineralogy, and grade [1]. However, as high-grade ores decline and costs rise, cyanide leaching has become the primary method for low-grade ores, despite its environmental and health risks [2].

Yet, refractory gold ores, where gold is trapped in sulfide minerals like pyrite or arsenopyrite, hinder cyanide leaching due to micron-sized particles and high reagent consumption [3, 4]. Thus, pre-treatments such as roasting at 550°C, pressure oxidation at 225–245°C, and biooxidation—applied since 1986—are used to enhance recovery [5, 6].

Moreover, in heap leaching, permeability is critical, as fine materials can block solution flow. Therefore, agglomeration with coarser particles improves permeability and recovery [7]. In this context, Robertson et al. [8, 9] highlight the role of agglomeration, while Yılmaz et al. demonstrate that nut shell additives enhance permeability and recovery at Uşak Kışladağ Gold Mine [10]. This effect is illustrated in Figure 1, where fine particles exhibit clay-like behavior, impeding uniform solution and gas flow, whereas agglomeration improves permeability and enhances extraction efficiency [11].

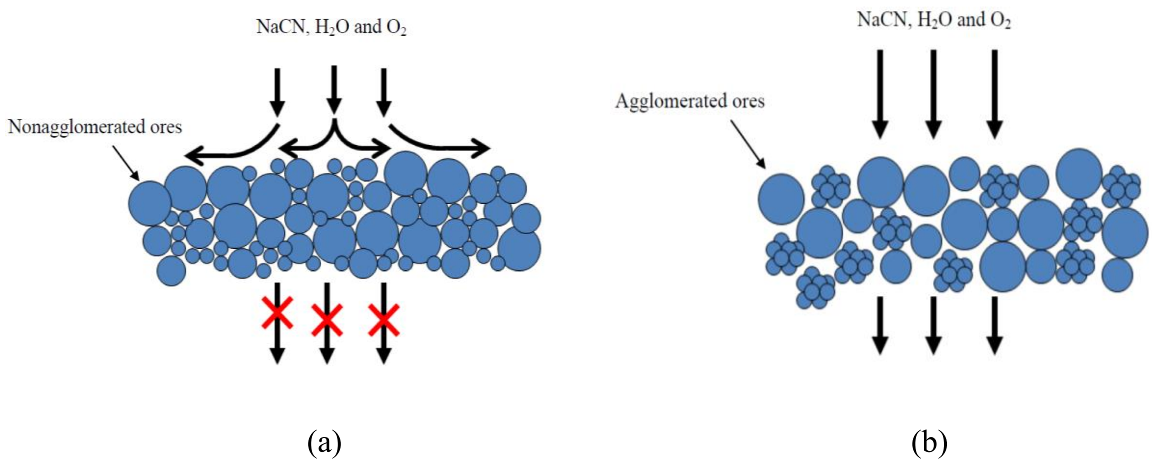

***Figure 1**. Schematic Diagram (a) Illustrating How Fine Particles Exhibit Clay-Like Behavior, Impeding the Uniform Flow of Solution and Gas During Heap Leaching, (b) More Uniform Flow of Solution and Gas in Agglomerated Ore [11].*

Vethosodsakda conducted permeability tests on agglomerated ores, showing increased permeability and reduced leaching times [11]. The results indicated that both particle size and moisture content are key factors in determining permeability. Ores with coarse particles and 6-8% moisture content exhibited high permeability due to the agglomeration process. In this context, Figure 2 illustrates the distribution of ore within the heap, highlighting the difference between actual and desired distribution, with the latter promoting better permeability and solution flow [10].

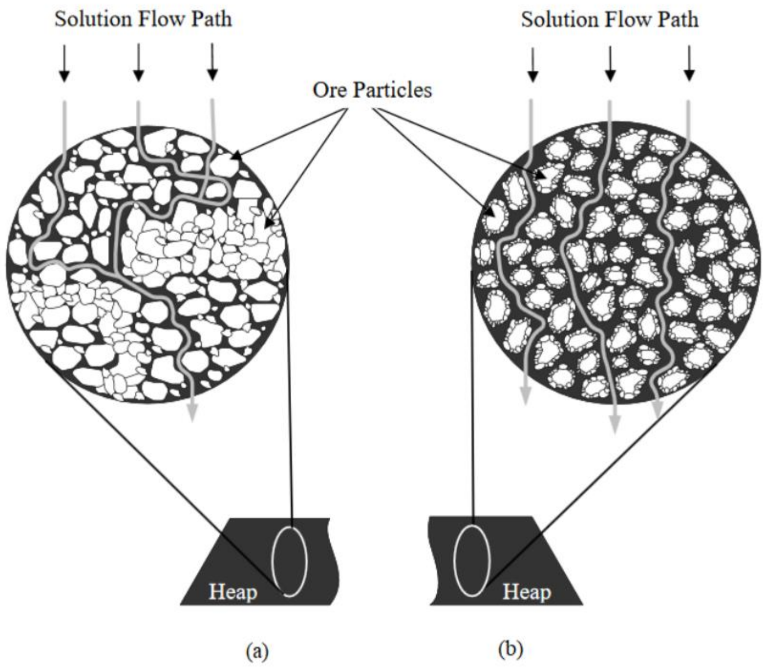

Figure 2*. Distribution of Ore Within the Heap: (a) Actual Distribution, (b) Desired Distribution [10].*

As illustrated in Figure 2, the distribution of ore within the heap can significantly impact permeability. In Figure 2a, fine-grained ore creates an impermeable layer, obstructing the flow of the cyanide solution. However, in Figure 2b, when fine and coarse particles are uniformly distributed, the solution can flow smoothly, thereby increasing gold recovery efficiency [10].

Several factors, including rock type, heap height, and NaCN solution concentration, affect permeability in heap leaching. Excessive fine-grained ores negatively impact permeability due to their clay-like behavior and the formation of channels [12]. Permeability values for materials vary, with fine sands having a permeability of 10^{-5} cm/s, clay-rich soils ranging from 10^{-7} to 10^{-8} cm/s, and sand mixtures and alluvium exhibiting a permeability of 10^{-6} cm/s [13]. Uhrie et al. [14]

noted that increased clay content reduces permeability, with the relationship between clay amount and permeability being inversely proportional.

Finally, as discussed in the Corelab report, changes in water permeability based on clay content and salinity are illustrated in Figure 3 [15]. Kinard and Schweizer [16] also highlighted that heap density is inversely proportional to permeability, with densities ranging from 1.19 to 1.43 t/m³ corresponding to permeabilities from 10^{-4} to 4×10^{-7} cm/s.

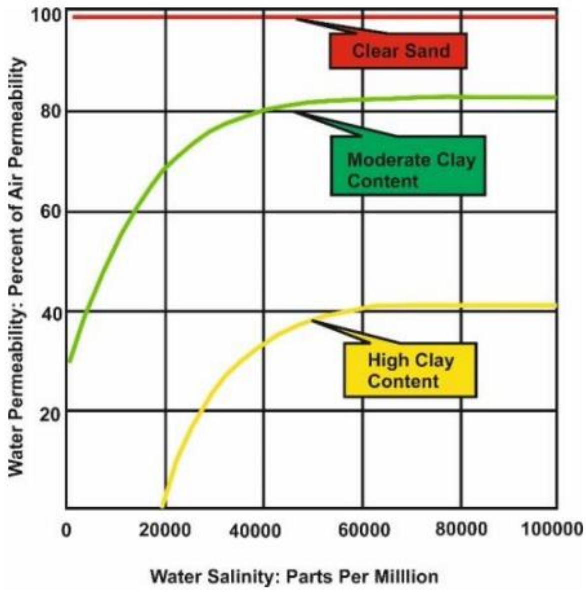

Figure 3. *Water Permeability Based on Clay Content [15].*

Thus, proper management of particle size, moisture content, and permeability through agglomeration and other pre-treatment processes is essential for optimizing heap leaching and ensuring efficient gold recovery. The aim of this study is to investigate the effects of different ore and limestone mixtures on permeability and gold recovery, focusing on optimizing leaching efficiency through various pre-treatment methods to enhance gold extraction from Uşak Kışladağ Gold Mine ore.

The objective of this study is to evaluate the impact of different ore and limestone mixtures on permeability and gold recovery, aiming to optimize leaching efficiency for Uşak Kışladağ Gold Mine ore. By investigating the permeability variations in crushed ore samples of different sizes and limestone mixtures, the study seeks to determine the most effective combination for enhancing solution flow and gold dissolution. Through permeability and leaching experiments, including bottle-roll tests, the research assesses how particle size distribution and limestone addition influence gold recovery, ultimately providing insights into optimizing heap leaching conditions.

2 MATERIAL AND METHOD

The ore from the Kışladağ Gold Mine was crushed to increase surface area and expose gold. To improve permeability, fine ore was mixed with limestone for uniform cyanide flow, enhancing gold dissolution.

Permeability tests were conducted on gold ore samples of various sizes, followed by experiments on (-2.36+0 mm) ore mixed with limestone at different sizes and ratios. The optimal mix was selected for column leaching, and gold dissolution efficiency and rates were analyzed.

2.1 Size and Chemical Analyses Conducted on the Sample

Initially, size and chemical analyses were conducted on the material sized (-18+0 mm) that is currently being applied to the heap at the Kışladağ Gold Mine, as presented in Tables 1 and 2.

Table 1. *Sieve analysis values of material sized (-18+0 mm) currently applied to the heap at kişladağ gold mine.*

Sample Size (mm)	Weight (%)	Cumulative Passing (%)
-25+18	0.5	100.0
-18+10	12.9	99.5
-10+6.70	8.6	86.6
-6.70+4.75	13.8	78.0
-4.75+2.36	18.5	64.2
-2.36+1.00	19.0	45.7
-1.00+0.50	4.1	26.7
-0.50+0.212	6.7	22.6
-0.212+0.150	1.8	15.9
-0.150	14.1	14.1
Total	**100.0**	

Considering Table 1, it can be observed that nearly all of the samples passed through the 18 mm sieve, with approximately 50% passing through the 2.36 mm sieve.

Table 2*. Chemical analysis values of material sized (-18+0 mm) currently applied to the heap at kişladağ gold mine.*

Element	Au	Ag	Al	As	Ba	Be	Bi	Ca	Cd	Co	Cr	Cu	Fe	Ga	K	La	Mg
Unit	ppm	ppm	%	ppm	ppm	ppm	ppm	%	ppm	ppm	ppm	ppm	ppm	%	ppm	%	ppm
Amount	1.32	1.90	7.62	172	320	3.90	8.00	0.66	3.80	25.00	121.00	142.00	3.98	20.00	3.71	50.00	1.26

Element	Mn	Mo	Na	Ni	P	Pb	S	Sb	Sc	Sr	Th	Ti	Tl	U	V	W	Zn
Unit	ppm	ppm	%	ppm	ppm	ppm	%	ppm	ppm	ppm	ppm	%	ppm	ppm	ppm	ppm	ppm
Amount	396	104	1.00	35	1090	909	3.70	13	10	604	30	0.24	10	<10	84	10	2000

The chemical analysis of the material brought from the Uşak Kışladağ Gold Mine shows that the gold grade is 1.32 ppm, the silver grade is 1.90 ppm, and the sulfur content is 3.7%. The material was analyzed across different size groups, and the results are presented in Table 3.

Table 3*. Gold (Au) analysis values by sample size.*

Size (mm)	Amount (%)	Grade (ppm)	Distribution (%)
-25+18	0.5	0.70	0.24
-18+10	12.9	0.80	7.85
-10+6.70	8.6	0.85	5.56
-6.70+4.75	13.8	0.88	9.19
-4.75+2.36	18.5	1.10	15.35
-2.36+1.00	19.0	1.73	24.98
-1.00	26.7	1.81	36.59
Total	**100.0**	**1.32**	**100.0**

Considering Table 3, it can be observed that as the sample size decreases, the Au values increase. This increase in Au values is attributed to the growing surface area, which facilitates the liberation of gold as the size reduces. The most significant increase occurs in the ore size below 2.36 mm, which is why material under 2.36 mm is utilized in heap leaching.

Permeability Tests

Permeability in heap leaching directly affects the contact of the cyanide solution with gold in the ore, thereby increasing gold recovery efficiency.

In heap leaching, fine-sized gold ores can lead to channeling due to clay-like behavior, resulting in low permeability and diminished gold dissolution efficiency. To minimize this low gold dissolution rate, permeability tests were conducted using the "Column Leaching Test Set" method. Before conducting the column leaching tests, permeability experiments were performed on mixtures of the gold ore sized (-2.36+0 mm) with limestone in various sizes and percentage ratios. The results were analyzed to select the most suitable mixture for heap leaching. Initially, a particle size analysis of the selected (-2.36+0 mm) sample for permeability testing was conducted, and the results are presented in Table 4. Permeability tests were conducted using limestone at ratios of 15%, 50%, 100%, 150%, and 200%, while keeping the ore size constant at -2.36+0 mm. Limestone was used in three different size ranges: -18+10 mm, -10+5 mm, and -5+0 mm.

Table 4*. Size distribution of the selected -2.36 mm sized ore for permeability.*

Sample Size (mm)	Weight (%)	Cumulative Undersize Ratio (%)
-2.36+1.70	12.4	100.0
-1.70+1.00	36.5	87.6
-1.00+0.50	22.4	51.1
-0.50+0.30	7.0	28.7
-0.30+0.150	9.0	21.7
-0.150+0.075	5.5	12.7
-0.075+0.045	3.5	7.2
-0.045	3.7	3.7
Total	**100.0**	

As shown in Table 4, approximately 51.1% of the sample distribution, reduced to a size below 2.36 mm, is below the 1.00 mm size.

Permeability tests were conducted in laboratory using the Permeability Test Set, set up according to the "Constant Head Permeability Test" process of Darcy's Law. The permeability tests were performed in accordance with ASTM D2434 (ASTM, 2006) standards. The schematic representation of the Constant Head Permeability Test Set is shown in Figure 4, and an image of the permeability test set available in our laboratory is presented in Figure 5.

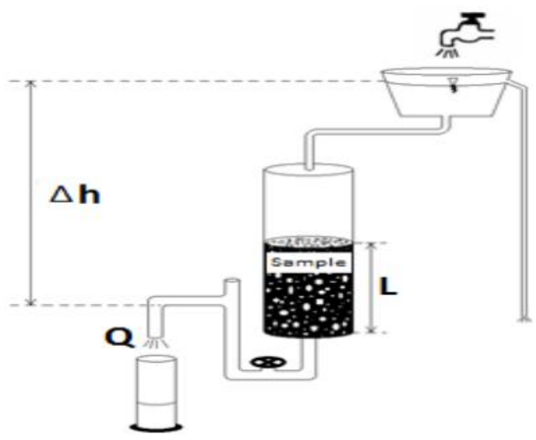

Figure 4*. Schematic representation of the constant head permeability test set [2].*

Figure 5. *Image of the permeability test set taken during permeability experiments.*

The permeability value is mathematically calculated using the formula (1):

$$K = \frac{Q * L}{A * t * \Delta h} \quad (1)$$

Where:

K: Permeability value (cm/s)

Q: Volume of discharged water (cm^3)

L: Sample height (cm)

A: Sample surface area (cm^2)

t: Discharge time (60 s)

Δh: Distance between the discharge point in the bucket and the discharge point at the bottom of the column (cm).

In all permeability tests conducted in ore preparation laboratory, the ore size was kept constant at (-2.36+0 mm), while the limestone size was varied.

2.2 Bottle Roll Tests

Gold dissolution efficiency tests were conducted on two different sample sizes (-2.36+0 mm and -75+0 μm) using an Atomic Absorption Spectrophotometer

(AAS). The Bottle Roll experiments, shown in Figure 6, involved periodic sampling at 2, 4, 8, 24, and 48 hours to analyze gold dissolution efficiency. The tests were performed on ore from the Uşak Kışladağ Gold Mine, and dissolution values were calculated using AAS to evaluate the effectiveness of the process.

Figure 6. *Image of the "bottle-roll" experiment setup.*

To determine gold dissolution efficiency, the following materials were used in the "Bottle-Roll" experiment conducted in our laboratory with 2.5-liter bottles:

- **Sample Amount**: 500 g
- **Water Volume**: 1 L
- **pH Adjustment and Value:** Adjusted with lime powder/$Ca(OH)_2$ to 10.5
- **NaCN Amount**: 1 g

2.3 Column Leaching" Experiments Conducted in Columns

The gold ore was thoroughly mixed with limestone sized (-10+5 mm). To create a basic environment (pH=10.5), hydrated lime was added to the sample and mixed well. Approximately 10% water was added to ensure proper agglomeration of the sample and limestone. The prepared sample was placed into the column leaching set available in our laboratory. A sodium cyanide (NaCN) solution was prepared at a concentration of 1 g/L, totaling 5 liters. After 24 hours, a loaded solution (gold solution) formed at the bottom of the columns, which was then transferred to activated carbon. The resulting barren solution was recycled back into the system, creating a closed-loop for the column leaching experiments. Samples were taken from both the loaded and barren solutions over a month (30 days) to calculate gold values. Initially, activated carbon was loaded at the start of the experiment, with a second loading performed on the 10th day. Samples from the activated carbon were collected at the end of the 10th and 30th days, dried, and prepared for analysis to determine the amount of gold absorbed by the activated carbon. In the column leaching experiments, the initial focus was on ores sized (-18+0 mm) and (-2.36+0 mm) (Figure 7).

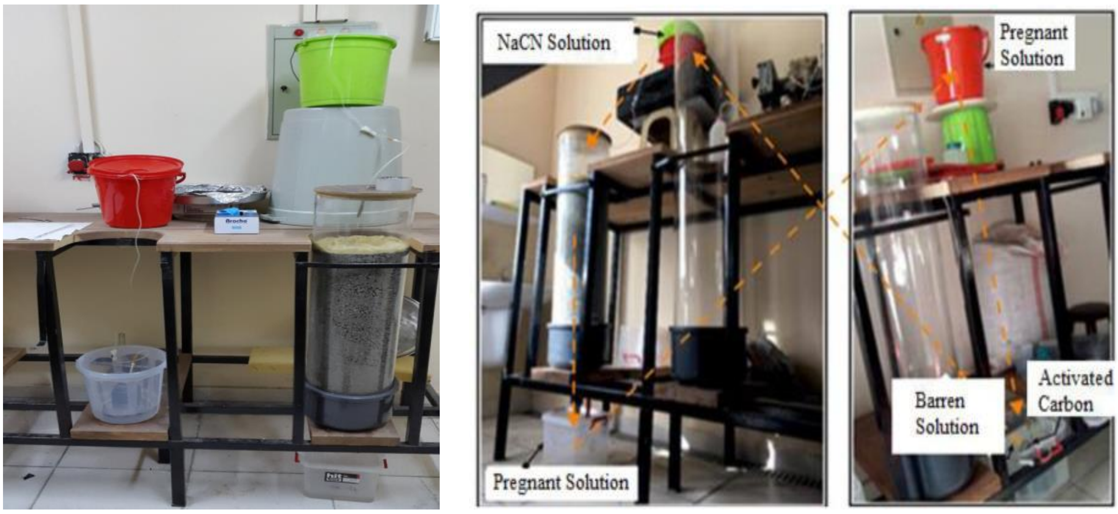

Figure 7. *Image of the Pilot-Scale "Column Leaching Set.".*

2.4 Column Leaching Experiments with Limestone Mixture

In the experiments conducted, the gold particles within the ore brought from the Uşak Kışladağ Gold Mine were liberated after the ore was crushed to a size of -2.36+0 mm. The ore was then mixed with limestone in two different ratios: 1:1 and 1.5:1. Additionally, limestone sized -10+5 mm was used in the experiments due to its better mixing properties. In the column leaching experiment using the 1:1 limestone mixture, the -2.36+0 mm ore was homogeneously mixed with -10+5 mm limestone and approximately 10% water. The mixture was then fed into the columns for the experiments.

3 RESULTS AND DISCUSSION

In this section, permeability tests, bottle roll experiments, and column leaching experiments are addressed separately, with results discussed alongside corresponding figures are provided accordingly. Trends and cause-and-effect relationships are explicitly identified, such as the impact of particle size on permeability and gold dissolution efficiency. Additionally, key findings are summarized at the end of each subsection as in the following.

3.1 Permeability Tests

The permeability test conducted on the ore with a size of (-2.36+0 mm) without the addition of limestone resulted in a permeability value of 0.62×10^{-3} cm/s, while the permeability value for the ore with a size of (-18+0 mm) was determined to be 1.28×10^{-3} cm/s.

Permeability tests were conducted using limestone at 15%, 50%, 100%, 150%, and 200% ratios. The resulting values from these experiments are presented in the graphs between Figure 8 and Figure 12.

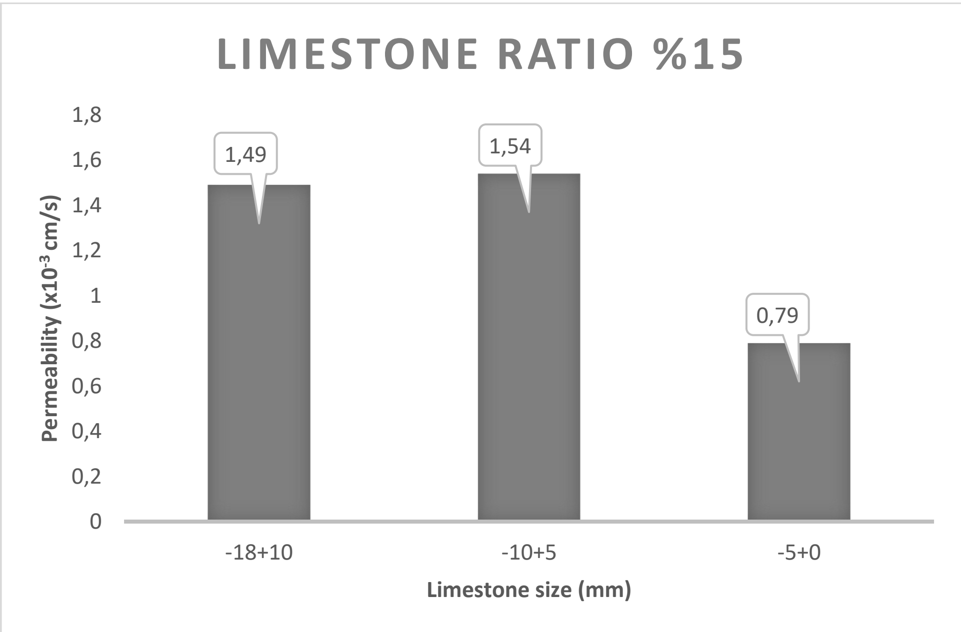

***Figure 8**. The effect of permeability with the mixture of limestone of different sizes at a 15% ratio.*

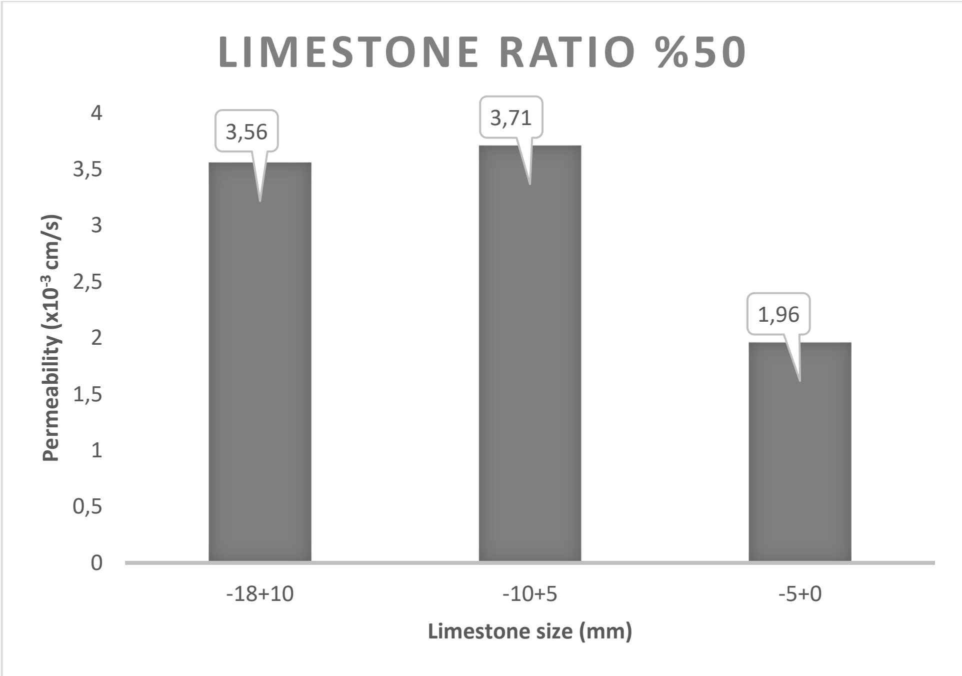

Figure 9. *The effect of permeability with the mixture of limestone of different sizes at a 50% ratio.*

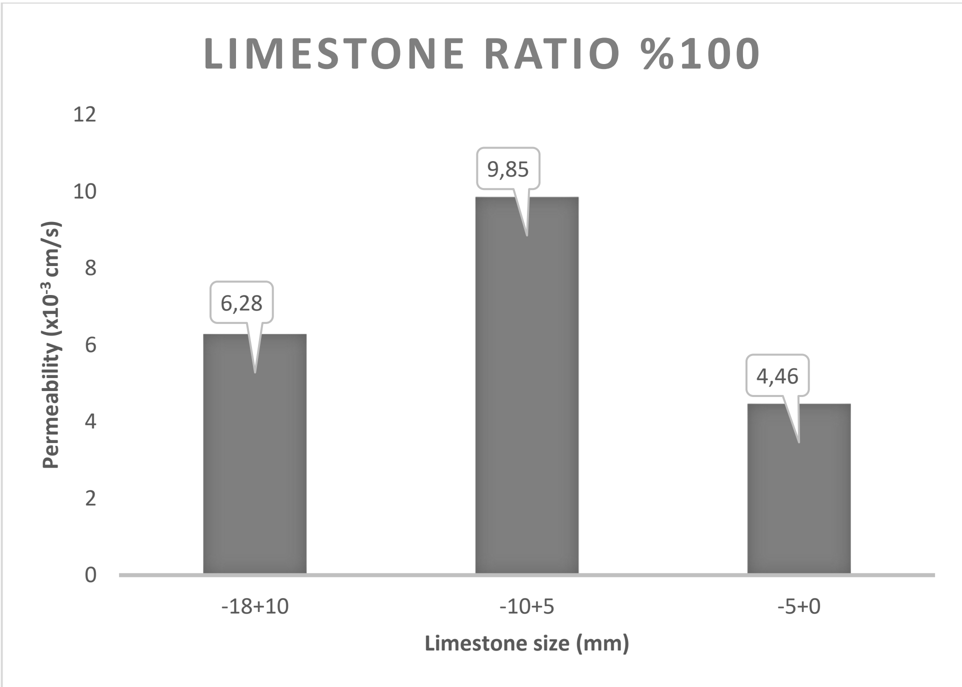

Figure 10. *The effect of permeability with the mixture of limestone of different sizes at a 100% ratio.*

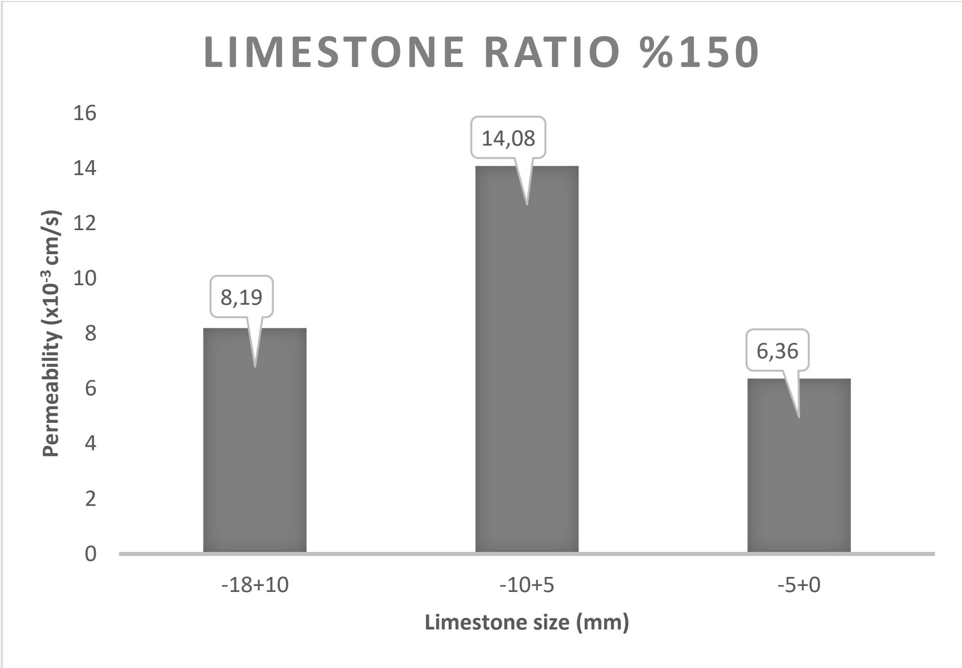

***Figure 11**. The effect of permeability with the mixture of limestone of different sizes at a 150% ratio.*

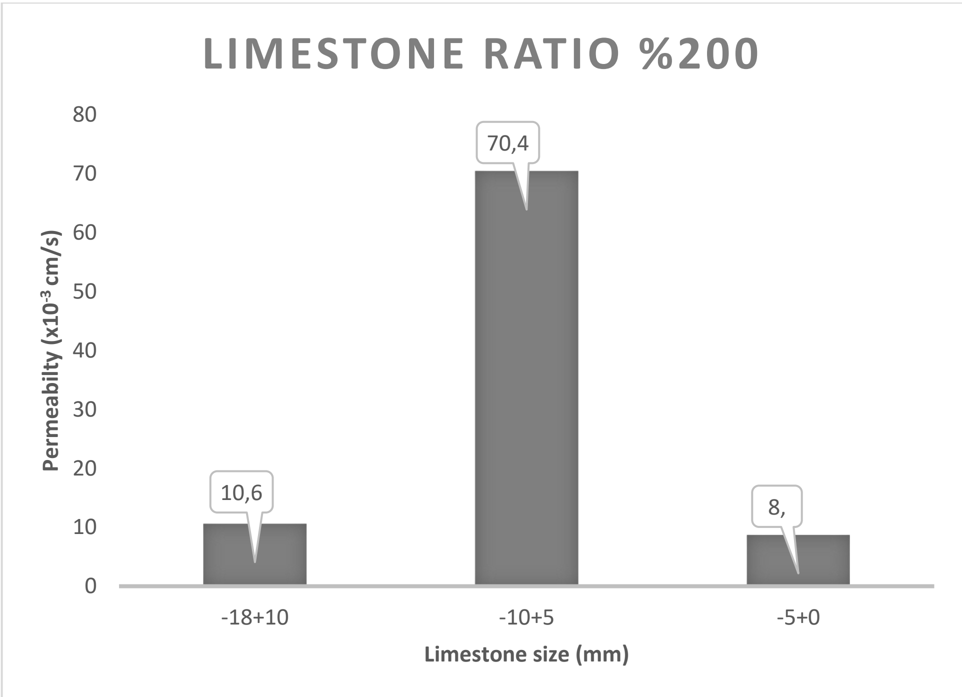

***Figure 12**. The effect of permeability with the mixture of limestone of different sizes at a 200% ratio.*

As a result of the permeability tests conducted with the sample and limestone mixture:

- It was observed that as the limestone particle size decreased, permeability also decreased; even the dust generated from smaller limestone particles adversely affected permeability.
- An increase in limestone particle size led to an increase in permeability; however, excessively large particles did not yield efficient results in permeability tests due to disaggregation.
- An increase in the percentage of limestone in the mixture resulted in higher permeability test results, while a decrease in the percentage led to reduced permeability.
- Among the permeability tests conducted with different limestone sizes, the best results were observed with the mixture of the sample and limestone of size (-10+5 mm).

The limestone of size -10+5 mm, which demonstrates a better mixing structure with the sample, is of significant importance to our study because it yields better results in permeability tests compared to the limestones of sizes -18+10 mm and -5+0 mm.

3.2 Bottle Roll Experiments Results

In this study, Bottle-Roll experiments were performed on two different gold ore sizes: (-2.36+0 mm) and (-75+0 µm) to evaluate gold dissolution efficiency. The results obtained from these experiments provide insights into the leaching behavior of different particle sizes. The dissolution trends and efficiency values for both ore sizes are illustrated in Figure 13 and Figure 14, where Figure 13 presents the dissolution behavior of the -2.36+0 mm sample, while Figure 14 displays the results for the -75+0 µm sample. These figures highlight the impact of particle size on the dissolution process and provide a comparative analysis of the leaching performance under the experimental conditions.

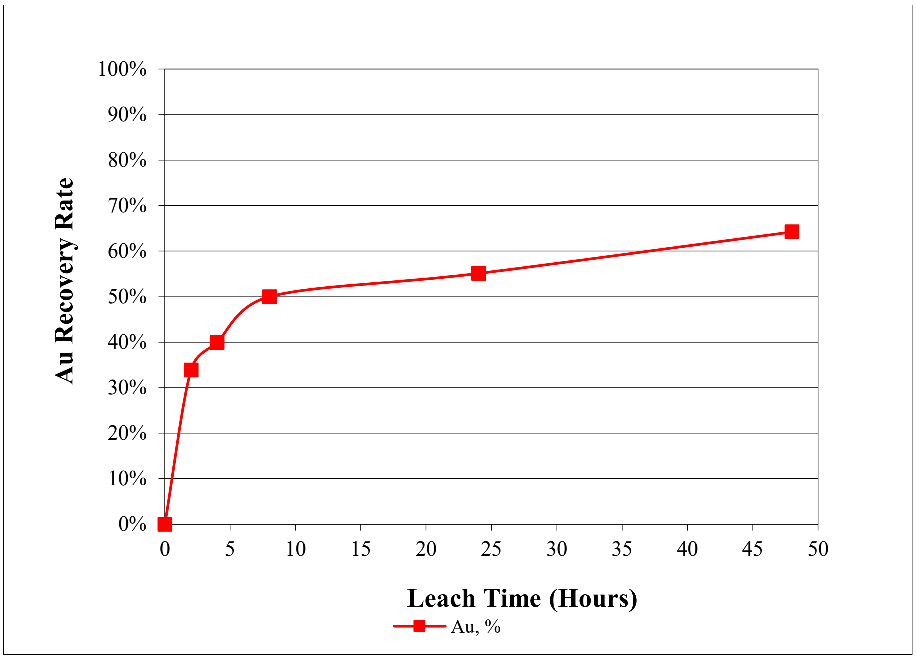

***Figure 13**. Graph of the "Bottle-Roll" experiment conducted with the sample of size -2.36+0 mm.*

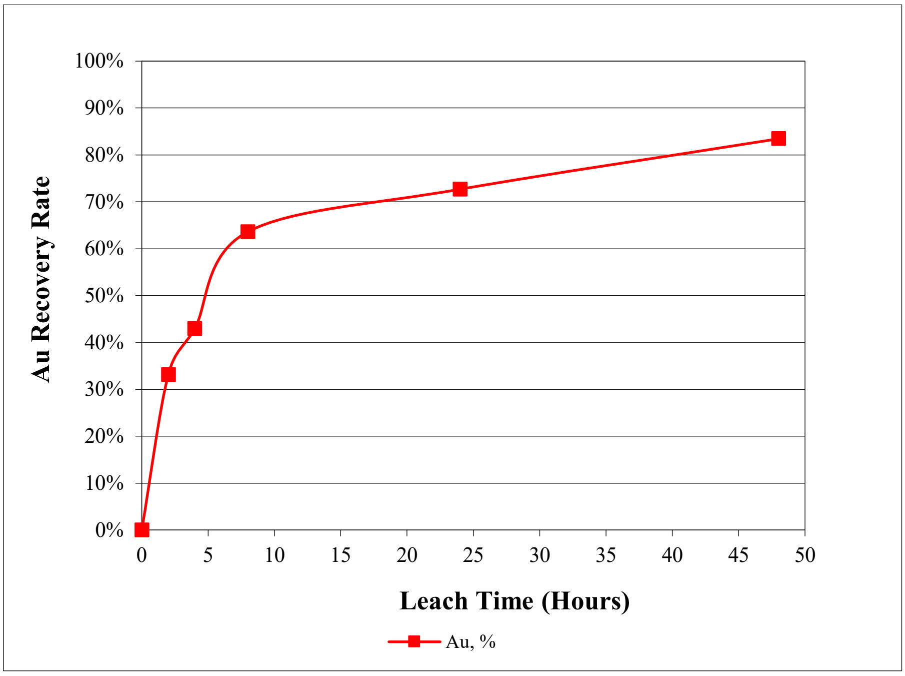

***Figure 14**. Graph of the "Bottle-Roll" experiment conducted with the sample of size -75+0 μm.*

The results of the conducted experiments are as follows:

- The gold recovery rate for the (-2.36+0 mm) gold ore was found to be: 64%
- The gold recovery rate for the (-75+0 μm) gold ore was determined to be: 83%

From the analysis of these results, it was observed that as the size of the ore increases, the gold recovery rate decreases. Conversely, a decrease in ore size leads to an increase in gold recovery efficiency. This is because the finer the gold ore is subjected to crushing or grinding, the more gold particles become liberated, allowing for better contact with the cyanide solution and subsequently improving dissolution.

3.3 Column Leaching Experiments

In column leaching experiments, the ores with sizes (-18+0 mm) and (-2.36+0 mm) were initially used. The Au dissolution yield was determined over a period of 30 days. After another 30-day leaching period, the Au recovery efficiency was calculated. The Au dissolution rate as a function of leaching time for the ore sized -18+0 mm is presented graphically in Figure 15.

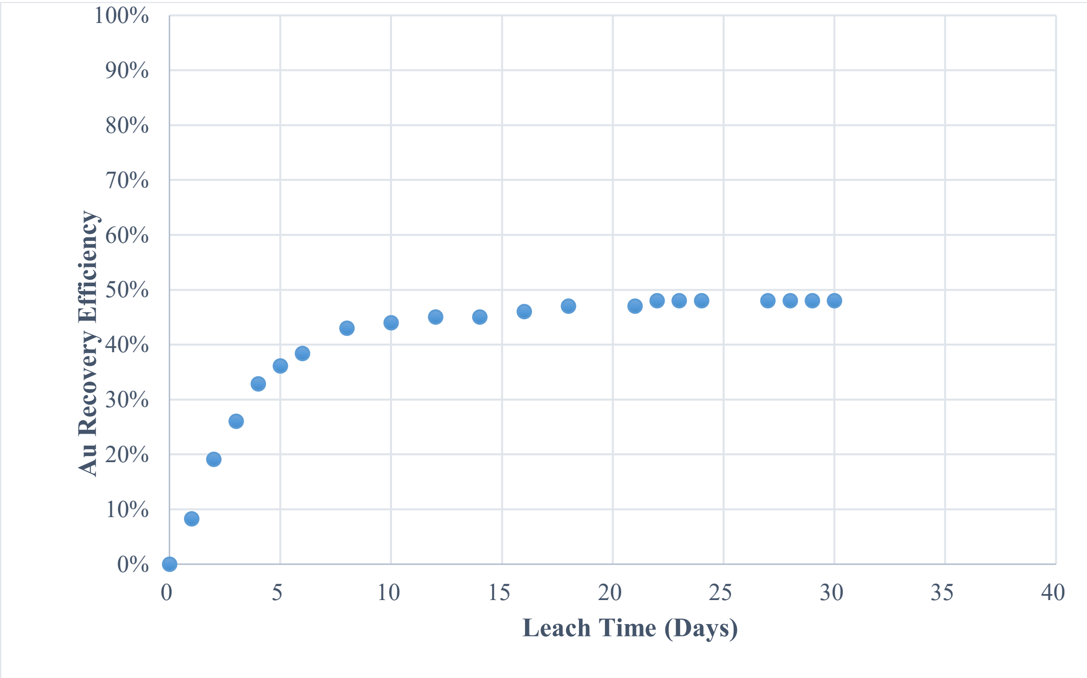

***Figure 15**. Graph of Au Recovery Efficiency Based on Leaching Time for (-18+0 mm) Gold Ore.*

At the Uşak Kışladağ Gold Mine, after a leaching period of 30 days for the ore sized (-18+0 mm):

- The gold recovery efficiency (Au dissolution rate) was determined to be 48%.

Subsequently, to enhance particle liberation, the ore was crushed to a size of -2.36+0 mm, and a second column leaching experiment was conducted. The Au dissolution yield was calculated at the end of the 30-day leaching period. The Au dissolution yield of the ore with a size of -2.36+0 mm as a function of leaching time is presented in the graph in Figure 16.

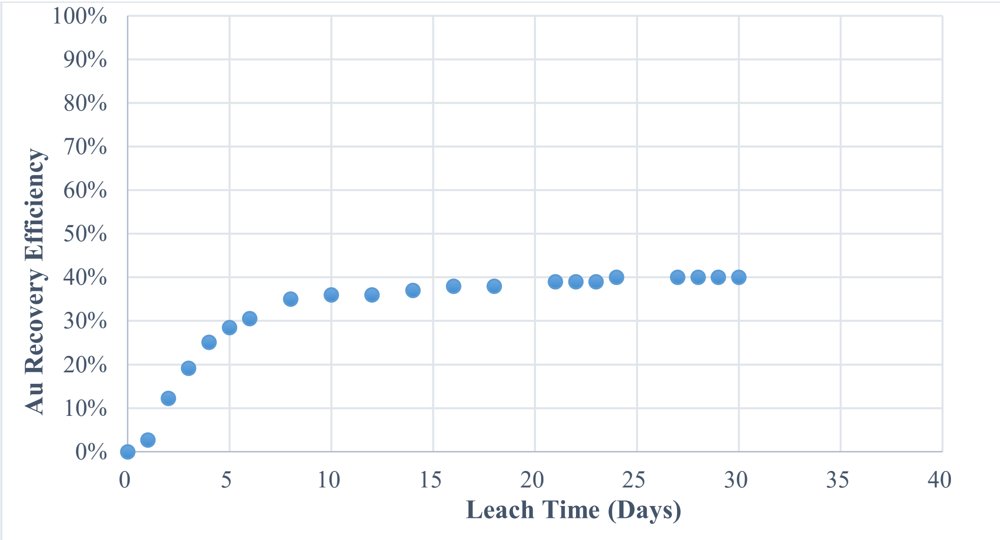

Figure 16. *Graph of Au dissolution efficiency as a function of leaching time for ore sized -2.36+0 mm.*

At the Uşak Kışladağ Gold Mine, the Au dissolution yield of the ore fed to the heap with a size of -2.36+0 mm was determined to be 42% after a 30-day leaching period.

Based on the graphs in Figures 15 and 16, it can be observed that the Au dissolution efficiency for ore sized -2.36+0 mm has decreased compared to that of -18+0 mm ore. This decline is attributed to the increased presence of fine particles within the ore, which leads to reduced permeability and Au dissolution efficiency. Consequently, the solution fails to effectively contact the gold particles within the ore.

To enhance both permeability and Au dissolution efficiency for the -2.36+0 mm ore, subsequent column leaching experiments were conducted using mixtures with limestone. This approach allowed for a thorough investigation of the effects on Au dissolution.

3.4 Column Leaching Experiments with Limestone Mixtures

In this study, experiments were conducted using ore from the Uşak Kışladağ Gold Mine, where the gold particles within the ore were released by crushing the ore to a size of -2.36+0 mm. The crushed ore was mixed with limestone in two different ratios: 1:1 and 1.5:1. The -10+5 mm sized limestone was utilized in the experiments due to its better mixing properties with the ore.

In the column leaching experiment conducted with the 1:1 limestone mixture, the -2.36+0 mm sized ore was homogeneously mixed with 10% moisture and -10+5 mm sized limestone. This mixture was then fed into the columns for the leaching process. The experiment was conducted in a closed-loop system over a period of 30 days. The results regarding the leaching duration and gold dissolution efficiency are illustrated in Figure 17.

This approach aimed to optimize gold recovery through effective mixing and interaction of the cyanide solution with the ore particles.

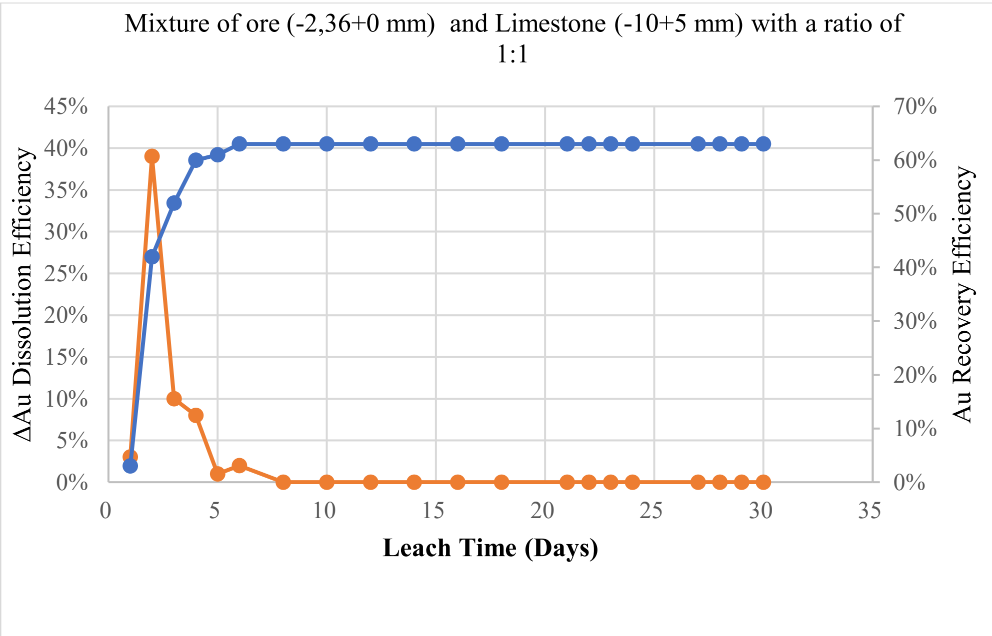

Figure 17*. Au dissolution graph of the sample sized -2.36+0 mm subjected to leaching over time with a limestone mixture in a ratio of 1:1.*

In Figure 17, after a leaching period of 30 days with a limestone mixture in a ratio of 1:1, the Au dissolution efficiency of the sample sized -2.36+0 mm was determined to be 63%. Subsequently, the results of the column leaching experiment conducted with a limestone mixture in a ratio of 1.5:1 are presented graphically in Figure 18.

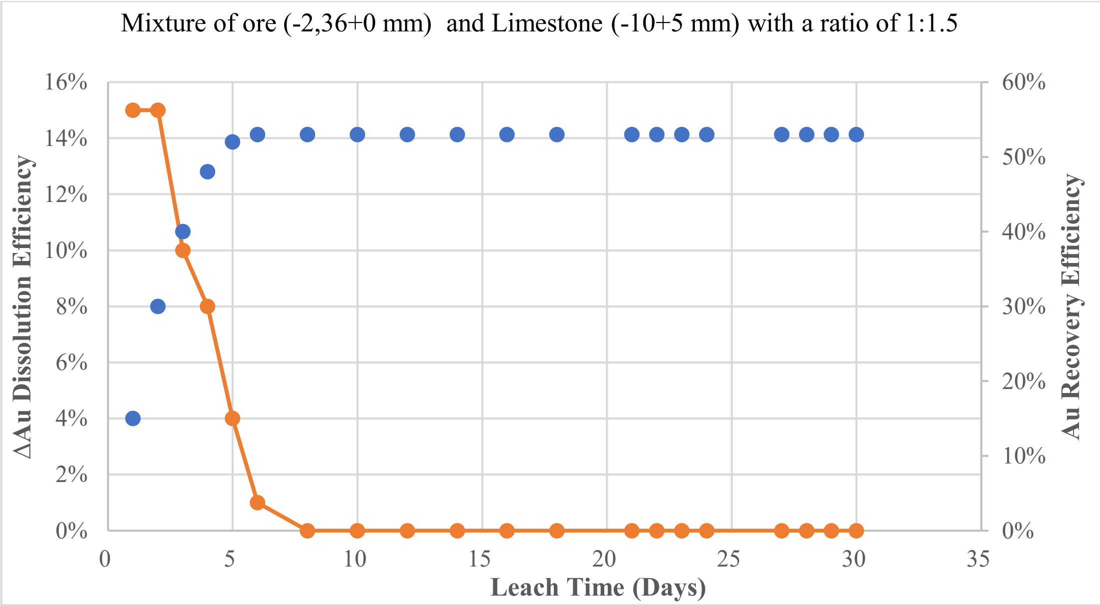

Figure 18*. Au dissolution graph of the sample sized -2.36+0 mm, conducted with a limestone mixture in a ratio of 1.5:1.*

At the end of the 30-day leaching period for the sample with a size of -2.36+0 mm mixed with limestone in a 1.5:1 ratio, the following results were observed:

- The Au dissolution efficiency was determined to be 53%.

The leaching experiments conducted with the -2.36+0 mm sample combined with limestone ores in ratios of 1:1 and 1.5:1 showed Au dissolution efficiencies of 63% and 53%, respectively. Although the leaching experiments with the -2.36+0 mm sample mixed with limestone in a 1.5:1 ratio positively affected permeability, it was noted that the dissolution efficiency of Au decreased compared to the 1:1 limestone mixture. This decrease can be attributed to the complete permeability of the medium and the leaching solution's insufficient contact with the gold particles within the ore.

3.5 Investigation of the Rate of Gold Dissolution by Cyanide Solution in the Ore

The variations in the dissolution rate of gold particles within the ore by sodium cyanide solution, based on the leaching duration, have been analyzed. The gold dissolution rate (Au dissolution rate) and gold dissolution efficiency (Au dissolution efficiency) are presented in graphical form between Figures 19-21.

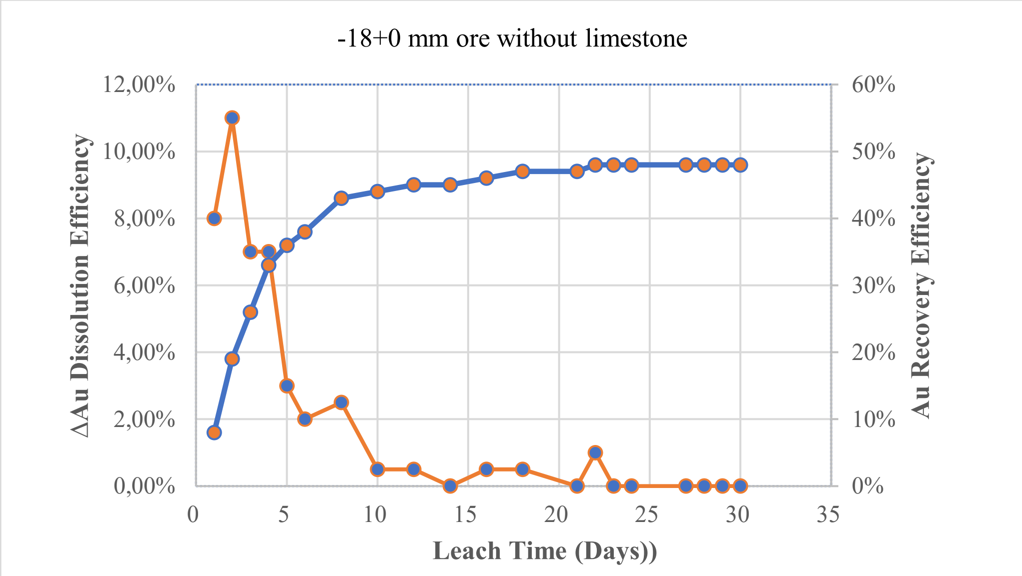

***Figure 19**. Au dissolution rate graph based on the leaching duration for the sample with a particle size of -18+0 mm.*

According to Figure 27, when examining the Au dissolution rate based on the leaching duration for the -18+0 mm sized sample from the Uşak Kışladağ Gold Mine:

- The Au dissolution rate on the first day was 8%,
- On the second day, the Au dissolution rate increased to 11% compared to the first day,
- The dissolution rates on subsequent days showed a decline.

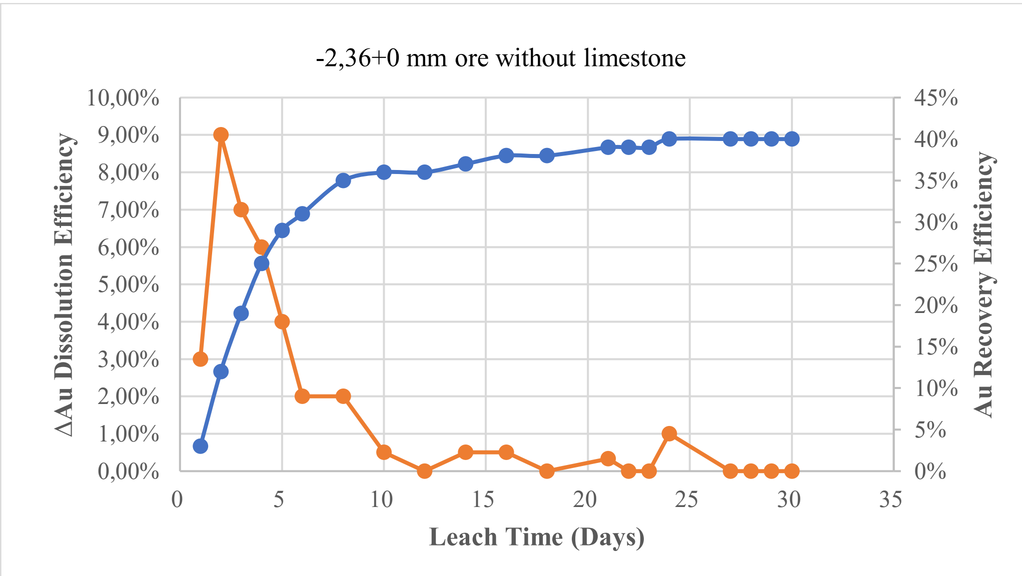

***Figure 20**. Au dissolution rate over time for the -2.36+0 mm sized sample.*

When examining the Au dissolution rate for the sample crushed to -2.36+0 mm without mixing limestone during the leaching process:

- The Au dissolution rate on the first day was 3%.
- By the second day, the Au dissolution rate increased to 9%.
- In the subsequent days, the Au dissolution rates decreased.

This reduction in both Au dissolution rate and Au recovery can be attributed to a decrease in permeability.

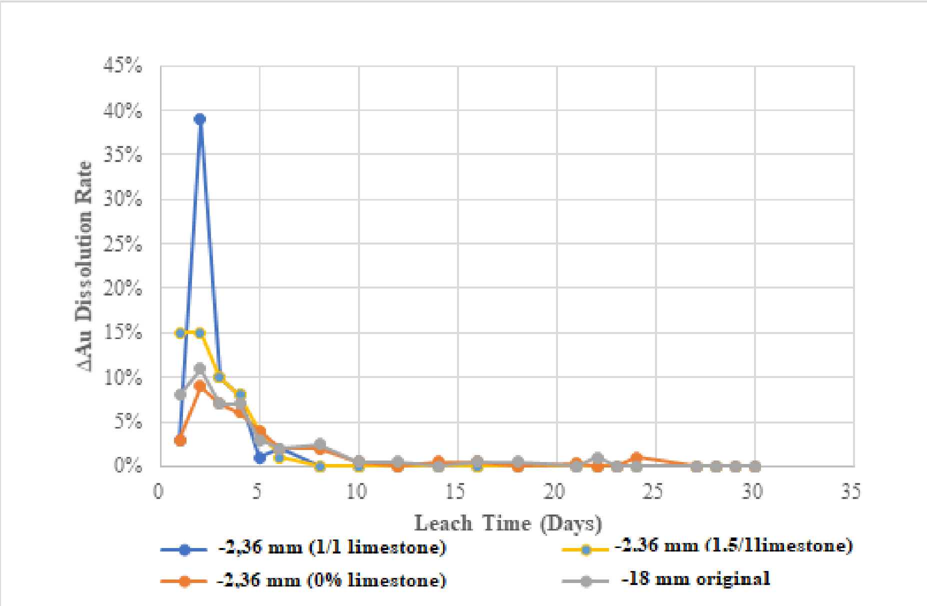

***Figure 21**. Graph of the changes in gold dissolution rate by the cyanide solution throughout the leaching duration.*

When examining the graphs in Figure 21:

- The highest Au dissolution (recovery) rate on the first day occurred with the -2.36+0 mm sized ore mixed with limestone at a 1:1.5 ratio.
- On the second day, the highest Au dissolution rate was observed with the -2.36+0 mm sized ore mixed with limestone at a 1:1 ratio.
- The lowest Au dissolution rate was found in the -2.36+0 mm sized ore without any limestone, which is attributed to low permeability.
- Among the experiments, the best gold dissolution rate and overall recovery were achieved with the -2.36+0 mm sized ore mixed with limestone at a 1:1 ratio.

The findings indicate several cause-and-effect relationships influencing gold recovery efficiency. A decrease in ore size increases surface area, leading to greater gold liberation and a higher gold grade in finer particles. The addition of limestone improves permeability, enhancing cyanide solution penetration and gold recovery; however, excessively fine limestone particles can reduce permeability due to their clay-like behavior. Crushing the ore to finer sizes (-75+0 μm) significantly increases gold dissolution efficiency (83% compared to 64%), demonstrating the impact of ore fineness on recovery. Additionally, mixing the ore with limestone at specific ratios (1:1 or 1.5:1) enhances permeability, leading to improved gold dissolution efficiency (from 42% to 63%). These results highlight how modifications in ore size, permeability, and limestone composition directly affect the efficiency of gold extraction.

4 CONCLUSION

This study focused on the investigation of gold recovery efficiency and permeability in ores obtained from the Uşak Kışladağ Gold Mine. The -18+0 mm sized ore was crushed to below 2.36 mm and mixed with locally abundant alkaline limestone to enhance particle liberation. The results indicated that the size of the limestone significantly influenced the permeability; specifically, as the limestone size decreased, permeability diminished due to the formation of dust, whereas increasing the limestone size enhanced permeability. However, excessively large limestone particles also led to suboptimal results due to segregation.

The study-utilized bottle roll tests to evaluate the gold dissolution efficiency, which yielded a recovery rate of 64% for -2.36+0 mm samples and 83% for -75+0 μm samples. In column leaching experiments without any mixtures, the gold recovery rates were found to be 48% for -18+0 mm samples and 40% for -2.36+0 mm samples, demonstrating that increasing particle size enhances permeability and consequently improves gold recovery efficiency. Conversely, smaller particle sizes led to a reduction in permeability and gold recovery due to the clay-like behavior of fine particles.

Subsequent experiments involving a mixture of -2.36+0 mm ore and -10+5 mm limestone in ratios of 1:1 and 1.5:1 resulted in gold recovery rates of 63% and

53%, respectively. The 1.5:1 mixture, although beneficial for permeability, did not allow the cyanide solution to contact the gold particles as effectively as the 1:1 mixture, indicating that optimal conditions for gold recovery depend on achieving a balance between particle size and solution permeability.

Throughout all experiments, the homogeneous flow of sodium cyanide solution was maintained, effectively mitigating the negative impact of fine particle presence on permeability. This approach enhanced particle liberation, ultimately leading to high gold recovery efficiency. The findings underscore the importance of optimizing ore preparation techniques to improve the overall efficacy of gold extraction processes.

Conflict of Interest

There is no conflict of interest between the authors.

Authors Contributions

Aminullah Rashidi: Investigation, Methodology, Formal Analysis, Data Curation, Writing – Original Draft.

Serdar Yılmaz: Conceptualization, Supervision, Methodology, Writing, Review & Editing, Validation, Project Administration.

Acknowledgment and Support

This study was supported by the Scientific Research Projects (BAP) Program under project number 2019-98150330-01. We would like to express our gratitude for the financial support provided, which made this research possible.

Statement of Research and Publication Ethics

The study is complied with research and publication ethics.

Artificial Intelligence (AI) Contribution Statement

This manuscript was entirely written, edited, analyzed, and prepared without the assistance of any artificial intelligence (AI) tools. All content, including text, data analysis, and figures, was solely generated by the authors.

REFERENCES

[1] O. Celep, “Gold recovery from Mastra ve Kaletaş (Gümüşhane) ores”, M. Sc. Thesis, Karadeniz Technical University, Trabzon, 2025.

[2] S. Yılmaz, “The effect of heap permeabilyt on gold dissolution efficiency”, PhD Thesis, Bülent Ecevit Üniversitesi, Zonguldak, 2018.

[3] H. Çiftçi, “Biooxidation of refractory gold ore and concentrates”, PhD Thesis, Süleyman Demirel Üniversitesi, Isparta, 2008.

[4] A. Akçıl ve H. Çiftçi, “Pretreatments Applied to Refractory Gold Ores”, *Madencilik*, c. 48, sy 1, ss. 17-30, 2009.

[5] A. Turan, “Keban bölgesindeki piritik refrakter altın cevherlerinin yangın tahlilinin optimizasyonu”, M. Sc. Thesis, İstanbul Teknik Üniversitesi, İstanbul, 2009.

[6] H. Çelik, “Using Biooxidation Method for the Pretreatment of Refractory Gold Ores/Concentrates”, *Madencilik*, c. 44, sy 3, ss. 35-46, 2005.

[7] S. Güney ve Ş. T. Azgın, “Altın Madenciliğinde, Yığın Liç Alanlarının Rehabilitasyonunda Yeraltı Suyu İle Yıkanma Yaklaşımının Değerlendirilmesi”, *Erciyes Üniversitesi Fen Bilim. Enstitüsü Fen Bilim. Derg.*, c. 39, sy 2, Art. sy 2, Ağu. 2023.

[8] S. W. Robertson, P. Basson, S. Brill, P. J. van Staden, ve J. Petersen, “Properties governing the flow of solution through crushed ore for heap leaching: Part III – Low-permeability ores”, *Hydrometallurgy*, c. 224, s. 106247, Şub. 2024, doi: 10.1016/j.hydromet.2023.106247.

[9] S. W. Robertson, P. J. van Staden, A. Cherkaev, ve J. Petersen, “Properties governing the flow of solution through crushed ore for heap leaching”, *Hydrometallurgy*, c. 208, s. 105811, Şub. 2022, doi: 10.1016/j.hydromet.2021.105811.

[10] S. Yilmaz, A. A. Sirkeci, M. Bilen, İ. Yigit, ve S. Kizgut, “The effect of nut shell addition on the permeability of a crushed gold ore”, *Physicochem. Probl. Miner. Process.*, c. 54, sy 2, ss. 467-475, Ağu. 2017, doi: 10.5277/ppmp1826.

[11] T. Vethosodsakda, “Evaluation of crushed ore agglomeration, liquid retention capacity, and column leaching”, M. Sc. Thesis, University of Utah, Utah, 2012.

[12] M. Milczarek, T. Yao, M. Banerjee, ve J. Keller, “Ore permeability methods of evaluation and application to heap leach optimization”, program adı: Heap Leach Solutions, Eyl. 2013, ss. 403-415.

[13] S. Bouffard, “Review of agglomeration practice and fundamentals in heap leaching”, *Miner. Process. Extr. Metall. Rev. - Min. PROCESS EXTR Met. REV*, c. 26, ss. 233-294, Tem. 2005, doi: 10.1080/08827500590944009.

[14] J. L. Uhrie, L. E. Wilton, E. A. Rood, D. B. Parker, J. B. Griffin, ve J. R. Lamanna, “The metallurgical development of the Morenci MFL project.”, *VI—Hydrometallurgy of Copper (Book 1)*, Santiago: (P. A. Riveros et al., Eds.), 2003, ss. 29-37.

[15] CoreLab. (1983). New Mexico Teacher University. Retrieved from http://infohost.nmt.edu/~petro/faculty/Engler524/PET524-2a-permeability.pdf

[16] A. A. Kinard, “Schweizer Engineering Properties of Agglomerated Ore in a Heap Leach Pile,” in *Society for Mining*, 1987.

BİTLİS EREN UNIVERSITY
JOURNAL OF SCIENCE AND TECHNOLOGY

E-ISSN: 2146-7706

A TWO-STEP WITH FIRST AND SECOND DERIVATIVE SCHEME FOR NUMERICAL SOLUTION OF FIRST-ORDER PROBLEMS IN DYNAMICAL SYSTEMS

Jamiu Garba [1,*], Umaru Mohammed [2], Oyewole Oyelami [3]

[1] *Department of Mathematics, Federal University of Technology Minna, Nigeria, jamiu.garba@st.futminna.edu.ng*
* *Corresponding author*
[2] *Department of Industrial Mathematics, Federal University of Technology Minna, Nigeria, umaru.mohd@futminna.edu.ng*
[3] *Department of Mathematics, National Open University of Nigeria, Nigeria, ooyelami@noun.edu.ng*

KEYWORDS

Dynamical system
Intra-step point
Non-linear
Numerical technique
Profile solution
Phase portrait

ARTICLE INFO

Research Article
Doi
10.17678/beuscitech.1633964

Received	February 12,2025
Revised	April 25, 2025
Accepted	June 24, 2025
Year	2025
Volume	15
Issue	1
Pages	80-98

ABSTRACT

One of the numerical techniques used to solve differential equations is the linear multistep method (LMM). A two-step second-derivative intra-point block numerical method of uniform order ten is proposed for solving dynamical systems in ordinary differential equations. The derived two-step method with multi-derivatives effectively addresses the challenges in solving nonlinear dynamical systems - exhibiting phenomena such as multiple steady states, oscillations, and chaos. The inclusion of second derivative in the block method makes sure more information about the ODE is used in generating the solution thereby improving the accuracy of the method. The method is A-stable, making it suitable for solving nonlinear dynamic systems in ordinary differential equations (ODEs). In addition, the method possesses a higher order of accuracy, and the associated error constants are very small. This block method generates numerical solutions that provide solution profiles and phase portraits for the problems considered under various situations of dynamical systems. The results generated from this method underscore its potential as a robust and versatile tool for solving a wide range of practical problems arising in real-life.

1 INTRODUCTION

This article focuses on the development of a numerical method from the class of linear multistep methods (LMM). It is our goal to develop a two-step block hybrid method that improves accuracy and zero-stability while also ensuring convergence by using the derivative of the iterative method in our derivation process – See [1-7]. Our goal is to come close to solving general first-order initial value problems of the form:

$$\frac{dy}{dx} = f\left(x, y\left(x\right)\right), \qquad y\left(x_0\right) = y_0; \; x_0 < x < x_N \tag{1}$$

where y_0 is the given initial condition.

Ordinary differential equations (ODEs) are an essential modeling tools in the fields of science and engineering. That proves its importance in the areas listed. As far as ODEs are concerned, their solutions are more important than their interpretation since it is the only way to understand them. If you employ nonlinear ODEs for any of these areas (engineering, chemistry, physics, economy, biology, and sociology), this holds true. Numerical models of neural networks and climate models, as well as models that incorporate turbulence and data compression, can all be used to prevent the collapse of systems' power by using nonlinear dynamical systems and mixing liquid with low power exhaustion in high-performance information processing, circuits, and other devices [8]. As far as nonlinear problems go, the nonlinear dynamic system is the most important one. This is because it is able to examine the chaotic or disordered problems and uncover the complicated laws that govern them [9, 10,]. It is impossible to solve most of the above-mentioned dynamical problems analytically, so they must be modeled numerically in order to capture their intrinsic laws, and ultimately, their features. The nonlinear dynamic system, on the other hand, is more diversified, and it evolves in a more sophisticated manner based on the prior state. It is very difficult to find analytic solutions in the current situation because of the complexity of the chaotic state. A lot of individuals give up on addressing the precise problem and instead focus on an approach with high approximation accuracy and quick calculation in order to represent the unknowable system state. Another goal is to create numerical integrators that can maintain as much of the underlying dynamics as feasible, even when the step size is large. Methods to solve nonlinear dynamic systems in this direction include a wide variety, including the perturbation technique [11,12], the Runge-Kutta method [13], and the Euler approach [14]. Unfortunately, these approaches have certain benefits in solving specialized systems, but when applied to generic nonlinear dynamic systems, they provide undesirable results, such as reduced accuracy, more complexity, and a huge number of calculations. When it comes to studying nonlinear dynamic systems, can we discover an effective approach with high approximation accuracy and avoid the Runge phenomenon? When it comes to numerically integrating known dynamic systems, LMMs have been widely used in the previous century as well-established mathematical theories [15-18]. Traditional linear multistep approaches to studying dynamics [4, 6, 7, 19, 20, 21] have become more accurate and precise. These studies collectively emphasize the power of spline-based collocation techniques in solving nonlinear evolution equations [22-25]. While not explicitly categorized as LMMs, their methodological foundations share strong parallels with linear multistep frameworks particularly in their treatment of derivative approximations, error control, and stability analysis.

When it comes to solving non-linear dynamical systems, the goal of this article is to develop a new, optimized continuous version of two-step second-derivatives hybrid block technique, utilizing the power series as a basis function, and implement the new method in block form. The second half of this study is concentrated on deriving the suggested approach after establishing the essential numerical features, such as the local truncation error and a stability analysis. The derived block method is used to solve nonlinear dynamic systems to show its efficiency and accuracy in providing the numerical solution to this type of problems.

2 DERIVATION OF THE METHOD

The continuous form of the proposed two-step second derivative method is based on approximating the solution $Y(x)$ of first-order linear and non-linear differential equations by

$$Y(x) = \sum_{j=0}^{2c+i-1} a_j x^j \tag{2}$$

$x = x_n, x_{n+\frac{1}{2}}, x_{n+1}, x_{n+\frac{3}{2}}, x_{n+2}$

where c and i are numbers of collocation points and interpolation points respectively of power series. The unknown coefficients $a_j's$ are obtained from solving a system of (11×11) non-linear equations:

$$\begin{pmatrix} 1 & x_{n+1} & x_{n+1}^2 & x_{n+1}^3 & x_{n+1}^4 & x_{n+1}^5 & x_{n+1}^6 & x_{n+1}^7 & x_{n+1}^8 & x_{n+1}^9 & x_{n+1}^{10} \\ 0 & 1 & 2x_n & 3x_n^2 & 4x_n^3 & 5x_n^4 & 6x_n^5 & 7x_n^6 & 8x_n^7 & 9x_n^8 & 10x_n^9 \\ 0 & 1 & 2x_{n+\frac{1}{2}} & 3x_{n+\frac{1}{2}}^2 & 4x_{n+\frac{1}{2}}^3 & 5x_{n+\frac{1}{2}}^4 & 6x_{n+\frac{1}{2}}^5 & 7x_{n+\frac{1}{2}}^6 & 8x_{n+\frac{1}{2}}^7 & 9x_{n+\frac{1}{2}}^8 & 10x_{n+\frac{1}{2}}^9 \\ 0 & 1 & 2x_{n+1} & 3x_{n+1}^2 & 4x_{n+1}^3 & 5x_{n+1}^4 & 6x_{n+1}^5 & 7x_{n+1}^6 & 8x_{n+1}^7 & 9x_{n+1}^8 & 10x_{n+1}^9 \\ 0 & 1 & 2x_{n+\frac{3}{2}} & 3x_{n+\frac{3}{2}}^2 & 4x_{n+\frac{3}{2}}^3 & 5x_{n+\frac{3}{2}}^4 & 6x_{n+\frac{3}{2}}^5 & 7x_{n+\frac{3}{2}}^6 & 8x_{n+\frac{3}{2}}^7 & 9x_{n+\frac{3}{2}}^8 & 10x_{n+\frac{3}{2}}^9 \\ 0 & 1 & 2x_{n+2} & 3x_{n+2}^2 & 4x_{n+2}^3 & 5x_{n+2}^4 & 6x_{n+2}^5 & 7x_{n+2}^6 & 8x_{n+2}^7 & 9x_{n+2}^8 & 10x_{n+2}^9 \\ 0 & 0 & 2 & 6x_n & 12x_n^2 & 20x_n^3 & 30x_n^4 & 42x_n^5 & 56x_n^6 & 72x_n^7 & 90x_n^8 \\ 0 & 0 & 2 & 6x_{n+\frac{1}{2}} & 12x_{n+\frac{1}{2}}^2 & 20x_{n+\frac{1}{2}}^3 & 30x_{n+\frac{1}{2}}^4 & 42x_{n+\frac{1}{2}}^5 & 56x_{n+\frac{1}{2}}^6 & 72x_{n+\frac{1}{2}}^7 & 90x_{n+\frac{1}{2}}^8 \\ 0 & 0 & 2 & 6x_{n+1} & 12x_{n+1}^2 & 20x_{n+1}^3 & 30x_{n+1}^4 & 42x_{n+1}^5 & 56x_{n+1}^6 & 72x_{n+1}^7 & 90x_{n+1}^8 \\ 0 & 0 & 2 & 6x_{n+\frac{3}{2}} & 12x_{n+\frac{3}{2}}^2 & 20x_{n+\frac{3}{2}}^3 & 30x_{n+\frac{3}{2}}^4 & 42x_{n+\frac{3}{2}}^5 & 56x_{n+\frac{3}{2}}^6 & 72x_{n+\frac{3}{2}}^7 & 90x_{n+\frac{3}{2}}^8 \\ 0 & 0 & 2 & 6x_{n+2} & 12x_{n+2}^2 & 20x_{n+2}^3 & 30x_{n+2}^4 & 42x_{n+2}^5 & 56x_{n+2}^6 & 72x_{n+2}^7 & 90x_{n+2}^8 \end{pmatrix} \begin{pmatrix} a_0 \\ a_1 \\ a_2 \\ a_3 \\ a_4 \\ a_5 \\ a_6 \\ a_7 \\ a_8 \\ a_9 \\ a_{10} \end{pmatrix} = \begin{pmatrix} y_{n+1} \\ f_n \\ f_{n+\frac{1}{2}} \\ f_{n+1} \\ f_{n+\frac{3}{2}} \\ f_{n+2} \\ g_n \\ g_{n+\frac{1}{2}} \\ g_{n+1} \\ g_{n+\frac{3}{2}} \\ g_{n+2} \end{pmatrix}$$

generated from

$$\left.\begin{array}{l} Y(x_{n+1}) = y_{n+1} \\ Y'(x_{n+j}) = f_{n+j} \\ Y''(x_{n+j}) = g_{n+j} \\ \quad j = 0, \frac{1}{2}, 1, \frac{3}{2}, 2 \end{array}\right\} \tag{3}$$

by the use of the matrix inversion method. Substituting $a_j's$ into (2) yields the continuous scheme of our technique in the form:

$$\begin{aligned} y(x) = y_{n+1} &+ h\left(\beta_0(x) f_n + \beta_{\frac{1}{2}}(x) f_{n+\frac{1}{2}} + \beta_1(x) f_{n+1} + \beta_{\frac{3}{2}}(x) f_{n+\frac{3}{2}} + \beta_2(x) f_{n+2}\right) \\ &+ h^2\left(\gamma_0(x) g_n + \gamma_{\frac{1}{2}}(x) g_{n+\frac{1}{2}} + \gamma_1(x) g_{n+1} + \gamma_{\frac{3}{2}}(x) g_{n+\frac{3}{2}} + \gamma_2(x) g_{n+2}\right) \end{aligned} \tag{4}$$

Evaluating (4) at $x = x_n, x_{n+\frac{1}{2}}, x_{n+\frac{3}{2}}, x_{n+2}$ gives the sufficient number of schemes necessary to implement the method as a block:

$$\begin{aligned} y_{n+\frac{1}{2}} = y_{n+1} - \frac{26081}{8709120}hf_n - \frac{122341}{544320}hf_{n+\frac{1}{2}} - \frac{313}{1260}hf_{n+1} - \frac{12091}{544320}hf_{n+\frac{3}{2}} - \frac{14111}{8709120}hf_{n+2} \\ - \frac{893}{2903040}h^2g_n - \frac{6887}{362880}h^2g_{n+\frac{1}{2}} + \frac{47}{1280}h^2g_{n+1} + \frac{1721}{362880}h^2g_{n+\frac{3}{2}} + \frac{103}{580608}h^2g_{n+2} \end{aligned} \quad (5)$$

$$\begin{aligned} y_{n+1} = y_n + \frac{24463}{136080}hf_n + \frac{3308}{8505}hf_{n+\frac{1}{2}} + \frac{104}{315}hf_{n+1} + \frac{788}{8505}hf_{n+\frac{3}{2}} + \frac{1153}{136080}hf_{n+2} \\ + \frac{421}{45360}h^2g_n - \frac{38}{567}h^2g_{n+\frac{1}{2}} - \frac{1}{10}h^2g_{n+1} - \frac{62}{2835}h^2g_{n+\frac{3}{2}} - \frac{43}{45360}h^2g_{n+2} \end{aligned} \quad (6)$$

$$\begin{aligned} y_{n+\frac{3}{2}} = y_{n+1} + \frac{14111}{8709120}hf_n + \frac{12091}{544320}hf_{n+\frac{1}{2}} + \frac{313}{1260}hf_{n+1} + \frac{122341}{544320}hf_{n+\frac{3}{2}} + \frac{26081}{8709120}hf_{n+2} \\ + \frac{103}{580608}h^2g_n + \frac{1721}{362880}h^2g_{n+\frac{1}{2}} + \frac{47}{1280}h^2g_{n+1} - \frac{6887}{362880}h^2g_{n+\frac{3}{2}} - \frac{893}{2903040}h^2g_{n+2} \end{aligned} \quad (7)$$

$$\begin{aligned} y_{n+2} = y_{n+1} + \frac{1153}{136080}hf_n + \frac{788}{8505}hf_{n+\frac{1}{2}} + \frac{104}{315}hf_{n+1} + \frac{3308}{8505}hf_{n+\frac{3}{2}} + \frac{24463}{136080}hf_{n+2} \\ + \frac{43}{45360}h^2g_n + \frac{62}{2835}h^2g_{n+\frac{1}{2}} + \frac{1}{10}h^2g_{n+1} + \frac{38}{567}h^2g_{n+\frac{3}{2}} - \frac{421}{45360}h^2g_{n+2} \end{aligned} \quad (8)$$

3 ANALYSIS OF THE METHOD

3.1 Local Truncation Error

Given that $y(x)$ is a sufficiently differentiable function, following [6], the derived two-step second derivative block hybrid method can be written as a linear operator as

$$L[y(x);h] = \sum_{j=0}^{k} \left(\alpha_j y_{n+j} - h\{\beta_j f_{n+j}\} - h^2\{\gamma_j g_{n+j}\} \right) \quad (9)$$

We can expand the terms in (9) as a Taylor series about the point x to come up with the expression

$$L[y(x);h] = e_0 y(x) + e_1 hy(x) + \ldots + e_p h^p y(x) + \ldots \quad (10)$$

where the constant $e_p, p = 0,1,\ldots$ are given as follows

$$\left.\begin{aligned}
e_0 &= \sum_{j=0}^{k} \alpha_j \\
e_1 &= \sum_{j=1}^{k} j\alpha_j - \left(\sum_{j=0}^{k} \beta_j + \beta_v\right) \\
e_2 &= \frac{1}{2!}\sum_{j=1}^{k} (j)^2\alpha_j - \left(\sum_{j=1}^{k} j\beta_j + v\beta_v\right) - \left(\sum_{j=0}^{k} \gamma_j + \gamma_v\right) \\
&\vdots \\
e_p &= \frac{1}{p!}\sum_{j=1}^{k} (j)^p\, \alpha_j - \frac{1}{(p-1)!}\left(\sum_{j=1}^{k} j^{p-1}\, \beta_j + j^{p-1}\gamma_j\right) - \frac{1}{(p-2)!}\left(\sum_{j=1}^{k} j^{p-2}\gamma_j + j^{p-2}\gamma_j\right)
\end{aligned}\right\} \tag{11}$$

v is the set of the the grid points, γ_v is the cofficients the main points in second derivatives of the methods, β_v is the cofficients the main points in first derivatives of the methods.

The numerical method is said to be of order *p* if $e_0 = e_1 = \ldots = e_p = 0$ and $e_{p+1} \neq 0$. By applying Eq. (11) to each methods in the block, the block method is of uniform order $(10,10,10,10)^T$ and the error constant is obtained as $e_{11} = \left(-\frac{89}{643778150400}, \frac{1}{1005903360}, \frac{89}{643778150400}, \frac{1}{1005903360}\right)^T$

3.2 Stability Analysis

In order to characterize the method for stability, we rewrite the schemes (5) to (8) as a matrix difference equation as follows:

$$P^{(1)}Y_w = P^{(0)}Y_{w-1} + h\left[Q^{(0)}F_{w-1} + Q^{(1)}F_w\right] + h^2\left[R^{(0)}G_{w-1} + R^{(1)}G_w\right] \tag{12}$$

where

$$\left.\begin{array}{l} Y_w = \left(y_{n+\frac{1}{2}}, y_{n+1}, y_{n+\frac{3}{2}}, y_{n+2} \right)^T \\ Y_{w-1} = \left(y_{n-\frac{1}{2}}, y_{n-1}, y_{n-\frac{3}{2}}, y_n \right)^T \\ F_w = \left(f_{n+\frac{1}{2}}, f_{n+1}, f_{n+\frac{3}{2}}, f_{n+2} \right)^T \\ F_{w-1} = \left(f_{n-\frac{1}{2}}, f_{n-1}, f_{n-\frac{3}{2}}, f_n \right)^T \\ G_w = \left(g_{n+\frac{1}{2}}, g_{n+1}, g_{n+\frac{3}{2}}, g_{n+2} \right)^T \\ G_{w-1} = \left(g_{n-\frac{1}{2}}, g_{n-1}, g_{n-\frac{3}{2}}, g_n \right)^T \end{array}\right\}$$

and $P^{(1)}, P^{(0)}, Q^{(1)}, Q^{(0)}, R^{(1)}$ and $R^{(0)}$ are matrices whose entries are given by the coefficients of the block method.

Definition 3.1. A block linear multistep method is said to be zero stable if the roots (λ_k) of the difference equation in (12) as $h \to 0$ is $|\lambda_k| \le 1,\ k = 1, \ldots 4$ and the multiplicity of the roots $|\lambda_k| = 1$ is not greater one [7].

Definition 3.2. (Akinfenwa *et al.*,[3]). A block method is A-stable if subjected to the test equation $y^{(n)} = \lambda^n y$ to yield

$Y_w = \sigma(z) Y_{w-1},\ z = \lambda h$ and the matrix

$$\sigma(z) = -\left(P^{(1)} - zQ^{(1)} - z^2 R^{(1)}\right)^{-1} \left(P^{(0)} + zQ^{(0)} + z^2 R^{(0)}\right) \tag{13}$$

produces the stability function $R(z) : \mathbb{C} \to \mathbb{C}$ whose the domain $S = \{ z \in \mathbb{C} : R(z) \le 1 \}$ is contained in the left-half complex plane.

The stability function of the method is obtained as:

$$R(z) = -\frac{A(z)}{2903040 \times B(z)} \tag{14}$$

where

$$A(z)=\begin{pmatrix}33094656z^8+44505048z^7-3644501112z^6-11422739963z^5-59334135598z^4\\-107784037251z^3-478403901952z^2-424689652800z-526727577600\end{pmatrix}$$

and

$$B(z)=\left(237z^8+948z^7-3165z^6-12807z^5+29147z^4+80745z^3-138775z^2-181440z+181440\right)$$

which yields the stability region below:

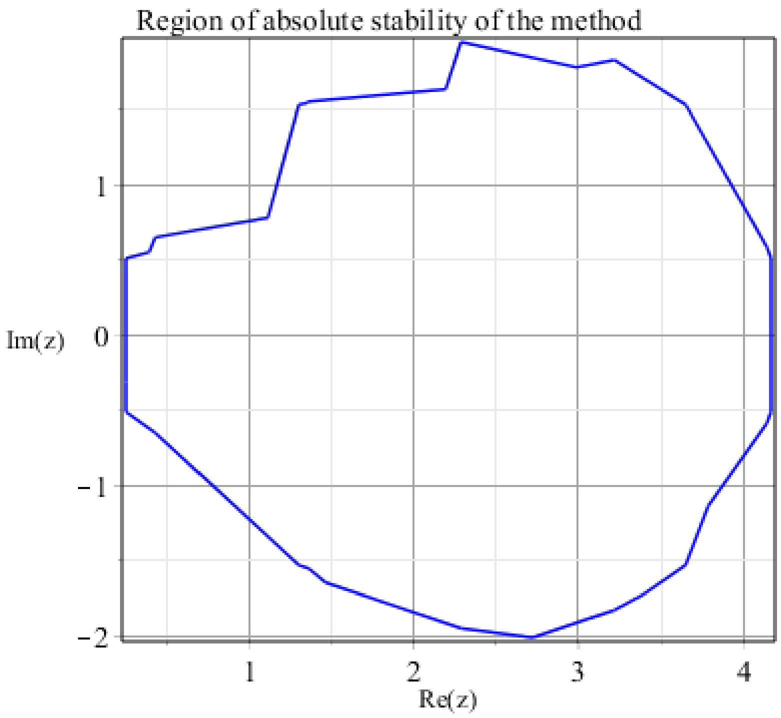

Figure 1. *Stability Domain of the block method which is A stable by Definition 3.2.*

3.3 Convergence of the Method

Consistency and zero stability are both required and sufficient for a linear multistep technique to reach convergence in the spirit of Lambert [1]. As a result, we infer that our technique is convergent since it has an order of accuracy greater than 1 (which implies consistency) and zero-stable as the roots of the first characteristic polynomial:

$$\rho(\lambda)=\left|\lambda P^{(1)}-P^{(0)}\right|=\left|\lambda^3(\lambda+1)\right|=0\Rightarrow|\lambda_k|=0,0,0,1.$$

4 NUMERICAL EXPERIMENTATION

First-order dynamical systems with applications in population dynamics, chemical equations, and vibration theory are implemented at this point. The resultant iterative techniques are discretized into the following form:

$$y'_{n+j} = f\left(x_{n+j}, y_{n+j}\right), \quad y''_{n+j} = g\left(x'_{n+j}, f_{n+j}\right), \quad j = 0, \frac{1}{2}, 1, \frac{3}{2}, 2 \tag{15}$$

and treated as a block which requires no predictors. Using the known initial condition, $y(x_n)$ for $n = 0,1,\ldots,N-2$, the first order initial value problems are solved in the N non-overlapping block points $[x_0, x_2],\ldots,[x_{N-2}, x_N]$, with the step size defined in the usual way as $h = x_{n+1} - x_n$.

4.1 One Dimensional Non-Linear Equations

Problem 1: consider the non-linear equation

$$y' = y^2 - xy, \quad y(0) = \frac{1}{2},$$

Where $0 \leq x \leq 5$

with the exact solution: $y(x) = -\dfrac{2e^{-\frac{1}{2}x^2}}{\sqrt{2\pi}erf\left(\frac{x}{\sqrt{2}}\right) - 4}$

The solution of problem (1) exists and is unique in some open interval around $f(x,y) = y^2 - xy$ and its partial derivative with respect to $\frac{\partial y}{\partial f} = 2y - x$, are continuous in a neighborhood of the point $\left(0, \frac{1}{2}\right)$

The exact and numerical solutions of Problem 1 are shown in Table 1.

Table 1. *Numerical Results of Problem 1 h = 0.125.*

x	Exact solution	Numerical solution	Absolute Error
0.5	0.580561504994342592870	0.580561504994337359380	5.23×10^{-15}
1.0	0.53001012553517410973	0.53001012553517913111	5.021×10^{-15}
1.5	0.35514264136413282107	0.35514264136411971949	1.31×10^{-14}
2.0	0.16838778751589774834	0.16838778751590368185	5.93×10^{-15}
2.5	0.05764101711735069568	0.05764101711734908072	1.62×10^{-15}
3.0	0.01481062184214964518	0.01481062184214924078	4.04×10^{-16}
3.5	0.00292731423971718403	0.00292731423971730883	1.25×10^{-16}
4.0	0.00044922099358723716	0.00044922099358725387	1.67×10^{-17}
4.5	0.00005365688894804310	0.00005365688894803547	7.63×10^{-18}
5.0	0.00000499092024129121	0.00000499092024128824	2.97×10^{-18}

Problem 2: consider the Riccati equation

$$y' = -y^2 + 2y + 1, \quad y(0) = 0,$$

where $0 \le x \le 10$.

with the exact solution: $y(x) = 1 + \sqrt{2}\tanh\left[\sqrt{2}x + \frac{1}{2}\log\left(\frac{\sqrt{2}-1}{\sqrt{2}+1}\right)\right]$

The exact and numerical solutions of Problem 2 are shown in Table 2.

Table 2. *Numerical Results of Problem 2 h=0.1.*

x	Exact solution	Numerical solution	Absolute Error in the new method	Error in [21] ***h = 0.05***
1	1.6894983915943829868601 90	1.689498391594262702400997411	1.202×10^{-13}	1.418×10^{-11}
2	2.357771653291484669754109 8	2.357771653291480161441488169	4.508×10^{-15}	7.234×10^{-13}
3	2.410813685936601635766048 6	2.410813685936601474683390076	1.611×10^{-16}	1.163×10^{-13}
4	2.414012382605692442433990 4	2.414012382605692432450850306	9.983×10^{-18}	2.132×10^{-14}
5	2.414201670696914256989920 7	2.414201670696914256292842259	6.971×10^{-19}	2.664×10^{-15}
6	2.414212859503916070906863 4	2.414212859503916070859043211	4.782×10^{-20}	4.441×10^{-16}
7	2.414213520829477776448884 0	2.414213520829477776445665405	3.219×10^{-21}	4.441×10^{-16}
8	2.414213559917628501101166 6	2.414213559917628501100953252	2.134×10^{-22}	4.441×10^{-16}
9	2.414213562227962865223392 2	2.414213562227962865223378235	1.399×10^{-23}	4.441×10^{-16}
10	2.414213562364516902740712 4	2.414213562364516902740711570	9.076×10^{-25}	4.441×10^{-16}

4.2 Two Dimensional Non-Linear Equations

Problem 3: consider the following vector field

$$y_1' = (\delta y_1 + y_2)(y_1^2 - 1), \quad y_1(0) = \frac{1}{100}$$
$$y_2' = (-y_1 + \delta y_2)(y_2^2 - 1), \quad y_2(0) = \frac{1}{50}$$

where $0 \le t \le 1$.

The solution profile and 2D phase portraits of Problem 3 are shown presented in Figs 2a and 2b for the case $\delta = -0.2$

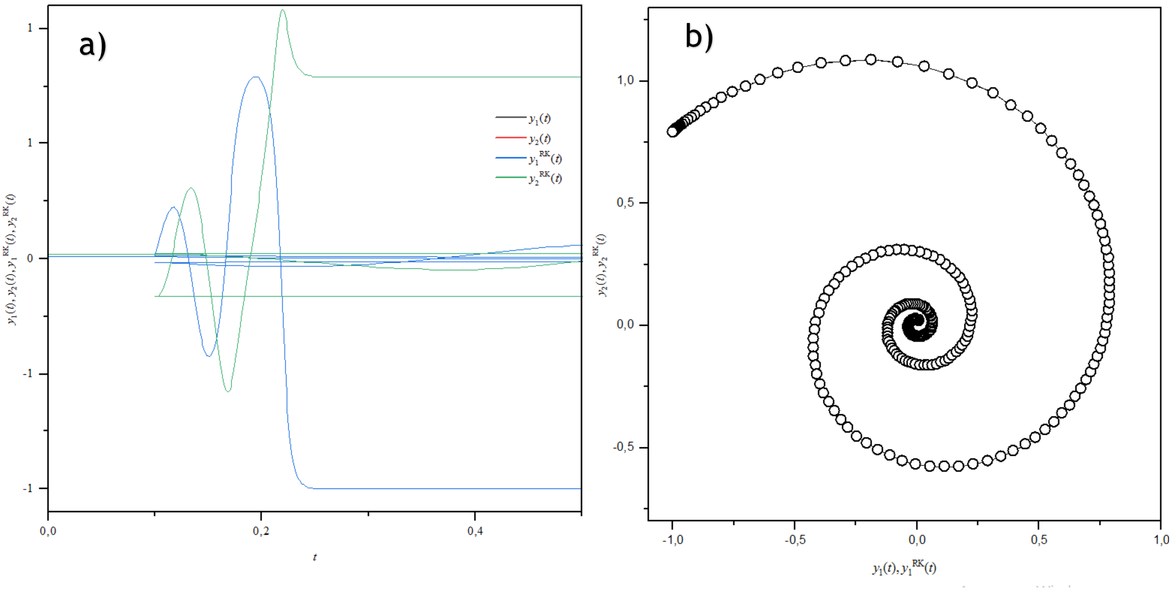

***Figure 2**. **a)** Solution profile of problem 3 with h=0.1, **b)** Phase portrait of Problem 3 with h=0.1.*

4.3 Examples from Chaos Theory

Problem 4: Consider the Lorenz system given by

$$\begin{aligned} y_1' &= a(y_2 - y_1), & y_1(0) &= 1 \\ y_2' &= -y_1 y_3 + b y_1 - y_2, & y_2(0) &= 5 \\ y_3' &= y_1 y_2 - c y_3 & y_3(0) &= 10 \end{aligned} \ ,$$

where $0 \le t \le 30$.

The parameters are given as $a = 10, b = 28, c = \frac{8}{3}$. The solution profile and 3D phase portrait of problem 4 are shown in Figs 3a and 3b with h = 0.1.

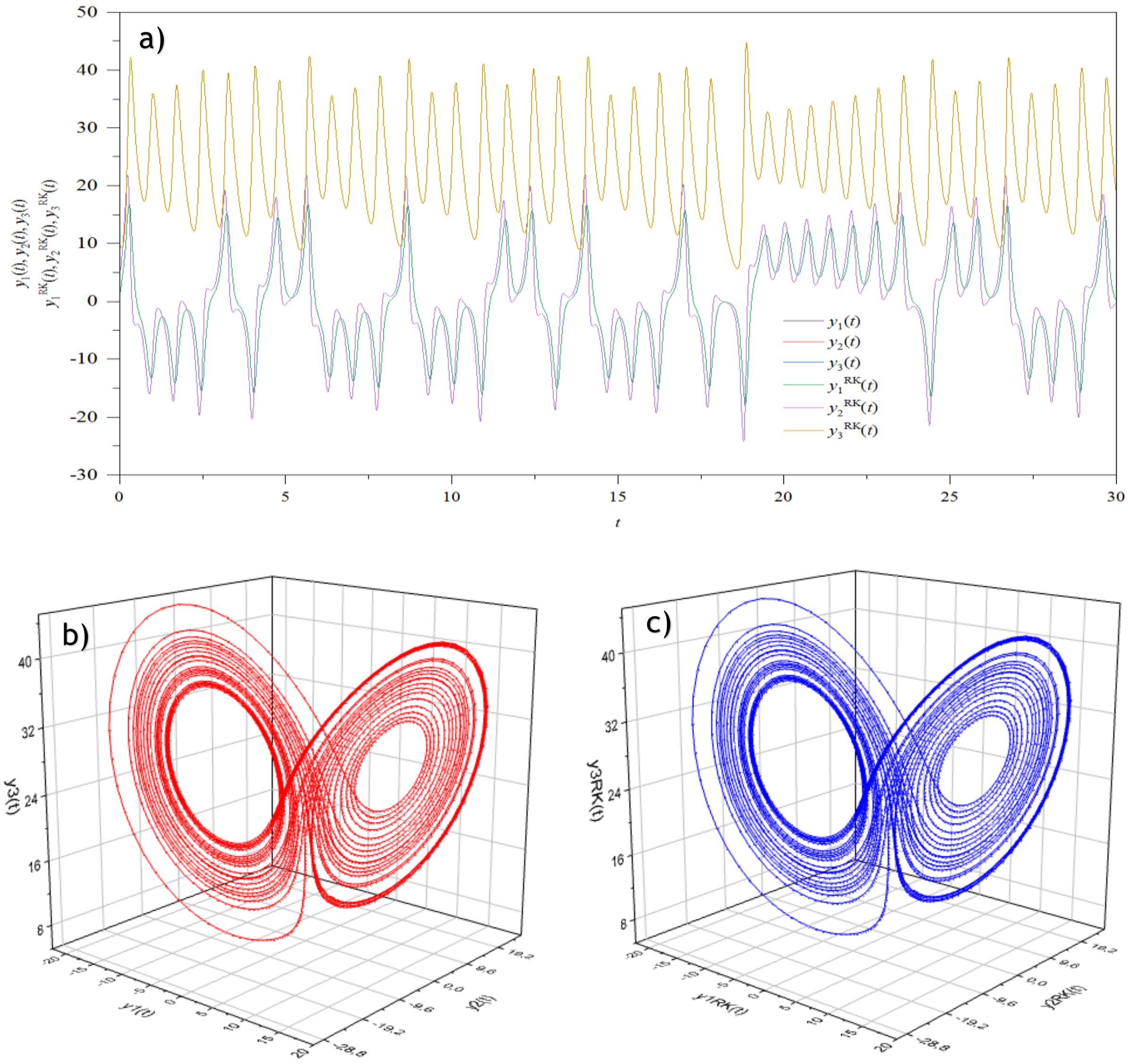

***Figure 3**. **a)** Solution profile of problem 4 with h=0.1, **b)** Phase portrait of problem 4 (new method), **c)** Phase portrait of problem 4 (R-K 5).*

Problem 5: Consider the Arneodo-Coullet given by

$$
\begin{aligned}
y_1' &= y_2, & y_1(0) &= 0.21 \\
y_2' &= y_3, & y_2(0) &= 0.22 \\
y_3' &= ay_1 - by_2 - y_3 - y_1^3, & y_3(0) &= 0.61
\end{aligned}
$$

where $0 \le t \le 100$.

The parameters are given as $a = 5, b = 3.8$.The solution profile and 3D phase portrait of problem 5 are shown in

Figs 4a and 4b with h = 0.0025.

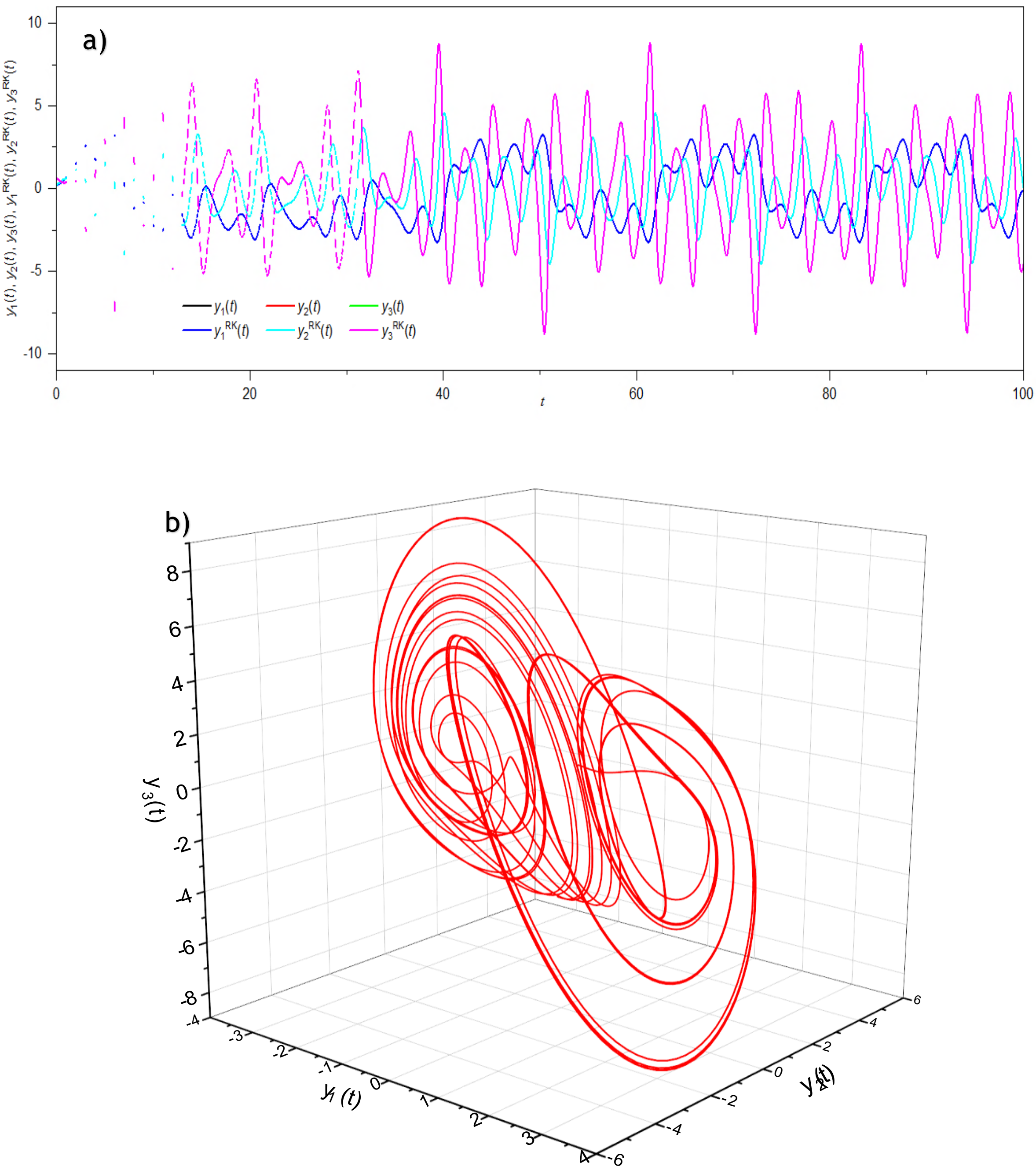

***Figure 4. a)** Time series solution for the Arneodo-Coullet equation with h=0.025*
***b)** Phase Portrait for the Arneodo-Coullet equation with h=0.025.*

4.4 Examples from Population Dynamics

Problem 6: Consider the predator -prey model with a Beddington-DeAnglis functional response

$$y_1' = y_1(1-y_1) - \frac{\alpha y_1 y_2}{1+\beta y_1 + \mu y_2}, \quad y_1(0) = 0.15$$

$$y_2' = \frac{E y_1 y_2}{1+\beta y_1 + \mu y_2} - D y_2, \quad y_2(0) = 0.5$$

where $0 \leq t \leq 200$.

In this example, the parameter used are $\alpha = 1, \beta = 1.3, E = 4, D = 0.4$. The solution profile and phase portraits of problem 6 are shown in Figs 5a, and 5b with h = 0.1 at various values of t.

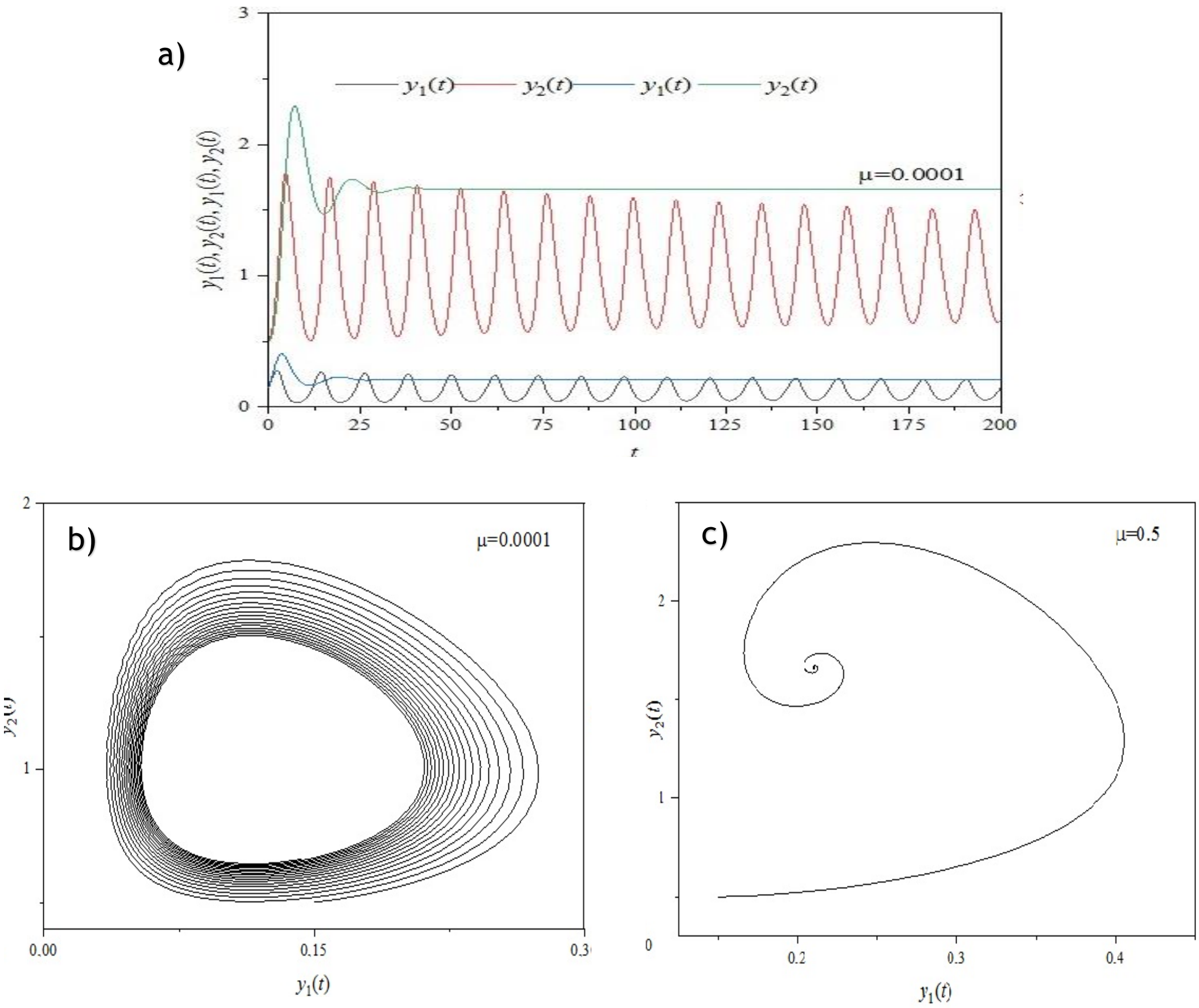

***Figure 5**. **a)** Time series solution for the Prey-predator model with h=0.1*
***b)** Phase portraits for the Prey-predator model with h=0.1 **c)** Phase portraits for the Prey-predator model with h=0.5.*

Problem 7: We also consider the Kermack-McKendrick model. SIR model that tracks the rise and fall in the number of infected patients observed in epidemics. If the population is divided into three classes: susceptible - y_1, infectious - y_2, and those removed due to immunity - y_3, the governing equations are:

$$
\begin{aligned}
y_1' &= by_1 - vy_1y_2 && y_1(0) = 700 \\
y_2' &= vy_1y_3 - cy_2, && y_2(0) = 1 \\
y_3' &= cy_2, && y_3(0) = 0
\end{aligned}
$$

where $0 \leq t \leq 1000$.

where *v* is the infection rate, *b* is the birth rate and *c* is the immunity rate. The simulation of the SIR model with $b = 0.02,\ v = 0.0005,\ c = 0.2$ is given in the figs below.

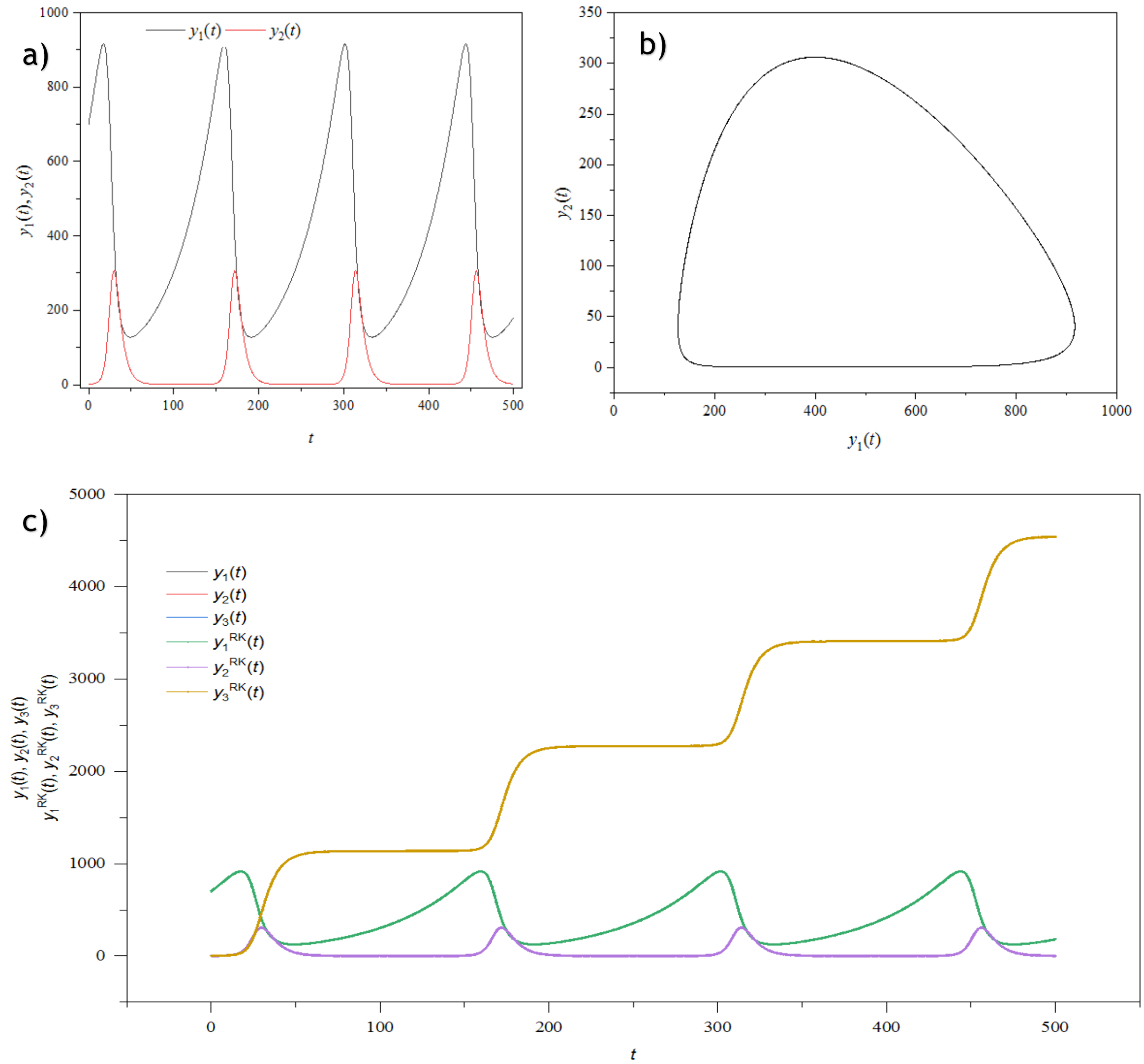

***Figure 6**. **a)** Time series solution of the SIR using h=0.1 **b)** Phase portraits of the SIR model when h=0.1 **c)** Time series solution of the SIR using h=0.1.*

5 DISCUSSION OF RESULTS

What follows is the analysis of the numerical results obtained from solving the nonlinear dynamical systems using the newly derived linear multistep method. Table 1 shows the numerical results for the nonlinear equation in Problem 1 for h = 0.125. The absolute errors indicate that the method is in agreement with the exact solution with relatively small errors. Similarly, in Table 2, we have the results of the Riccati equation in Problem 2. The problem is solved using the step size h = 0.1 and the error analysis, as shown in the table, reveals that the new method is effective in solving the nonlinear problem better than the method in [21] (even with its smaller step size of h = 0.05)

However, problems 3-7 are nonlinear dynamical systems, which have no known analytical solutions. In this regard, our method is validated by solving the problems with the known Runge-Kutta method of order 5 embedded in Maple 2015, and the results show that both methods are in agreement. Figure 2a shows the behaviour of the two-dimensional nonlinear equations in Problem 3, while Figure 2b is the phase portrait of the problem. Figure 2a and Figure 2b agrees with those found in literature. Also, figure 3a is the behavioural solution of the Lorenz system in problem 4, while figures 3b and 3c show the phase portraits for our method and the Runge-Kutta method, respectively. Similarly, the profile solution of the Arneodo-Coullet equation in problem 5 is displayed in figure 4a, while figure 4b shows its phase portraits. And figures 5a and 5b give the profile solution and the portrait phase of the predator-prey in problem 6. Figure 5a agrees with those found in literature. Lastly, the solution to the Kermack-McKendrick SIR model in problem 7 is given in Figure 6.

6 CONCLUSION

We have proposed a novel numerical technique with intra-step points for the solution of non-linear dynamical systems. The inclusion of second derivtaive in the implementation of the block hybrid method makes sure more information (multiderivative of the problems) about the ODE is used in generating the solution thereby improving the accuaracy of the method. Having discussed the convergence analysis, we found the method to be of order 10. The numerical solutions show the graphical simulation of the proposed methods displaying the profile solutions and their corresponding phase portraits are shown in Figures 2-6. As we mentioned, application problems considered do not have known analytical solutions hence we validated our results with the Runge-Kutta method (RK5). Hence, this method is recommended for real-life problems involving nonlinear dynamical systems. In future research, we intend to explore the method on dynamical systems in partial differential equations.

Conflict of Interest

There is no conflict of interest between the authors.

Authors Contributions

This work was carried out in collaboration between all the authors. J. Garba conceived the idea and designed the study. He performed the Mathematical analysis of derivation and implementation of the method, and wrote the first draft of the manuscript. O. Oyelami managed the literature searches, performed computational analysis that produced the graphs and gave insightful comments on all sections of the draft manuscript. U. Mohammed provided adequate guidelines and thorough supervision of the manuscript.

Statement of Research and Publication Ethics

The study is complied with research and publication ethics.

Artificial Intelligence (AI) Contribution Statement

This manuscript was entirely written, edited, analyzed, and prepared without the assistance of any artificial intelligence (AI) tools. All content, including text, data analysis, and figures, was solely generated by the authors.

REFERENCES

[1] J. D. Lambert, Numerical Methods for Ordinary Differential Systems, The Initial Value Problem. Chichester, UK: Wiley, 1991.

[2] P. Onumanyi, D. O. Awoyemi, S. N. Jator, and U. W. Sirisena, “New linear multistep methods with continuous coefficients for first order initial value problems,” *J. Nig. Math. Soc.*, vol. 13, no. 1, pp. 37–51, 1994.

[3] O. A. Akinfenwa, S. N. Jator, and N. M. Yao, “A self-starting block Adams methods for solving stiff ODEs,” in Proc. *14th IEEE Int. Conf. Comput. Sci. Eng.*, 2011, p. 156.

[4] D. G. Yakubu, G. M. Kumlen, and S. Markus, “Second derivative Runge-Kutta collocation methods based on Lobatto nodes for stiff systems,” *J. Mod. Methods Numer. Math.*, vol. 8, no. 2, pp. 118–138, 2017.

[5] K. Mehdizadeh, N. Nasehi, and G. Hojjati, “A class of second derivative multistep methods for stiff systems,” *Acta Univ. Apulensis*, vol. 30, no. 1, pp. 171–188, 2012.

[6] J. Garba and U. Mohammed, “Derivation of a new one-step numerical integrator with three intra-step points for solving first order ordinary differential equations,” *Niger. J. Math. Appl.*, vol. 30, no. 1, pp. 155–172, 2020.

[7] U. Mohammed, J. Garba, and M. E. Semenov, “One-step second derivative block intra-step method for stiff system of ordinary differential equations,” *J. Niger. Math. Soc.*, vol. 40, no. 1, pp. 47–57, 2021.

[8] K. M. Ibrahim, R. K. Jamal, and F. H. Ali, “Chaotic behaviour of the Rossler model and its analysis by using bifurcations of limit cycles and chaotic attractors,” *J. Phys.: Conf. Ser.*, 2018, doi:10.1088/1742-6596/1003/1/012099.

[9] G. Chen and J. L. Moiola, “An overview of bifurcation, chaos and nonlinear dynamics in control systems,” *J. Franklin Inst.*, vol. 331, no. 6, pp. 819–858, 1994.

[10] A. Farshidianfar and A. Saghafi, “Global bifurcation and chaos analysis in nonlinear vibration of spur gear systems,” *Nonlinear Dyn.*, vol. 75, no. 4, pp. 783–806, 2014.

[11] L. V. Stepanova and S. A. Igonin, “Perturbation method for solving the nonlinear eigenvalue problem arising from fatigue crack growth problem in a damaged medium,” *Appl. Math. Model.*, vol. 38, no. 14, pp. 3436–3455, 2014.

[12] M. Jiya, “Application of homotopy perturbation method (HPM) for the solution of non-linear differential equations,” *Pac. J. Sci. Technol.*, vol. 11, no. 2, pp. 268–272, 2010.

[13] J. Giné, J. Llibre, K. Wu, and X. Zhang, “Averaging methods of arbitrary order periodic solutions and integrability,” *J. Differ. Equations*, vol. 260, no. 5, pp. 4130–4156, 2016.

[14] H. de la Cruz, R. J. Biscay, J. C. Jimenez, and F. Carbonell, “Local linearization-Runge-Kutta methods: a class of A-stable explicit integrators for dynamical systems,” *Math. Comput. Model.*, vol. 57, nos. 3–4, pp. 720–740, 2013.

[15] H. H. Goldstine, *A History of Numerical Analysis from the 16th through the 19th Century*. New York, NY, USA: Springer, 2012.

[16] K. Atkinson, W. Han, and D. E. Stewart, Numerical Solution of Ordinary Differential Equations. *Pure Appl. Math.*, vol. 108, 2011.

[17] G. G. Dahlquist, "A special stability problem for linear multistep methods," *BIT*, vol. 3, no. 1, pp. 27–43, 1963.

[18] P. Henrici, *Discrete Variable Methods in Ordinary Differential Equations*. Hoboken, NJ, USA: Wiley, 1962.

[19] R. T. Keller and D. U. Qiang, "Discovery of dynamics using linear multistep methods," *SIAM*, vol. 59, no. 1, pp. 429–455, 2021.

[20] M. Musa and M. A. Unwala, "Extended 3-point super class of block backward differentiation formula for solving stiff initial value problems," *Abacus (Math. Sci. Ser.)*, vol. 44, no. 1, pp. 584–591, 2019.

[21] B. S. H. Kashkari and M. I. Syam, "Optimization of one step block method with three hybrid points for solving first-order ordinary differential equations," *Results Phys.*, vol. 12, pp. 592-596, 2019.

[22] S. B. G. Karakoç, A. Saha, and D. Y. Sucu, "A collocation algorithm based on septic B-splines and bifurcation of traveling waves for Sawada Kotera equation," *Math. Comput. Simul.*, vol. 203, pp. 12–27, 2023.

[23] R. Jiwari and S. A. Pandey, "Collocation algorithm based on septic B-splines and bifurcation of traveling waves for Sawada-Kotera equation," *Math. Comput. Simul.*, vol. 203, no. 1, pp. 12–27, 2023.

[24] A. Kiliçman, A. E. Ismail, and Z. Ismail, "A novel scheme based on collocation finite element method to generalised Oskolkov equation," *J. Sci. Arts*, vol. 25, no. 4, pp. 895–908, 2021.

[25] B. M. Saka and F. Erdogan, "A septic B-spline collocation method for solving the generalized equal width wave equation," *Kuwait J. Sci.*, vol. 43, no. 1, pp. 20–31, 2016.

BİTLİS EREN UNIVERSITY
JOURNAL OF SCIENCE AND TECHNOLOGY

E-ISSN: 2146-7706

THE EFFECTS OF TWISTED STRIPS WITH DIFFERENT LENGTH ON HEAT TRANSFER AND PRESSURE DROP IN CONCENTRIC HEAT EXCHANGER

Zeki ARGUNHAN [1,*], Cengiz YILDIZ [2], Emin EL [3]

[1] *Bitlis Eren University, Department of Mechanical Engineering, Türkiye, zargunhan@beu.edu.tr*
* *Corresponding author*
[2] *Fırat University, Department of Mechanical Engineering, Türkiye, cyildiz@firat.edu.tr*
[3] *Bitlis Eren University, Department of Mechanical Engineering, Türkiye, eel@beu.edu.tr*

KEYWORDS

Twisted Strips
Concentric Heat Exchanger
Heat Transfer
Pressure Drop

ARTICLE INFO

Research Article
Doi
10.17678/beuscitech.1591461

Received	November 26, 2024
Revised	June 30, 2025
Accepted	June 30,2025
Year	2025
Volume	15
Issue	1
Pages	99-111

ABSTRACT

This study investigated the use of twisted strips as passive turbulators to improve heat transfer efficiency in concentric heat exchangers. In the experiments, four different lengths of twisted strips were designed (l = 0.25 m, 0.5 m, 0.75 m, and 1 m) and their performance was evaluated in a system with air and water fluids. The effects of twisted strips on heat transfer and pressure drops are investigated in both parallel and countercurrent flow patterns, and the results are analyzed in terms of Nusselt and Reynolds numbers. The results indicated that tubes using twisted strips achieved significant increases in the heat transfer coefficient compared to straight tubes. The highest increase in heat transfer performance reached 78% when the length of the twisted strip was l/L=1. The Nusselt number increased by a factor of 1.2 to 1.8, depending on the length of the twisted strips. The shortest strip length (l/L=0.25) resulted in the lowest heat transfer performance. However, these improvements were accompanied by significant increases in pressure drop; for full-length strips, the pressure drop increased by nearly 100%. The pressure drop increased slightly as the Reynolds number increased. The swirling flow generated by the twisted ribbons plays an important role in increasing the heat transfer. Despite the increases in pressure drops, the energy loss is negligible compared to the heat transfer gain achieved. In conclusion, the length ratio of the twisted strips significantly affects the thermal performance of the heat exchanger while increasing the pressure losses. These findings demonstrate the effectiveness of twisted strips as passive turbulators.

1 INTRODUCTION

Heat exchangers are extensively utilized in heating and cooling systems. Enhancing heat transfer efficiency can facilitate the design of smaller, more economical, and energy-efficient heat exchangers.

Heat transfer enhancement can be achieved through various augmentation strategies, which are generally classified into three primary categories: (i) Passive Methods, (ii) Active Methods, and (iii) Combined Methods [1]. Passive methods typically involve alterations to the surface or geometry of the flow passage, such as using inserts or additional devices [2]. Conversely, active methods are more intricate, requiring external energy input to achieve the intended flow modifications and improve heat transfer rates. Combined methods integrate multiple approaches to create a synergistic improvement in performance.

Passive techniques, particularly those employing inserts in the flow passage, offer advantages over active techniques due to their straightforward and cost-effective manufacturing processes, and their ease of application in existing heat exchangers. Consequently, extensive research has been conducted on passive methods and their fluid flow dynamics. Swirl flow generators are a commonly employed solution to enhance heat transfer rates in such setups [3].

Swirl flow devices, recognized as passive heat transfer enhancement methods, generate a rotational flow along an axis parallel to the main flow direction, thereby increasing heat transfer performance [4]. Research on swirling flows in pipes is typically divided into two categories: continuous swirl and decaying swirl. Investigations have explored the heat transfer and pressure drop behavior of fluids in tubes with continuous swirl flows [2], [5], while studies on decaying swirl flows have focused on understanding their thermal transfer characteristics [6], [7].

Regarding compound techniques, R. Babu et al. [8] carried out an extensive review of both experimental and numerical studies addressing passive compound heat transfer enhancement methods. Notable examples discussed in the review included setups such as helical ribbed tubes combined with double twisted tape inserts, dimpled tubes integrated with swirl generators in the form of twisted tapes, and irregular wire coils used in conjunction with twisted tapes. These compound approaches were found to deliver significantly higher heat transfer coefficients compared to the use of a single enhancement strategy alone.

R. Mashayekhi et al. [9] investigated the thermo-hydraulic performance of a bent elliptical pipe integrated with bent tape inserts, focusing on factors such as geometric configurations, Reynolds numbers, and varying slopes. The findings demonstrated that the Nusselt numbers and friction factors were higher compared to those observed in smooth elliptical pipes. Similarly, B. Kumar et al. [10] explored the influence of perforated and V-cut twisted tapes, showing that modifications in twist ratios and V-cut dimensions led to increases in both the Nusselt number and the friction factor.

Y. Hong et al. [11] proposed a synergistic design involving a spiral corrugated pipe with multiple twisted bands for liquid-gas heat exchange. This configuration enhanced turbulent heat transfer and flow performance, leading to higher Nusselt numbers. Likewise, M. M. K. Bhuiya et al. [12] explored perforated triple-twisted tape inserts with varying porosities, finding that reduced porosity improved heat transfer and thermal efficiency. B. K. Dandoutiya and A. Kumar [13] studied the use of W-cut twisted belts in a double-pipe heat exchanger, showing that turbulence and flow separation induced by the inserts enhanced heat transfer rates. R. Behcet et al. [14] placed a propeller-type turbulator at the inlet of the inner tube to increase heat transfer in parallel-flow heat exchangers and experimentally investigated the effect of this structure on heat transfer and friction losses. In the experiments, they used air as hot fluid and water as cold fluid and made measurements at Reynolds numbers between 8000 and 24000. The use of a turbulator increased the heat transfer by 25.5%-50.3%, while increasing the friction losses by about five times. Exergy analysis showed that the exergy losses were 15% lower in the turbulator system compared to the empty pipe. As a result, it was determined that the use of turbulators both improves thermal performance and provides thermodynamic advantages. Z. Argunhan and C. Yıldız [15] experimentally investigated the effects of rotary generators with different numbers of holes on heat transfer and pressure drop in a nested tube heat exchanger. In the experiments, rotary generators with a 55° blade angle and one to four circular holes were installed at the start of the inner tube, and it was found that the four-hole generator increased heat transfer by up to 83% when using air and water.

This study investigates passive heat transfer enhancement using twisted metallic strips as turbulators in the inner pipe of a concentric double-pipe heat exchanger. The effects of various tape lengths (l/L = 0.25, 0.5, 0.75, 1) on thermal performance and pressure drop were experimentally examined under both parallel and counterflow configurations. The results revealed that twisted tapes significantly enhance heat transfer efficiency. A comprehensive evaluation of the heat gain-to-pressure loss ratio enabled the identification of optimal tape length and Reynolds number range. The study contributes to the development of energy-efficient designs for compact heat exchangers by promoting turbulence-induced thermal enhancement.

2 METHOD

The heat transferred from hot fluid to cold fluid in the concentric type heat exchangers [16];

$$Q = m_h Cp_h (T_{hi} - T_{ho}) \quad \textbf{(1)}$$

The heat received by the cold water is

$$Q = m_c Cp_c (T_{ci} - T_{co}) \quad \textbf{(2)}$$

The heat transfer for hot and cold fluids can be expressed using the following equations:

$$Q = m_h Cp_h (T_{hi} - T_{ho}) = m_c Cp_c (T_{ci} - T_{co}) \quad \textbf{(3)}$$

$$Q = h_h A (T_m - T_w) \quad \textbf{(4)}$$

The average fluid temperature, T_m, was computed as the arithmetic mean of the inlet and outlet temperatures of the fluid. This value was utilized to represent the fluid's physical properties at the average temperature. The wall temperature, T_w, was calculated as the arithmetic mean of the measurements taken by thermocouples affixed to the pipe wall.

The theoretical Nusselt number for the pipes was calculated using the Dittus-Boelter correlation, as provided in "Eq. 5" [17].

$$Nu = 0.023Re^{0.8}Pr^{0.4} \quad \textbf{(5)}$$

Additionally, the Nusselt number, representing the air-side average heat transfer coefficient, is expressed as

$$Nu = \frac{hD_e}{k} \quad \textbf{(6)}$$

$$Re = \frac{VD_e}{\nu} \quad \textbf{(7)}$$

$$D_e = \frac{4A_c}{P} \quad \textbf{(8)}$$

3 EXPERIMENTAL STUDY

The experimental setup used in the study is given in Figure 1a and the schematic representation of the system is in Figure 1b. A variety of twisted turbulators were designed and evaluated during the experiments. These turbulators were installed at the inlet section of the inner pipe within the concentric heat exchanger.

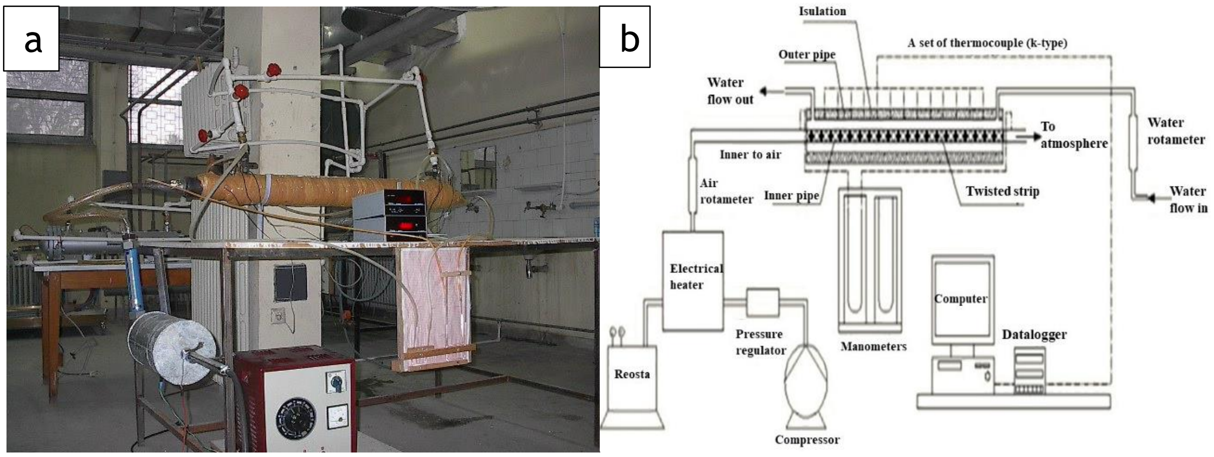

Figure 1. a) *The experimental setup* ***b)*** *Schematic diagram of the experimental system.*

The design of the turbulator, formed by twisting galvanized iron strips with dimensions of 60 mm in width (H) and 2 mm in thickness (t), is illustrated in Figure 2. The overall lengths of the turbulators were 275 mm, 550 mm, 582 mm, and 1100 mm. The pitch, defined as the distance traveled by the strip after one full rotation around its axis, is illustrated in the figure. All turbulators tested were constructed with a consistent pitch of 100 mm. The inner diameters of the inner and outer pipes were 50 mm and 70 mm, respectively, with an overall pipe length of 1100 mm.

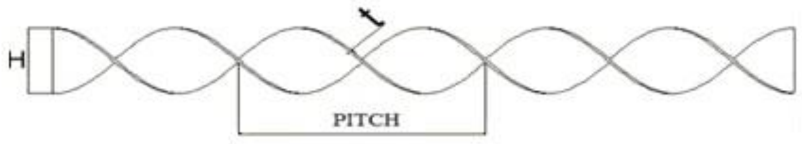

***Figure 1**. Geometrical structure of turbulator.*

Tubes equipped with twisted tapes of different lengths and tape-length ratios (l/L=0.25, 0.5, 0.75, 1) were investigated. Additionally, for comparative purposes, a full-length tape was used in certain tests.

During the experiments, a twisted tape was positioned at the inlet of the test section to function as a swirl flow generator, promoting enhanced heat transfer within the tube. Hot air flowed through the inner pipe, while cold water moved through the surrounding annular space. The air entering the system was heated via an electrical heater, with its power output controlled using a variable-output voltage transformer.

The inlet and outlet temperatures of air and water, as well as those at 10 evenly distributed points along the inner pipe, were measured using a multichannel temperature monitoring system equipped with Fe-constantan thermocouples.

Air and water flow rates were adjusted using rotameters and valves positioned at the inlets. Pressure drops across the heat exchanger pipes were determined with the help of two inclined water manometers connected to the inlet and outlet sections.

Experiments were carried out under both parallel and counter flow arrangements, testing a variety of turbulent elements over a wide range of Reynolds numbers.

4 RESULTS

Before assessing the impact of the turbulators, an equivalent number of experiments was conducted with an empty inner pipe across Reynolds numbers ranging from 3400 to 6900. This step was undertaken to validate the methodology against the Dittus-Boelter correlation.

Based on the experimental data collected from the air side, the relationship between Nusselt numbers and Reynolds numbers was analyzed and plotted for both parallel and countercurrent flow configurations, as shown in Figures 3 and 4, respectively.

The Nusselt numbers showed a significant increase when turbulators were employed in the tubes. For countercurrent flow, the improvement in Nu numbers reached up to twice the values observed in the empty tube. The effect of turbulators on heat transfer was more pronounced at higher Reynolds numbers. While a similar trend was noted for parallel flow, as shown in Figure 3, the enhancement was 10-20% lower than that observed for countercurrent flow, as shown in Figure 4.

The overall findings confirm that, in all configurations, the use of turbulators resulted in higher Nusselt numbers compared to a plain tube. The relationship between pressure drops and Reynolds numbers for tubes equipped with twisted tape inserts of varying lengths is shown in Figure 5.

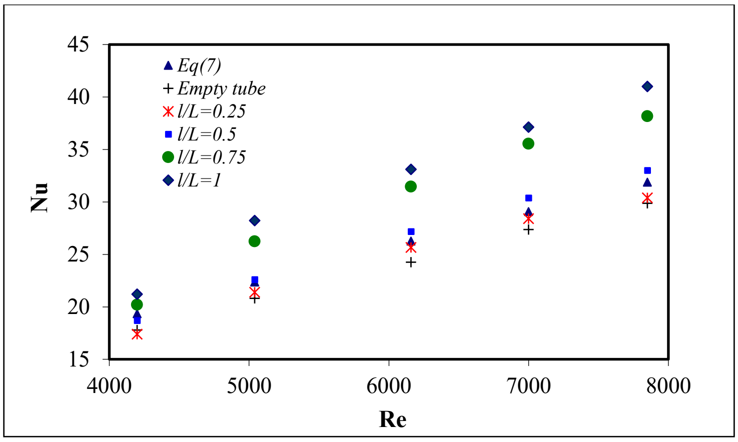

Figure 2. *Nusselt numbers for parallel flow.*

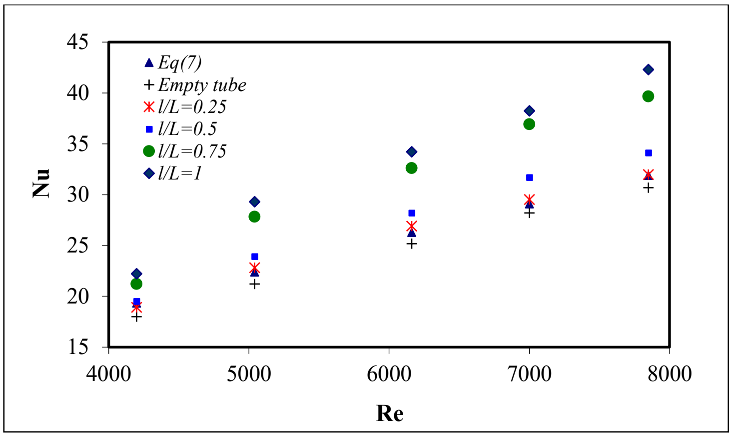

***Figure 3**. Nusselt numbers for countercurrent flow.*

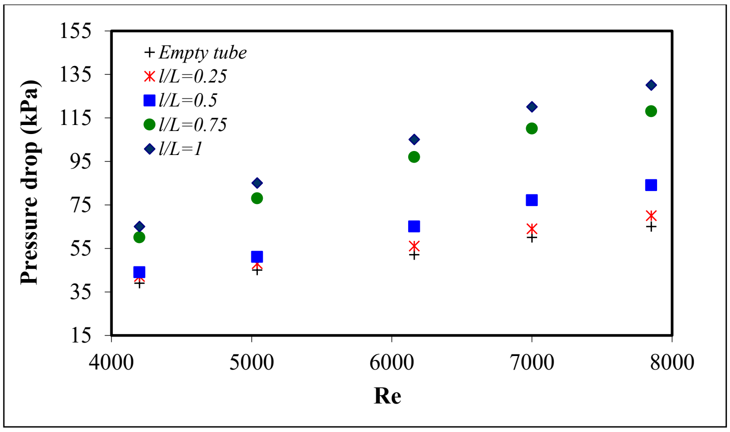

***Figure 4**. Pressure drops along the heat exchanger tube equipped with helical turbulators.*

It is evident that the introduction of turbulators into the flow path causes a significant increase in pressure drop. For all turbulators with varying lengths of twisted tape, the pressure drop values were observed to be greater at higher Reynolds numbers.

5 DISCUSSION

In this study, an experimental investigation of heat transfer (Nusselt number, Nu) and pressure drops in a heat exchanger with a plain tube and twisted tapes of varying length ratios of (*l*/L= 0.25, 0.5, 0.75, 1) was conducted and the findings are presented. Several salient concluding remarks are revealed by the present study, which are summarized as follows:

• Compared to a conventional heat exchanger, the augmented model demonstrated a significant improvement in the heat transfer coefficient, with a 61% increase for twisted tape at l/L= 0.25 and a 78% increase for twisted tape at l/L=1.

• The Nu values for tubes with twisted tape inserts of varying lengths were found to be approximately 1.2-1.8 times higher than those for the plain tube, maintaining a consistent trend.

• It was observed that the smallest tape-length ratio (l/L=0.25) resulted in the lowest heat transfer rate.

• The twisted tape with the highest length ratio (l/L=1) provided a heat transfer coefficient approximately 1.5 times greater than that of the lower twist ratio (l/L=0.25).

• Pressure drops increased by up to 100% over the plain tube when using full-length twisted tapes.

• Pressure drops for tubes equipped with twisted tapes of l/L=0.25,0.5,0.75,1 rose with an increase in Reynolds number (Re).

• All tubes fitted with twisted tape inserts exhibited higher mean pressure drops compared to the plain tube.

• The pressure drop ratio showed a slight increase with the rise in Reynolds number.

• While turbulators caused a notable increase in pressure drop, the corresponding energy loss was negligible compared to the heat gain obtained from their use.

It was observed that an increase in heat gain corresponded with an increase in pressure drop. However, the energy loss resulting from the pressure drop was significantly lower than the heat gain achieved. The variation of the heat gain-to-pressure drop ratio as a function of the Reynolds number is illustrated in Figures 6 and 7 and can be calculated using the following equation [16], [18] :

$$\frac{Q_{NG}}{\Delta P_A} = \frac{Q_{ts} - Q}{\Delta P_{ts} - \Delta P}\ 1000.V \qquad \textbf{(9)}$$

Where ΔP_{ts} (kPa) and ΔP (kPa) are the pressure decreases in the heat exchanger with and without the twisted strips, respectively, while Q_{ts} (W) and Q (W) are the heat energy amounts transferred in the heat exchanger with and without the twisted strips.

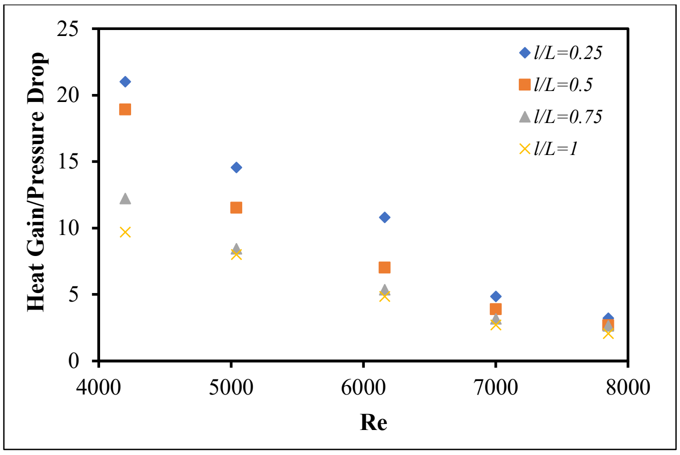

Figure 5. *Variation of (Heat Gain/Pressure Drop) for parallel flow.*

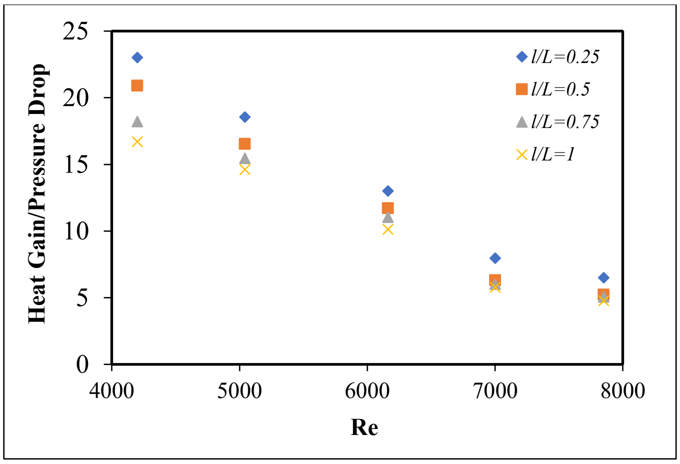

Figure 6. *Variation of (Heat Gain/Pressure Drop) for countercurrent flow.*

In Figure 6 and 7, the "heat gain/pressure drop" ratio decreases significantly for all *l*/L ratios as the Reynolds number increases. This trend shows that pressure losses increase significantly at high flow rates, whereas the increase in heat transfer is more limited. The highest ratio is observed for *l*/L = 0.25 at low Reynolds numbers. This indicates that the shorter the twisted strips offer a more favourable performance. At *l*/L = 0.5, 0.75, and 1, the efficiency value is lower, suggesting that longer the twisted strips lead to more pressure drop than heat gain due to increased friction losses.

Notations

A = Surface area for heat transfer (in square meters).
A_c = Surface area of the duct (in square meters)
C_p = Heat capacity per unit mass (in joules per kilogram per kelvin).
D_e = Equivalent diameter of the tube (in meters).
H = Width of twisted strips (in meters).
h = Coefficient of film heat transfer (in watts per meter-kelvin).
l= Twisted tape length (in meters).
L = Tubes length (in meters).
m = Flow rate of mass (in kilograms per second).
Nu = Dimensionless Nusselt number, representing convective heat transfer.
P = Perimeter per unit length of the duct (in meters)
Pr= Dimensionless Prandtl number, indicating fluid heat transfer characteristics.
Q = Heat transfer power (in watts).
Re = Reynolds number, expressing flow conditions in the system.
t = thickness of twisted strips (in meters)
T = Fluid temperature (in kelvin).
v = Kinematic viscosity of the fluid (in square meters per second).
V = Flow rate of fluid volume (in cubic meters per second).

Subscripts

i = inlet
c = cold
h = hot
o = outlet
w = wall

Conflict of Interest

There is no conflict of interest between the authors.

Authors Contributions

Zeki ARGUNHAN: Project administration, investigation, methodology, conceptualization, conduct practical experiments, visualization, writing – original draft, writing – review and editing.

Cengiz YILDIZ: Project administration, investigation, methodology, conceptualization, conduct practical experiments, visualization, writing – original draft, writing – review and editing.

Emin EL: Investigation, visualization, writing – original draft, writing – review and editing.

Statement of Research and Publication Ethics

The study is complied with research and publication ethics.

Artificial Intelligence (AI) Contribution Statement

This manuscript was entirely written, edited, analyzed, and prepared without the assistance of any artificial intelligence (AI) tools. All content, including text, data analysis, and figures, was solely generated by the authors.

REFERENCES

[1] H. Hamed, A. Mohammed, R. Khalefa, O. Habeeb, and M. Abdulqader, "The Effect of using Compound Techniques (Passive and Active) on the Double Pipe Heat Exchanger Performance," *Egypt. J. Chem.*, pp. 0-0, Mar. 2021, doi: 10.21608/ejchem.2021.54450.3134.

[2] M. Sheikholeslami, M. Gorji-Bandpy, and D. D. Ganji, "Review of heat transfer enhancement methods: Focus on passive methods using swirl flow devices," *Renew. Sustain. Energy Rev.*, vol. 49, pp. 444-469, Sep. 2015, doi: 10.1016/j.rser.2015.04.113.

[3] F. Seibold, P. Ligrani, and B. Weigand, "Flow and heat transfer in swirl tubes — A review," *Int. J. Heat Mass Transf.*, vol. 187, p. 122455, May 2022, doi: 10.1016/j.ijheatmasstransfer.2021.122455.

[4] J. Chen *et al.*, "Understanding the role of swirling flow in dry powder inhalers: Implications for design considerations and pulmonary delivery," *J. Control. Release*, vol. 373, pp. 410-425, Sep. 2024, doi: 10.1016/j.jconrel.2024.07.034.

[5] M. Hangi, A. Rahbari, X. Wang, and W. Lipiński, "Hydrothermal characteristics of fluid flow in a circular tube fitted with free rotating axial-turbine-type swirl generators: Design, swirl strength, and performance analyses," *Int. J. Therm. Sci.*, vol. 173, p. 107384, Mar. 2022, doi: 10.1016/j.ijthermalsci.2021.107384.

[6] D. Wang, A. Khalatov, I. Borisov, E. Shi-Ju, and O. Stupak, "Swirling flow and heat transfer in a pipe: Decay and transition to axial flow," *Int. J. Heat Mass Transf.*, vol. 233, p. 125976, Nov. 2024, doi: 10.1016/j.ijheatmasstransfer.2024.125976.

[7] L. Liu, J. Zhang, S. Liu, K. Wang, and H. Gu, "Decay law and swirl length of swirling gas-liquid flow in a vertical pipe," *Int. J. Multiph. Flow*, vol. 137, p. 103570, Apr. 2021, doi: 10.1016/j.ijmultiphaseflow.2021.103570.

[8] R. Babu., P. Kumar., S. Roy, and R. Ganesan, "A comprehensive review on compound heat transfer enhancement using passive techniques in a heat exchanger," *Mater. Today Proc.*, vol. 54, pp. 428-436, 2022, doi: 10.1016/j.matpr.2021.09.541.

[9] R. Mashayekhi, A. H. Eisapour, M. Eisapour, P. Talebizadehsardari, and A. Rahbari, "Hydrothermal performance of twisted elliptical tube equipped with twisted tape insert," *Int. J. Therm. Sci.*, vol. 172, p. 107233, Feb. 2022, doi: 10.1016/j.ijthermalsci.2021.107233.

[10] B. Kumar, A. K. Patil, S. Jain, and M. Kumar, "Effects of Double V Cuts in Perforated Twisted Tape Insert: An Experimental Study," *Heat Transf. Eng.*, vol. 41, no. 17, pp. 1473-1484, Sep. 2020, doi: 10.1080/01457632.2019.1649926.

[11] Y. Hong, L. Zhao, Y. Huang, Q. Li, J. Jiang, and J. Du, "Turbulent thermal-hydraulic characteristics in a spiral corrugated waste heat recovery heat exchanger with perforated multiple twisted tapes," *Int. J. Therm. Sci.*, vol. 184, p. 108025, Feb. 2023, doi: 10.1016/j.ijthermalsci.2022.108025.

[12] M. M. K. Bhuiya, M. M. Roshid, M. M. M. Talukder, M. G. Rasul, and P. Das, "Influence of perforated triple twisted tape on thermal performance characteristics of a tube heat exchanger," *Appl. Therm. Eng.*, vol. 167, p. 114769, Feb. 2020, doi: 10.1016/j.applthermaleng.2019.114769.

[13] B. K. Dandoutiya and A. Kumar, "Study of thermal performance of double pipe heat exchanger using W-cut twisted tape," *Energy Sources, Part A Recover. Util. Environ. Eff.*, vol. 45, no. 2, pp. 5221-5238, Jun. 2023, doi: 10.1080/15567036.2023.2207497.

[14] R. Behcet., A. Yakut., and Z. Argunhan., "The effect of rotary type turbulator placed in entrance of heat exchanger on heat transfer and frictional loss," *Energy Educ. Sci. Technol. Part A-Energy Sci. Res.*, vol. 28, no. 1, pp. 239-248, 2011.

[15] Z. Argunhan and C. Yıldız, "The effects of swirl generator having wings with holes on heat transfer and pressure drop in tube heat exchanger.," *Pamukkale Univ. J. Eng. Sci.*, vol. 12, no. 2, pp. 217-223, 2011.

[16] F. P. Incropera and D. P. Dewitt, *Fundamentals of heat and mass transfer*, 6th. ed. New York: J. Wiley & Sons, 2006.

[17] V. I. Deev, V. S. Kharitonov, A. M. Baisov, and A. N. Churkin, "Heat transfer characteristics of water under supercritical conditions," *Int. J. Therm. Sci.*, vol. 171, p. 107238, Jan. 2022, doi: 10.1016/j.ijthermalsci.2021.107238.

[18] G. Çakmak and C. Yıldız, "The influence of the injectors with swirling flow generating on the heat transfer in the concentric heat exchanger," *Int. Commun. Heat Mass Transf.*, vol. 34, no. 6, pp. 728-739, Jul. 2007, doi: 10.1016/j.icheatmasstransfer.2007.03.007.